

IMPROVING AEROSOL DISPERSION THROUGH A FUNDAMENTAL
UNDERSTANDING OF INTERPARTICLE FORCES

By

STEPHEN THOMAS TEDESCHI

A DISSERTATION PRESENTED TO THE GRADUATE SCHOOL
OF THE UNIVERSITY OF FLORIDA IN PARTIAL FULFILLMENT
OF THE REQUIREMENTS FOR THE DEGREE OF
DOCTOR OF PHILOSOPHY

UNIVERSITY OF FLORIDA

2007

© 2007 Stephen Thomas Tedeschi

To my Grandfather, Frank Mone, who first taught me about engineering and instilled in me the desire learn about how and why all things work, that is, the science of everything. The time I spent helping you on those projects, although too few, started me down the path I'm on today.
Thank you.

ACKNOWLEDGMENTS

I first thank my advisor, Dr. Hassan El-Shall, for all of his wisdom and guidance throughout my studies here at the University of Florida. His extensive knowledge and experience were invaluable sources of information and encouragement.

I acknowledge my committee members for their helpful discussions and suggestions including Dr. Rolf Hummel, Dr. Brij Moudgil, Dr. Arun Rande, Dr. Rajiv Singh, and Dr. Spyros Svoronos. Special recognition goes to Professor Brian Scarlett. He will always be remembered for his unwavering belief in his students and encouragement for the pursuit of knowledge and the understanding of science of all things. These values he lived for live on in all of us who knew him.

I thank my family, especially my parents Frank and Raffeale and my brother Daniel, for always believing in me and encouraging me to follow my dreams. E alla mia Nonna, grazie mille per tutto! Their support was essential to accomplishing this goal.

I especially want to thank my fiancée Dr. Anna Fuller for her never ending patience and encouragement throughout our many years here. So many dinner conversations over research helped us through so many of those challenges. It won't have been possible without you.

Many thanks go to Dr. Nate Stevens, Dr. Scott Brown and Dr. Yakov Rabinovich, for their help in several details of my research. I also thank Dr. Kevin Powers for his advice and debates with me over almost every point of the project, as well as Gill Brubaker and Gary Scheiffele for their invaluable assistance and Kerry Siebein for all of her assistance on the SEM and TEM.

I also gratefully acknowledge my current group members including Dr. Maria Palazuelos Jorganes, Dr. Saijit "Ply" Daosukho, Rhye Hamey, Yang-Yao "Simon" Lee, Kerri-Ann Hue, Milorad Djomlija, Julio Castro, Amit Singh, Debamitra Dutta, and Kalyan Gohkale; past members including Dr. Ayman El-Midany, Dr. Olesya Zhupanska, Dr. Ecivit Bilgili, Dr. Mario

Hubert, Dr. Dimitri Eskin, Dr. Nishanth Gopinathan, Dr. Madhavan Esayanur, Dr. Caner Yurteri, Dr. Dauntel Specht, Dr. Marco Verwijs, and Dr. Kerry Johanson; and undergraduate students including Calvin Faucett for their help in carrying out my research, and also for their support and encouragement. Dear colleagues and friends, thank you for making my time here in Gainesville interesting and memorable.

I thank the staff of the Particle Engineering Research Center including Jamie Anders, Ashley Boller, Noeleen Brophy, Anne Donnelly, John Henderson, Donna Jackson, Dr. Victor Jackson, Sophie Leone, James Newman, Greg Norton, and Jo-Anne Standridge for all of their support and assistance.

Lastly, I acknowledge the Particle Engineering Research Center, the United States Army Environmental, Chemical, and Biological Center, and our industrial partners for their financial support.

TABLE OF CONTENTS

	<u>page</u>
ACKNOWLEDGMENTS	4
LIST OF TABLES	9
LIST OF FIGURES	10
ABSTRACT	14
CHAPTERS	
1 INTRODUCTION	16
Impact of Dry Powder Dispersion	16
Current Research	18
2 BACKGROUND	21
State-of-The-Art Dispersion Techniques	21
Mechanical Dispersion Devices and Methods	21
Reducing Attractive Forces	26
Particle Charging to Increase Repulsive Forces	28
Powder Processing Techniques to Reduce Capillary Effects	29
Summary of Current Research	32
3 INTERPARTICLE FORCES IN AEROSOLS	36
Introduction	36
van der Waals Forces	37
Microscopic Approach	38
Macroscopic Approach	39
Surface Energy Approach to Adhesion	40
Capillary Forces	41
Roughness	42
Electrostatic Forces	44
4 MATERIALS AND METHODS	51
Material	51
Experimental Factors and Processing Methods	52
Drying Method	53
Spacer Material	54
Relative Humidity	55
Surface Modification	56
Dispersion Medium	56

Characterization Methods.....	57
Particle Size and Morphology	57
Material surface energy	60
Dispersion Characterization	60
Particle size comparison.....	61
Settling measurements.....	61
Powder Mechanics.....	62
Interparticle Forces.....	64
Design of Experiments	65
5 RESULTS AND DISCUSSION.....	73
Characterization.....	73
Particle Size of Single Materials	73
Particle Size of Mixtures	75
Morphology	75
Drying Methods.....	76
Aerosol Experiments	78
Spacer Addition.....	78
Dispersion Medium	83
Surface Modification.....	85
Design of Experiments	88
Interparticle Forces on the Macro and Micro Scale.....	89
Bulk Powder Strength.....	90
Experimental methods.....	90
Shear test results.....	91
Shear test discussion.....	92
Interparticle Forces.....	93
Experimental methods.....	94
Interparticle force results and discussion	96
Data Correlation.....	99
6 CONCLUSIONS	136
7 CASE STUDY: ARMY OBSCURANTS	141
Introduction.....	141
Experimental.....	143
Factors and Preparation:	143
Flake Thickness	143
Spacer material	144
Characterization.....	145
Particle size and morphology	145
Aerosol performance	145
Powder performance	146
Results and Discussion	148
Conclusions	150

8 SUGGESTIONS FOR FUTURE WORK.....	157
LIST OF REFERENCES.....	160
BIOGRAPHICAL SKETCH.....	171

LIST OF TABLES

<u>Table</u>		<u>page</u>
3-1	van der Waals interaction forces and energies for different geometries.....	50
3-2	Interaction energy using the Derjaguin Approximation.	50
5-1	Summary of optimum surface modified aluminum.	135

LIST OF FIGURES

<u>Figure</u>	<u>page</u>
1-1 Representation of the relationship developed through this research.	20
2-1 The Thermodynamics of drying methods.	35
3-1 Illustration of important interparticle forces in powders and aerosols.	48
3-2 Depiction of the three interactions known as van der Waals forces.	48
3-3 Depiction of the calculation of force using the Derjarguin Approximation.	49
3-4 Change in contact area with increasing roughness.	49
4-1 A roadmap to dispersion: depiction of the direction for the presented research.	67
4-2 Thermodynamic path of drying methods investigated.	68
4-3 Images of the Air dispersion chamber.	69
4-4 The Sci-Tec ShearScan TS12 shear tester and test cell.	70
4-5 A typical result from the consolidation and failure of a powder sample.	70
4-6 Schematic of the AFM operation.	71
4-7 Example of a force distance curve for the AFM.	72
5-1 Particle size distribution of aluminum flakes.	101
5-2 Particle size distribution of Valimet aluminum in isopropyl alcohol.	101
5-3 SEM images of Sigma VPD Aluminum flakes.	102
5-4 TEM images of Sigma 1215 aluminum flakes.	102
5-5 Contact mode topographical images of aluminum flakes.	103
5-6 Detailed topographical image of flake surface.	103
5-7 SEM Image of Valimet aluminum spheres.	104
5-8 Phase diagram for carbon dioxide as related to supercritical drying.	104
5-9 Particle size distribution measured following each drying method.	105
5-10 Contact area with increasing roughness.	105

5-11	Calculated van der Waals forces of a smooth and rough surface.	106
5-12	Illustration of the change in contact area as a result of the addition of fumed silica.....	106
5-13	Calculated van der Waals forces with the addition of silica.....	107
5-14	SEM images of aluminum flakes with silica.	108
5-15	Air Chamber transmission measurement.	108
5-16	Average and standard deviation of settling rate.....	109
5-17	Airborne concentration at selected times after partial vacuum dispersion.	109
5-18	Airborne concentration by vacuum dissemination with silica.....	110
5-19	Dissemination pressure and airborne concentration.	110
5-20	Airborne concentration by high pressure gas dissemination with silica.....	111
5-21	Illustration of the dispersion effect of liquid carbon dioxide.....	111
5-22	Airborne concentration produced by liquid carbon dioxide dissemination.....	112
5-23	Airborne concentration for gas vs. liquid carbon dioxide.....	112
5-24	Airborne concentration using liquid carbon dioxide and silica.	113
5-25	Summary of airborne concentration by carbon dioxide dispersion.	113
5-26	Particle size of aluminum flakes at 20, 50, and 80% relative humidity.....	114
5-27	Digital image of water drops on aluminum as used for measurement.....	114
5-28	Contact angle on ODTMS surface modified aluminum.	115
5-29	Change in contact angle of TDFS surface modified aluminum.....	115
5-30	Digital image of water drop on modified flake bed.....	116
5-31	Airborne concentration of surface modified aluminum flakes at 50% humidity.....	116
5-32	Airborne concentration of bare aluminum at 20, 50, and 80% humidity.	117
5-33	Experimental design dispersion results.	117
5-34	Unconfined yield strength vs major consolidation stress at 20% relative humidity.....	118
5-35	Unconfined yield strength vs major consolidation stress at 50% relative humidity.....	119

5-36	Unconfined yield strength vs major consolidation stress at 80% relative humidity.....	120
5-37	Unconfined yield strength vs major principle stress for bare aluminum.....	121
5-38	Unconfined yield strength vs major principle stress for TDFS modified aluminum.....	122
5-39	Unconfined yield strength vs major principle stress for ODTMS modified aluminum. .	123
5-40	Response plot for unconfined yield strength.	124
5-41	Damaged aluminum coating on cantilever tip.....	124
5-42	Bare aluminum particle probe.....	125
5-43	ODTMS modified Aluminum particle probe.....	125
5-44	Contact mode image of the CVD bare aluminum surface.....	126
5-45	Contact mode image of bare aluminum in 3D.....	126
5-46	Detailed contact mode image of bare CVD aluminum.....	127
5-47	Contact mode image of bare aluminum in 3D.....	127
5-48	Contact mode image of ODTMS modified aluminum.....	128
5-49	Contact mode image of ODTMS aluminum in 3D.....	128
5-50	Typical force distance curve.....	129
5-51	Interparticle force at humidity for bare aluminum.....	130
5-52	Interparticle force at humidity for ODTMS modified aluminum.....	131
5-53	Comparison of the effect of surface modification.....	132
5-54	Interaction energy and surface modification.....	133
5-56	Overlay of response plots.....	134
5-57	Overlay of contour on airborne concentration results.....	134
7-1	Laser Diffraction particle size distribution for aluminum flakes.....	152
7-2	Typical Images of aluminum flakes and silica.....	152
7-3	Packing density of flakes and FoM.....	153
7-4	Figure of Merit for aluminum flakes of varying thickness.....	154

7-5	Figure of Merit for aluminum flakes of varying thickness and spacer concentration.	154
7-6	Average FoM for aluminum flakes of varying thickness and silica concentrations.	155
7-7	Design Expert Surface Response plot for FoM.	156

Abstract of Dissertation Presented to the Graduate School
of the University of Florida in Partial Fulfillment of the
Requirements for the Degree of Doctor of Philosophy

IMPROVING AEROSOL DISPERSION THROUGH A FUNDAMENTAL
UNDERSTANDING OF INTERPARTICLE FORCES

By

Stephen Thomas Tedeschi

December 2007

Chair: Hassan El-Shall

Major: Materials Science and Engineering

Dispersion is a vital aspect of powder technology impacting traditional and emerging technologies in many diverse areas including health, industry, the environment, and the military. In such applications, the properties and quality of the resultant product will be directly and noticeably affected by the degree to which the particles are dispersed. Reduced dispersion, or increasing agglomeration, will lead to decreased efficiency and ultimately result in a low yield and increased cost. As powder technology moves into the nano-age new, more complex challenges arise. Decreasing particle size into the submicron range significantly increases the effect of surface forces leading to an increase in the cohesive forces of the powder, thus, making an understanding of dispersion even more essential.

In order to develop the knowledge base to understand and control aerosol dispersion, a fundamental study of the significant powder characteristics and environmental conditions that effect dispersion has been completed and through this investigation the resulting change in interparticle forces has been measured. Supercritical drying was shown to successfully produce a dry, dispersible powder through the supercritical phase and the evasion of capillary forces. A fumed silica spacer material was used to improve dispersion through a reduction in contact area

and in turn van der Waals forces. Surface modification was shown to control the surface energy of the aluminum surfaces, leading to a multifaceted contribution to dispersion. First, the increased hydrophobicity reduced the amount of adsorbed water and was successfully used to control capillary forces. In the dry system, the silane was shown to also reduce van der Waals forces through the change in surface energy and the steric barrier produced. This research was guided using statistical experimental design in order to efficiently study significant factors affecting flake dispersion in air. An improvement in the dispersion of an aluminum flake system was shown. However, more importantly, a correlation between the processing parameters and the change in interparticle forces that led to the increase in dispersion was determined. It was shown that an understanding of the interparticle forces and the processing methods that affect them can be used to decrease adhesion and develop novel dissemination methods that result in improved dispersion. Ultimately, this knowledge allows the application of this research to other powder systems.

CHAPTER 1 INTRODUCTION

Powder dispersion is vital to traditional and emerging technologies in many diverse areas including health care, industry, the environment, and the military. In each application, the degree to which the powder is dispersed will have direct and noticeable effects on the properties and quality of the resultant product. Reduced dispersion, or increasing agglomeration, will lead to defects and decreased process efficiency resulting in low yield and increased cost. As powder technology moves into the nano-age, new and more complex challenges arise due to decreasing particle size into the submicron range. This significantly increases the surface forces leading to an increase in cohesiveness of the powder. Therefore, understanding these forces and their role in powder dispersion is essential.

Impact of Dry Powder Dispersion

Health care is a major area where the dispersion of drug powders greatly effects treatment. Inhaled drug aerosols are used to treat a number of lung disorders including chronic obstructive pulmonary disease (COPD), a group of lung disorders that includes asthma, and is attributed with a cost of over 14 billion dollars in the United States alone. The drug powder must be under a critical size as only drug particles 5 μm in size or smaller are capable of deep lung delivery[1]. Agglomeration of the drug leads to larger sizes and deposition on the tongue or throat rendering that portion of the dose ineffective.

Industrial powder processes, such as ceramic processing, powder metallurgy, chemical reactors, powder coating applications, and aerosol technologies require controlled dispersion of powders. Unwanted agglomeration during die filling or pressing will reduce the quality of the product by creating density gradients and voids[2]. Chemical reactors, coal, and other powder burning operations require a uniform particle size distribution in order to maintain a constant

heating rate. Agglomeration of the powder will result in an inconsistent particle size and lead to variations in the products. Powder coating operations rely on dispersed powder to produce uniform coatings on the substrate. Powder dispersion is also an important factor in aerosol technologies. Separation and classification systems must be able to separate starting materials into the true primary particle sizes in order to obtain optimum results. Also, the evaluation of filters requires that the powder passing through the filtration system be fully dispersed into a known and uniform size to measure the true filter efficiency. These are only a few industrial applications, but the great extent of the impact is readily acknowledged.

Increased dispersion will also have an impact on the environment. Dry powders are used in agriculture as fertilizers to enrich the soil and as pesticides to increase crop yield. Reports have shown that fertilization has many beneficial effects on soil including increased water holding capacity, porosity, infiltration capacity, hydraulic conductivity, water stable aggregation, and decreased surface crusting[3]. In the long term, this will lead to higher quality soil and increased crop yield. Dry chemicals used in firefighting are vital when water is not available or when water cannot be used, i.e. electrical fires. In both cases by increasing the degree of dispersion, the higher surface area available for reaction will increase the effectiveness of these chemicals and in turn a smaller amount of the chemical will be required for the same performance. Farmers will use less fertilizer lowering costs and leading to more organic, healthier foods and firefighters will be able to extinguish fires more efficiently with less chemicals reducing the concern for environmental cleanup following a fire.

Effective aerosolization is also important for defense. The United States Military Services rely on obscurant clouds to hide personnel and equipment from enemy acquisition[4]. A program has been initiated to develop more efficient obscurants by engineering the particle

which make up the cloud. In order to realize the full potential of the engineered particulates, dispersion of the powder in the aerosol into primary particles must be achieved. In addition, the powder settling rate greatly depends on particle size and reducing the size will increase the amount of time the powder is airborne. Therefore, any agglomeration of the material, before or after dissemination, will result in decreased obscuration efficiency.

Great improvements in all of these areas can be realized by controlling the degree of powder dispersion. Benefits include decreased costs and, simultaneously, increased efficiency. Towards these ends, researchers have undertaken the investigation of powder dispersion for a variety of these applications. However, dispersion is a very complex problem as powder properties are unique to the material of which they are made and can change as their environment changes. The majority of the published research is empirical in nature and focuses on optimizing the dispersion of a specific powder, for a particular application, under a given set of conditions. Little work has been done to correlate the interparticle forces involved in dispersion with the powder properties, effect of environmental conditions, and general trends seen in particle size, and degree of dispersion, measurements. A systematic study of the parameters involved in the particulate system, including correlating the effect microscopic (interparticle forces and surface forces) and macroscopic (bulk forces) interactions together with the influence of the surrounding medium on these interactions, is required.

Current Research

The first step towards the realization of an increased state of dispersion is an understanding of the interparticle forces of a given system and the factors that affect them. It should be recognized that the dominant forces are dependent on the physical and chemical properties of the material and thus will vary between particle systems. However, if a general battery of tests is

developed along with the understanding of the relationship to interparticle forces, this knowledge can be applied to any powder. Therein lies the focus of this research.

The goal of this research is to study the fundamental interactions between particles in air and their magnitude. In addition, the effect of significant factors on the particle and bulk scale forces and their subsequent influence on the particle size distribution after aerosolization has been studied both experimentally and theoretically. This document describes a systematic study of the physical, chemical, and environmental factors that has been completed for an aluminum flake material in order to develop a fundamental understanding of the effect of these aspects on airborne concentration and particle size through the correlation of factor effect on single particle and bulk scale force measurements.

The degree of dispersion in air is dependent on two things, the source and magnitude of the significant interparticle forces, and the energy supplied to the agglomerated powder by the disperser. An illustration of the interrelationship developed through this research is given in Figure 1-1. For this research, relative humidity, powder surface modification, the effect of flow aids such as second phase particles, and dispersion medium were studied and an understanding of the fundamental interactions relevant to dispersion were determined. Statistical experimental designs were used to systematically investigate these factors to efficiently determine those significant to the aerosolized particle size distribution. Additionally, interparticle force measurements using the atomic force microscope (AFM) were made to determine the effect of the significant factors on particle, or micro-scale, and shear were made to see their effect on the bulk, or macro-scale. When these results were compared, insight into the mechanism of adhesion for a given powder, and thus the best method of dispersion, was determined.

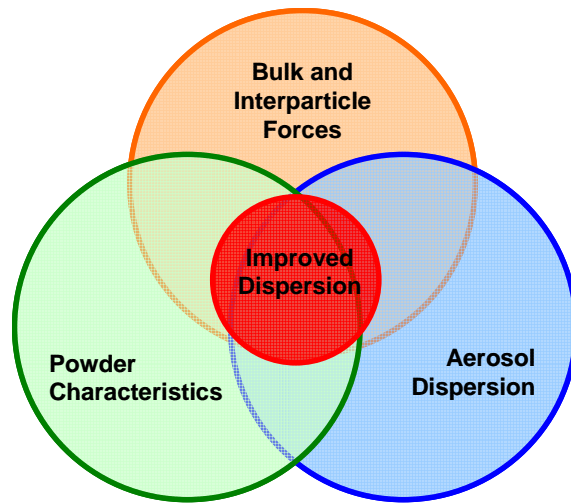


Figure 1-1. Representation of the relationship developed through this research. Through an understanding of the effect of significant powder characteristics, processing parameters on aerosolized particle size and their correlation to bulk and interparticle forces the fundamental knowledge base required to improve aerosol dispersion can be developed.

CHAPTER 2 BACKGROUND

A great deal of work has been put forth to improve dispersion in several diverse fields. The research covers a large number of materials in many different areas and technologies. However, since powder properties are commonly unique to a specific material, one dispersion method may not be effective for more than one powder[5-14]. In order for powder to be dispersed, the external force applied to the cluster of powder as a bulk or agglomerate must be larger than the attractive forces holding the powder together. The powder particles themselves can also be modified to reduce the attractive forces between them and thus reduce the amount of energy needed to disperse them. Many examples are seen for the dispersion of pharmaceutical drug powders, which is a major area of research due to their direct effect on the treatment of health problems and accounts for a majority of the published research. Efforts have focused on four main areas: developing mechanical dispersion devices, reducing attractive forces between particles, increasing repulsive forces, and improving processing and drying methods. Each will be discussed in more detail.

State-of-The-Art Dispersion Techniques

Mechanical Dispersion Devices and Methods

In general, there are a number of different types of dispersion devices that can be characterized by the method in which the aerosol is disseminated. Many variations of dispersion devices can also be found in literature[15-22]. For some devices, the powder is dispersed in a dilute suspension with a volatile liquid. It is then nebulized into small droplets containing particles. The liquid then volatilizes leaving the powder suspended in an aerosol. If, however, more than one particle is present in each drop, capillary forces caused by a decrease in liquid volume of the meniscus between them can cause the particles to become agglomerated. Dry

powders are also dispersed in fluidized beds where larger particles can be added to aid in dispersion. Smaller particles are entrained in the air stream flowing through the bed and carried out of the device. Dry powders can also be disseminated by high speed air jets that entrain and mix the powders. These dispersion systems rely on airflow to impart the energy required to disperse the powder through rapid acceleration and deceleration along with rapid compression or expansion of the carrier gas. Venturi type nozzles, ejectors, and by annular nozzles, which can operate at subsonic, sonic, or supersonic velocities, are examples of this type of device. Internal propellers have also been added to aid the mixing of different powders and in dispersion. A number of commercial and experimental devices for dry powder dispersion, such as classifier nozzles and dust generators, have been reviewed in literature by Ranade and Calabrese[23] as have a number of dry powder inhalers (DPIs) for the administration of pharmaceutical powders by Hickey and coworkers[18].

Improved performance requires a better understanding of how these devices work. A dispersion device has two functions: (1) entrain the powder in air from the bulk reservoir and (2) carry the particles out of the device and into the environment to produce an aerosol cloud. During one or both of these functions, additional steps are required to disperse the powder and maintain that state of dispersion. Often mechanical dispersion, or deagglomeration, is achieved by shear and impaction.

Shear can be produced by acceleration in air and is a common dispersion method employed by many nozzle-type dispersion devices including venturiers, ejectors or sub-sonic, sonic, and super-sonic nozzles discussed previously. The rapid acceleration or deceleration of the air around the powder and by rapid volume change through expansion or compression of the air causes shearing and normal forces that act to separate particles. The particles suspended in a

fluid third phase, liquid or gas, will experience forces from the movement of medium in the form of these pressure and velocity gradients. As the agglomerate enters the flow field, it will experience a shear force produced by the sudden acceleration, which, if larger than the attractive forces between the particles, will pull them apart. The magnitude of the airflow velocity and pressure change through the nozzle can be controlled by design and will affect the amount of energy supplied to the agglomerate.

Unstable airflow leads to large velocity gradients in the form of small turbulent eddies. The agglomerate, possessing a sufficiently large size and inertia in comparison to that of the eddy, will not be able to follow the abnormal path of the airflow. The resulting stresses experienced by the agglomerate as it travels past these eddies act to disperse it. Agglomerates smaller in scale than the eddies will, however, be able to follow the fluid flow of the turbulent air more closely and not experience the large stresses needed for dispersion. Thus, conditions for a lower limit to the effectiveness of this method are recognized. In their study, Ranade and Calabrese[23] found that an annular geometry dispersion device configured such that the particles enter the air stream at the point of maximum energy, i.e. maximum turbulence created by an acceleration gradients, led to the best dispersion. Turbulence created by device configuration was experimentally studied for a number of dry powder inhalers (DPI's) by Chew[24-26] for pharmaceutical powders. It was shown that the airflow was highly dependent on the device configuration but varied with the drug powder used such that no one configuration worked well of all powders.

Turbulence has also been experimentally studied with latex particles in conjunction with a numerical simulation developed by Endo[27]. The simulation was compared to the experimental results and used to calculate the adhesion force of spherical particles. A value of approximately

1 MPa was calculated for two 1 μm latex particles. In this work, the effect on the particle size distribution was not included. Changes in particle size distribution will change the powder packing and thus the number of particle contacts in the bulk powder. This will influence the powder strength and the force needed to disperse it. Particle size distribution has been shown to change the number of contacts between particles and thus the total adhesion of the bulk powder[28-31]. It was acknowledged that increasing the total number of contacts between particles in a bulk powder increased the points of adhesion and in turn led to a stronger powder. Straying from a spherical particle shape introduces errors that have not yet been included in the model. One reason for this is that the particle shape also affects the number of contacts as well as the total area in contact. High aspect ratio particles such as flakes may have a smaller number of contacts but have a larger total contact area which will also lead to an increase in powder strength. This has been experimentally shown to affect the degree of dispersion in a number of studies[9, 32, 33].

Turbulent flow through any system will also lead to impaction. Turbulence will cause particles to collide with each other and the wall as they move through the turbulent air[34, 35]. The force of the collisions will be dependent on the particle size and inertia, the gas velocity, and the velocity gradients determined by the eddy size. Y. He studied the effect of collision on dispersion and showed that collisions of sufficient force were enough to separate agglomerates of some powders[36]. The force of the airflow combined with impaction has to be larger than the interparticle forces of the agglomerate. Galk and coworkers study this technique in a classifier[17]. It was shown that by adding an impeller in the dispersion step of a industrial classification system, improvements in dispersion were achieved.

In many devices, an impeller, a rotating disk or internal propeller, was added to increase turbulence. Voss and Finley[22] investigated the effect of turbulence by comparing a dispersion rig they developed against a common pharmaceutical inhaler that uses this technology, the Diskhaler®. They concluded that turbulence was not the only method of deagglomeration but that impaction was also involved. Agglomerates that were too large to follow the turbulent eddies were impacted by the impeller which aided in the dispersion. A mixer-type dispersion device, which uses an internal propeller to disperse the powder, was studied by Masuda and Gotoh[37]. They found that particle size was inversely proportional to the impeller rate regardless of the powder used. The lowest operational speed was also found to be dependent on device geometry. This shows that dispersion is known to be dependent on the powder properties but the device design also significantly contributes to dispersion and operational parameters.

Particles in a stable air stream can also be impinged upon a flat plate, or other such obstacle, set perpendicular to their trajectory. The force of the agglomerate's collision with the obstacle will impart on it energy needed for fracture. After the collision the particles and agglomerates that remain will be carried past the obstacle by the air stream into a turbulent region. An experimental study by Wang[38] using a common DPI showed that by this method an increase in dispersion of 2-3 times was achieved as compared to acceleration in air alone. Gomes et al[39] have shown experimentally that the inertia of the particle is related to its residence time in the wake region of the obstacle where turbulence is high. Longer residence time in the wake region leads to more particle-particle collisions and a smaller resultant particle size. Impaction has been experimentally shown to improve dispersion in the SPIROS[20]® and rotohaler®[26] devices.

Shear, turbulence, and impaction are dispersion mechanisms that are relatively easy to generate, and can be created simply by controlling device design. However, it is seen that alone these mechanisms are not entirely sufficient and further research is required, especially for particle under $1\mu\text{m}$ in size. It is therefore necessary to also study the powder itself and add processing steps during powder production to reduce cohesion below the force of the dispersion device. A better understanding of both interparticle forces and energy available applied by these dispersion mechanisms will lead to increased dispersion.

Reducing Attractive Forces

If the attractive forces between particles are reduced, accordingly is the energy needed to separate the particles. The major contribution to attraction is attributed to van der Waals forces or capillary forces, in the presence of a liquid. The magnitude will be due to the number of contacts within the powder and the contact area between particles. These forces can be reduced by changing the Hamaker constant or surface energy of the interacting surfaces. This reduction has been accomplished in a number of ways.

A coating of a low surface energy material, such as Teflon, or chemical surface modification will reduce the attractive forces at the particle surface. Chemical surface modifications and physical coatings on metal particles were studied experimentally by Ranade and coworkers[11, 12, 40]. Five methods were investigated in an attempt to reduce the cohesion between metal powders including the addition of a spacer, chemical surface alteration, monolayer coatings of surfactants, particle encapsulation by a silane, and altering particle geometry. They found that the growth of a thin oxide layer on the metal powder significantly increased the dispersion. In order to further understand the effect on dispersion, they studied the effect of surface modification on the tensile strength of the powders. It was determined that

liquid-phase deposition of silica and a continuous oxide layer coating by steam treatment improved dispersion. The use of adsorbed films has been studied theoretically by Vold and is shown to reduce particle cohesion thereby increasing dispersion[41].

Particles of a different material can also be added in an attempt to alter the interparticle forces. Second phase particles have been investigated for use in pharmaceutical powders for DPIs. Zeng observed an increase in dispersion when fine lactose particles were added to a drug powder[13, 30, 31]. These particles had a lower interparticle attraction and thus reduced the attraction between drug particles. Louey and coworkers[8] showed an increase in the fine powder fraction (FPF), the fraction of powder below 5 μ m, by mixing two non-active spacer particles with the drug. They theorized that the carrier particles have sites of varying degrees of adhesion. The last powder to be added will attach to the site of lowest adhesion and will detach easier increasing the final FPR of drug particles released.

The size distribution and polydispersity of dry powders has also been identified to affect dispersion by increasing the packing and number of contacts. Safatov and coworkers[42] determined that the powder size distribution affected the amount of energy required for dispersion. In their work, they found that a large size distribution lead to agglomeration and attempts to disperse the powder proved more difficult than for a more monodispersed powder. Chew and Chan [28] concluded that dispersion of a smaller size distribution powder generated more fine particles when using a typical DPI. It was determined that large particles and agglomerates were lost to impaction inside the dispersion device and were not aerosolized. An increase in the width of the size distribution will also affect the particle packing, and in turn affect the number of contact points for cohesion.

Particle Charging to Increase Repulsive Forces

Dispersion can also be affected by charging the particles. Imparting a similar charge to powder particles will increase the repulsive forces by the magnitude of the charge and will counter act the attraction due to van der Waals forces[43]. Particles can obtain a charge from a number of different methods[15, 44-46]. Commonly, charge can be transferred to particles upon contact with another surface, as in tribocharging, irradiation of the powder, and collisions with electrons, ions, or ion clusters in the surrounding environment.

Ren and coworkers[47] developed a disperser for the electrostatic stabilization of fine, dry calcium carbonate and talc materials. The parameters used were in agreement with their theoretical calculations based on first principle equations. It was shown through experimentation that electrostatic stabilization of CaCO_2 was achieved for a maximum of 48 hours by corona charging. The process was highly dependent on humidity and adsorbed moisture due to the nullification of charge by water[48]. In the study, it was concluded that the method was ineffective for particles less than $2\mu\text{m}$ in size. An expression for the summation of interparticle forces was developed and the force of electrostatic repulsion needed for dispersion was determined. Simple assumptions were made and the effect of roughness was not included, a factor that is known to have a significant effect on interparticle forces[7, 8, 32, 49-55].

In subsequent research, the particle surfaces were first coated with a polymer then subjected to corona charging[56]. The polymer addition was expected to decrease the attractive forces between particles as compared to the uncoated CaCO_3 particles and hold a better charge, increasing the ability of this technique to disperse the powder yet the results showed only slight improvements. Due to these limiting factors, including humidity[15, 45, 47], the charge density

on the particles[57], particle concentration[58], and those presented in the work by Ren, it can be seen that charging is effective but only under limited conditions.

Powder Processing Techniques to Reduce Capillary Effects

Many powder processing methods require the powder to be suspended in a liquid and thus an additional drying step is needed. Conventional drying methods, such as simple evaporation or even heating under vacuum, result in a hard, dry cake. Often the agglomerates that form cannot be re-dispersed. If the powder is manufactured already containing agglomerates, the production of a dispersed aerosol becomes that much harder. Therefore, drying is a crucial step in developing a material that can be disseminated as a dispersed dry powder aerosol and will now be described in detail.

As water is removed from a powder, a liquid bridge, or meniscus, forms between the particles. These liquid bridges will be detrimental to the powder dispersion. The liquid can dissolve some of the particle surface and redeposit the material in the neck region. If the material is soluble in water, excess material can be deposited at the particle contacts as the powder is dried and form a solid bridge holding the particles together. If no dissolution occurs the liquid bridges still lead to the formation of capillary forces between the particles which will bring them into intimate contact after which van der Waals forces hold the particles together. The phase change across the gas liquid phase boundary followed by evaporation can be seen by the red line in Figure 2-1, a general gas-liquid-solid phase diagram depicting the thermodynamic phase change path of each drying method. The presence of water in the air is the source of another capillary attraction since only a very small amount is needed to form liquid bridges in the neck regions between particles. It can then be understood that drying can also be an important process for powders which are not completely immersed in liquid. A number of processing methods have been developed to overcome these difficulties including freeze-drying,

supercritical fluid processing, and a boiling method. The phase changes that occur during these drying methods can be seen in Figure 2-1 and will be explained in more detail for each process.

Freeze-drying, as the name implies, is a method during which the powder is initially exposed to temperatures low enough to freeze the liquid in the system after which the pressure is lowered by placing the sample under a high vacuum to sublime away the liquid. Using this method, capillary forces due to water bridges are avoided. The path through the phase diagram for freeze drying is depicted by the blue line in Figure 2-1. However, during freezing the liquid will crystallize and stresses develop that, if sufficiently high, may be damaging to the powders[21].

Supercritical (SC) Fluid processing is becoming a popular focus of research because of the many unique possibilities. During Supercritical Fluid Processing, or critical point drying, the liquid is heated beyond the critical point of the liquid directly to a supercritical fluid, avoiding the formation of a liquid / gas interface completely. The critical point is a critical temperature and pressure at which the densities of the gas and liquid are equal and the phase boundary between the two phases ceases to exist. Above the critical point the system is in a gaseous state and cannot be liquefied by applying pressure. SC processing is carried out in a pressure vessel in order to maintain a constant process volume. The fluid is added as a liquid and heat is applied causing the pressure to increase. The system is brought above the critical point of the fluid, that is, a temperature above which the increased pressure cannot maintain the liquid phase. This is a unique phase having qualities of both gas and liquid. As the pressure vessel is vented, the SC fluid escapes as a gas without forming liquid bridges. The process as it relates to the phase diagram is shown by the green line in Figure 2-1.

In order to carry out this process, the powder must be immersed in the medium to be taken to the supercritical point. This substance is chosen by its chemical properties, toxicity, abundance, etc., and the ease of going supercritical. The most commonly used medium for this type of processing is CO₂ mostly due to its abundance, environmental inertness, relatively low Critical point, and low toxicity. This may require an intermediate step to insure that the medium the powder is first dispersed in will be miscible with the substance. Powders dispersed in water that are not miscible in CO₂, for example, are commonly solvent exchanged with alcohol, which is miscible in CO₂.

The solubility and dispersion of powder in SC-CO₂ mediums have been improved by the use of surfactants in a similar method to common aqueous detergents. Through this research, DeSimone and coworkers have developed surfactants that will adsorb onto the particle surface allowing particles that are normally insoluble to readily disperse in the SC-CO₂ medium[59-62].

Shekunov and coworkers supercritically processed a common pharmaceutical powder used in DPIs in order to evaluate the effect on dispersion[63]. During supercritical processing, the powder formed a very loosely packed, soft agglomerate structure. There are several advantages to this loosely agglomerated structure. It yields a larger aerodynamic shape factor and low bulk density, which increases the volume diameter available to the airflow, providing rapid acceleration. In addition, the resulting agglomerates do not have a high inherent strength since no capillary forces were present to pull particles together limiting strong van der Waals attraction. The soft agglomerates that are formed can easily be broken up by the turbulent flow through an inhaler. It was shown that this processing method resulted in a factor of two increase in the drug fine particle fraction (FPF) after aerosolization as compared to other processing methods. However, this increase in the fine powder fraction was directly after production and it

did not appear to prevent agglomeration during storage due to the re-adsorption of water from the air.

Sievers and coworkers developed a method in which high concentration aqueous suspensions of therapeutic proteins were aerosolized using a supercritical CO₂-assisted method[64, 65]. The suspension was mixed with in a low dead volume tee creating an emulsion. The CO₂ was brought to its supercritical state and then passed through a capillary restrictor resulting in the aerosolization of the aqueous solution into small droplets. Many powders and solvents have been successfully investigated using this method. It was found that, the powder must be mixed with a solvent which then evaporates after aerosolization. The final particle size is thus controlled by the size of the droplet formed after aerosolization since capillary forces will hold the particles within the droplet together.

Recently, a new method of aerosol formation has been invented in which powder dispersed in water was passed through a heated capillary tube. Upon heating the water boils and generates an aerosol[66]. This process is depicted by the orange ring in Figure 2-1. It was reported that high concentration slurries were aerosolized with high fine volume fractions by this method. This process is limited by the need for a large amount of equipment limiting its ability to be used in a portable device.

Summary of Current Research

To date, the evaluation and optimization of the mechanisms and efficiency of dispersion methods in systems such as pharmaceutical powders for inhalers have typically been empirical in nature. That is, the effect of a single variable on the measured fine powder fraction (FPF), the weight percent of powder with a size less than 5 μ m, in the resultant aerosol is measured. The combination that yields the highest FPF is then chosen. A very limited scientific understanding

pertaining to the reasons for adhesion or magnitude of the force in the powder system is available. Through these investigations researchers have determined that the particle dispersion of the aerosolized powder was affected by device configuration, chamber size, impeller speed, primary particle size and morphology, powder formation, crystallinity, and particle size distribution. Estimations of the energy input needed for high fine particle fractions of powder have been developed using simple assumptions for inhaler type dispersers. Complete dispersion into primary particles, however, was not achieved by any method. These studies have shown that the generation of an aerosol from a bulk feed powder results in a maximum fine particle fraction of only 50 wt %. Examination of all of the work completed yields, at best, a vague relationship between all of the relevant variables for only a limited number of materials.

None of the work found in literature to date considers the powder system as a whole. Included in the current research, is the investigation of dispersion factors such as: the effect of relative humidity, surface modification, the effect of flow aids, and dispersion medium on the particle size and settling of the powder. In addition, interparticle forces were measured using the Atomic Force Microscope (AFM), and bulk powder properties were determined using a shear cell to understand the effect of these properties on the micro and macro scale. Statistical Design of Experiments was used to insure efficient and statistical analysis of the data. It should be recognized that the dominant forces are dependent on the physical and chemical properties of the material and thus will vary between particle systems. Once these forces are understood, the dispersion method can be optimized to overcome the forces of attraction between particles.

In Chapter 3, a more detailed expression of the significant interparticle forces found in bulk powders and aerosols as well as their sources is developed. Chapter 4 will then outline the materials and experimental procedure used in this investigation. Experimental results will be

presented in Chapter 5 and the discussion will be given in Chapter 6. The conclusions drawn from this research are explained in Chapter 7. The application of these conclusions is shown in a case study in Chapter 8.

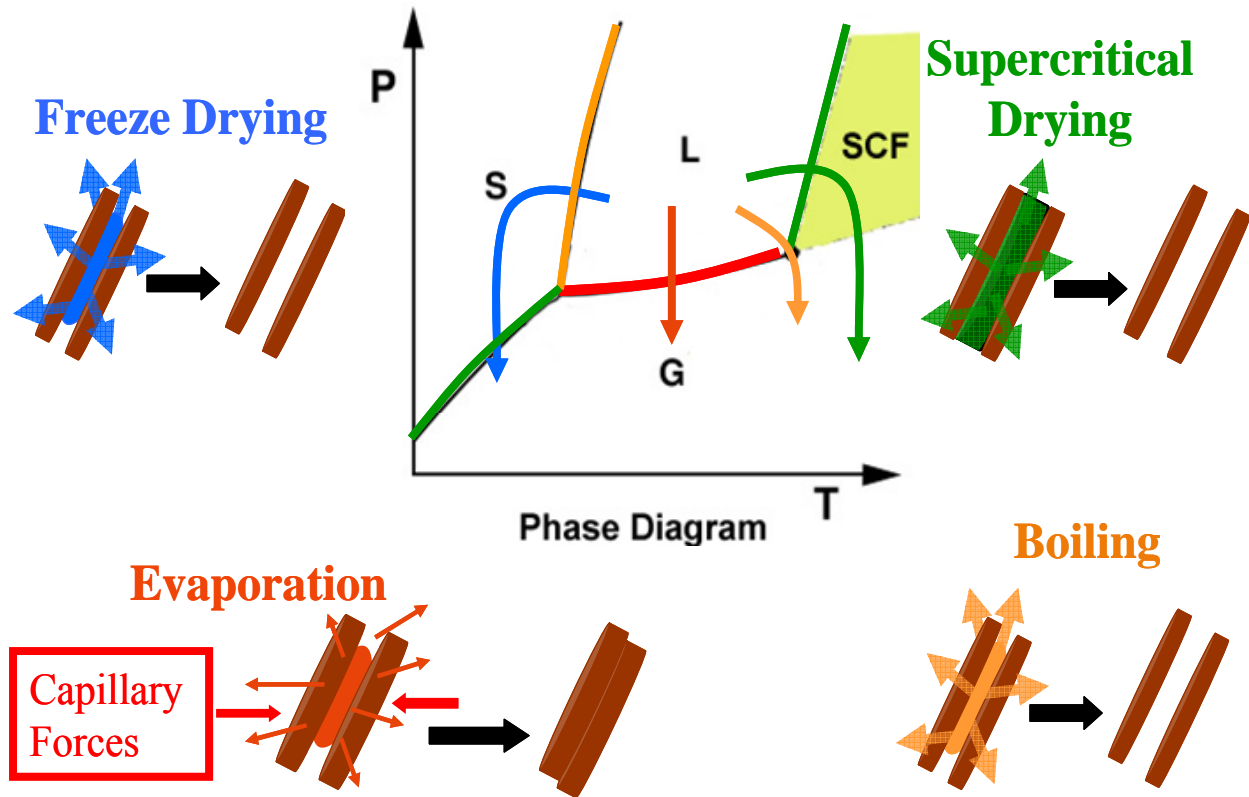


Figure 2-1. The Thermodynamics of drying methods. A depiction of the thermodynamic path across phase boundaries followed by each of the three drying processes investigated in this research. Evaporation crosses the gas-liquid phase boundary leading to capillary forces. During freeze drying, low temperature and low pressure are used and the liquid is first frozen then removed by sublimation. If the pressure is not sufficiently low, condensation is possible and will lead to capillary forces. The boiling method used high temperature and takes the liquid through the boiling point. Expansion of the liquid into a gas is used to overcome capillary forces. Supercritical drying takes a path to high temperature and high pressure completely avoiding the formation of capillary forces through the entire process.

CHAPTER 3 INTERPARTICLE FORCES IN AEROSOLS

Introduction

An aerosol is a dispersion of particles in air. Bulk powder is commonly disseminated to form the aerosol. The state of dispersion of the aerosol is governed by the conditions under which it is disseminated, the environment into which it is distributed, and the characteristics of the bulk powder from which it is taken. Particle properties are determined by the inherent nature of the powder, the interaction between particles on both the macro-scale and micro-scale, and the medium surrounding them. In order to improve aerosol dispersion, it is important to recognize all of the significant interactions that determine these properties and understand the correlation between them on the micro- and macro-scale.

The particle interactions consist of the sum of both the attractive (or cohesive) forces holding the particles together and the repulsive forces acting to separate them. The forces common to dry powder systems include attraction by van der Waals forces, cohesion by capillary forces in the presence of liquid bridges, and repulsion by electrostatic forces[67]. In addition, for the bulk state, the powder will also experience friction when in contact with other particles and shear forces as they move past each other. An illustration depicting these forces can be seen in Figure 3-1. Here F_{ad} is the force of adhesion due to van der Waals and capillary bridge forces, F_{es} is the electrostatic force, F_F and F_S are the friction and shear forces respectively acting at the particle level, and F and S are the overall normal and shear forces acting on the ensemble of particles. Each of these forces will now be examined in more detail in order to develop an understanding of their interactions in dry powder systems.

van der Waals Forces

The most common interparticle forces for powders in air arise from the electromagnetic interaction, coulombic attraction, or dipoles created by the separation of the positive and negative portions of atoms or molecules[68, 69]. These dipoles form a number of mechanisms including: the creation of fluctuating induced dipoles by vibrational motion, permanent dipoles, or polar molecules. There are three main contributions collectively called van der Waals forces which include: Keesom interactions, or dipole-dipole interactions; Debye interactions, or dipole – induced dipole interactions; and London dispersion interactions, or instantaneous, fluctuating dipole – induced dipole interactions. An illustration of these forces can be seen in Figure 3-2. London dispersion forces are considered to be the predominant part of van der Waals force between colloidal particles[70, 71].

The theory behind these forces was derived from the ideal gas law, which predicted the behavior of monatomic and simple diatomic gas. To explain the deviation of more complex molecules for the ideal gas law, Johannes D. van der Waals suggested a modification to the ideal gas law to include intermolecular interactions, and it became known as the van der Waals equation of state, Equation 3-1[71, 72].

$$\left(P - \frac{\alpha}{V^2}\right)(V - \beta) = RT \quad (3-1)$$

Here P is pressure, V is volume, R is the gas constant, T is temperature, and α and β are constants specific to a particular gas. The constant β describes the finite volume of the molecules comprising the gas, and the constant α takes into account the attractive forces between the molecules. After some time, a paired potential form of the equation for interaction included, for the first time, both an attractive and repulsive term. This would later become known as the commonly used Lennard–Jones potential, Equation 3-2 [73].

$$W_{a/a} = \frac{C}{r^6} + \frac{B}{r^{12}} \quad (3-2)$$

Here the net potential energy between two atoms, $W_{a/a}$, separated by a distance, r , is described by the competition of an attractive London dispersion force [74], C , related to the synchronization of instantaneous dipoles created when the energy fields of neighboring atoms overlap [75], and a Born repulsion term, B , arising from the overlap of electron clouds.

Microscopic Approach

In 1937 Hamaker expanded the concept of the van der Waals forces from single atoms and molecules to all atoms in solid bodies [70, 76]. He assumed that each atom in one body interacts with all atoms in another body and added these forces by a method known as pair wise summation. Bradley [77], Derjaguin [75], and [78] all followed Hamaker to improve the understanding of the forces acting between bodies. According to their approach, the interaction energy, W , of two spheres of equal size can be calculated by Equation 3-3. If the radius of the particles is much greater than the separation distance, the results can be simplified to the more common equation for the van der Waals energy of interaction between two spheres shown in Equation 3-4.

$$W_{sph/sph} = \frac{A}{6} \left[\frac{2R^2}{H(4R+H)} + \frac{2R^2}{(2R+H)^2} + \ln \left(1 - \frac{4R^2}{(2R+H)^2} \right) \right] \quad (3-3)$$

$$W_{sph/sph} = \frac{AD}{12H} \quad (3-4)$$

Here A is the Hamaker constant, R is the particle radius, H is the separation distance between the particle surfaces, and D is the particle diameter. One important aspect of this work is that the van der Waals forces can now be considered by the geometry of the body and an interaction term that is dependent only on the material properties, not shape. A compilation of the interaction forces and energies for various geometries can be seen in Table 3-1.

Macroscopic Approach

This microscopic approach does have one drawback; it does not take into account the effect of the interaction of dipoles within one body on other dipoles within the same body. In an attempt to include these interactions, Lifshitz [79] modified the Hamaker theory in 1956. Lifshitz ignored the atoms completely, assuming each material was a single body. He developed a calculation for van der Waals forces using the difference in dielectric properties. Equation 3-5 is the final expression Lifshitz derived for the Hamaker constant.

$$A_{132} = \frac{3}{2} k_B T \sum_{n=0}^{\infty} \left[\frac{\varepsilon_1(i\nu_n) - \varepsilon_3(i\nu_n)}{\varepsilon_1(i\nu_n) + \varepsilon_3(i\nu_n)} \right] \left[\frac{\varepsilon_2(i\nu_n) - \varepsilon_3(i\nu_n)}{\varepsilon_2(i\nu_n) + \varepsilon_3(i\nu_n)} \right] \quad (3-5)$$

Here the subscripts 1, 2, and 3 refer to material 1 and 2 interacting in medium 3; $k_B T$ is Boltzmann's constant times temperature; and $\varepsilon(\nu)$ is the dielectric permittivity of the material at a frequency, ν . There is some complexity involved in employing this equation as it is quite difficult to measure the dielectric response of materials over the wide range of frequencies required for the calculation. Work has been done by Ninham and Parsegian [80] and Hough and White [81] to simplify the measurement to specific characteristic frequencies in the ultraviolet (UV) range. The result is Equation 3-6, the Tabor-Winterton approximation [82].

$$A_{132} = \frac{3}{4} k_B T \left(\frac{\varepsilon_1 - \varepsilon_3}{\varepsilon_1 + \varepsilon_3} \right) \left(\frac{\varepsilon_2 - \varepsilon_3}{\varepsilon_2 + \varepsilon_3} \right) + \frac{3h\nu_e}{8\sqrt{2}} \frac{(n_1^2 - n_3^2)(n_2^2 - n_3^2)}{(n_1^2 + n_3^2)^{1/2} (n_2^2 + n_3^2)^{1/2} \left\{ (n_1^2 + n_3^2)^{1/2} + (n_2^2 + n_3^2)^{1/2} \right\}} \quad (3-6)$$

Again, the subscripts 1, 2, and 3 refer to material 1 and 2 interacting in medium 3; $k_B T$ is Boltzmann's constant times temperature; and $\varepsilon(\nu)$ is the dielectric permittivity of the material at a frequency, ν ; n_i is the refractive index of the respective material; and h is Plank's constant. It is interesting to note that where the medium and the solids have the same index of refraction ($n_1=n_2$

and $\epsilon_1 = \epsilon_2$) the Hamaker constant A_{132} goes to zero. This method is known as index matching and can be used to minimize or eliminate the effect of the Hamaker constant.

Up to this point, the relationships for interaction have used interaction energies, not the interaction force. For molecules, this is reasonable but as larger bodies are studied, force is of more interest. To overcome the challenges presented by the geometry of different surfaces, Derjaguin developed an approximation to relate the force of an interaction between a body of some geometry to the energy of interaction per unit area of two parallel flat surfaces [75]. To do so, the force is integrated over infinitely small, flat concentric rings of radius x and thickness dx on each body as the separation distance between the bodies, H' , goes from H to infinity as depicted in Figure 3-3. The relationship between the interaction force for bodies of different geometries and the interaction of planar surfaces can then be extracted making it possible to compare the interaction force of bodies of different sizes and geometries. For this reason, interaction force measurements are often reported as force normalized by radius. A list of factors that can be used to calculate the force of interaction from the energy of interaction of two plates of different geometries can be seen in Table 3-2.

Surface Energy Approach to Adhesion

In the previous section, the interaction between surfaces is determined as the surfaces are at some distance apart. However, when the surfaces are in contact, as is the case for powder in the bulk state, a different approach can also be considered using the surface energies of the surfaces described by the work of adhesion. Work of Adhesion is defined as the energy needed to separate two surfaces from contact to an infinite separation distance and takes into consideration the surface energy of the bodies in contact as seen in Equation 3-7 [83].

$$W_a = \gamma_{12} + \gamma_{23} \tag{3-7}$$

Here W_a is the work of adhesion, γ_{12} is the surface energy of one new surface 1 in medium 2 and γ_{23} is the surface energy of new surface 3 in medium 2. By combining Equation 3-7 with Equation 3-8, Young's equation, Equation 3-9 is obtained for the work of adhesion based on contact angle.

$$\gamma_{12}\cos \theta = \gamma_{23} - \gamma_{13} \quad (3-8)$$

Here γ_{12} is the surface energy at the liquid and vapor interface, γ_{23} is the surface energy at the solid and vapor interface, γ_{13} is the surface energy at the solid and liquid interface, and $\cos \theta$ is the angle between γ_{12} and γ_{13} through the liquid phase.

$$W_a = \gamma_{12} (1 + \cos \theta) \quad (3-9)$$

From this equation, the work of adhesion can be calculated by measuring the contact angle of a liquid, with a known surface energy, on the material of interest. By modifying the surface energies of the bodies through coatings and chemical surface modification, the work needed to separate them can also be modified. Doing so in a controlled manner can lead to the lowering of the cohesion between particles and thus the energy needed for dispersion.

Capillary Forces

Another important source of cohesion arises from capillary forces that form in the liquid pendulums between particles in the presence of liquid and is known to have a significant effect on the mechanical properties, transport, and dispersion of powder[2]. The first attempt to understand this cohesion in soil was made by Haines and Fisher[3, 84] and an expression for the force of cohesion due to the formation of aqueous liquid bridges was developed. Condensation of water vapor, present as relative humidity in the air, is sufficient to create liquid bridges[85, 86]. Since, most powder processing and transport occurs in ambient conditions, and in the presence of humidity, an understanding of the effect of capillary forces on dispersion is vital.

Liquid present in a particle system will collect at contact points between particles and form liquid bridges. Capillary forces in the liquid bridge will increase the cohesion between the particles at these points. For this reason, the degree of powder packing is an important factor of the system[87]. Close packed structures will have more particle contacts leading to a higher number of points for adhesion resulting in an increase in the powder strength. On the other hand, more open structures will have fewer contacts for adhesion leading to a weaker powder with a higher flowability. It can be readily seen that this phenomenon is very important for both the dispersion of dry powder from a reservoir, as in inhalers, and in the preservation of the powder dispersion after aerosolization. The equation for the attractive forces due to the presence of liquid bridges between two spheres is given in Equation 3-10.

$$F_{cap} = -2\pi R\gamma \cos \theta \quad (3-10)$$

Here R is the radius of the capillary, γ is the surface tension of the liquid phase, θ is the contact angle of the liquid at the particle surface, and the sign of the equation represents the force direction, which is cohesive in nature. The adhesion force due to the presence of a liquid bridge is calculated by the Laplace equation, Equation 3-11.

$$\Delta P = \gamma \left(\frac{1}{r_1} - \frac{1}{r_2} \right) \quad (3-11)$$

Here, ΔP is the pressure difference across the liquid interface, γ is the surface tension of the liquid and r_1 and r_2 are the radii of the particles. Decreasing particle size will therefore have a large effect on the adhesion force when liquid bridges are present.

Roughness

Up to this point, only ideal, smooth surfaces have been considered. However, this is unlikely for real surfaces. At the atomic level there will be roughness due to the size of atoms

and their spacing within the crystal structure. These perturbations on the particle surface will influence the effective interparticle spacing, the consequences of which are multifold since van der Waals forces are sensitive to the area of the surfaces in contact and separation distance between particles. The classical model for the effect of roughness on van der Waals adhesion was created by Rumpf [88, 89] and shown in Equation 3-12.

$$F_{ad} = \frac{A}{6H_o^2} \left[\frac{rR}{r+R} + \frac{R}{\left(1 + \frac{r}{H_o}\right)^2} \right] \quad (3-12)$$

Here A is the Hamaker constant, H is the interparticle separation distance, R is the radius of the particle, and r is the radius of the asperity on the surface. This model, however, significantly underestimated the adhesion force. The model has since been modified by others and research by Rabinovich and coworkers[53, 54, 90] has further refined the model to better predict experimental results, and in its final form is seen as Equation 3-13. Their work indicates that surface roughness on the nanometer scale (<2nm) greatly increases the force of adhesion, and as the scale of the roughness increases there is a subsequent decrease in adhesion forces.

$$F_{ad} = \frac{AR}{6H_o^2} \left[\frac{1}{\left(1 + \frac{32Rk_1rms}{\lambda^2}\right)} + \frac{1}{\left(1 + \frac{k_1rms}{H_o}\right)^2} \right] \quad (3-13)$$

The additional terms in this equation include k_1 , the maximum peak to peak height between asperities; rms, the root mean squared roughness of the surface; and λ , the average peak to peak distance between asperities. The first term accounts for the particle contact with the asperity

surface and the second term represents the interaction between the particle and the average surface plane.

Surface roughness will also decrease the minimum amount of water needed to form liquid bridges at particle contact points. Rabinovich and coworkers have investigated the effect of nanoscale surface roughness on the critical humidity required for the onset of capillary forces in such systems[49, 52, 55, 90, 91]. The presence of roughness on surfaces on a nanoscale has been shown to have a profound effect on the critical humidity required to induce capillary adhesion. Their study also validates a simple analytical expression developed to predict the force of adhesion as a function of particle size, humidity, and roughness, which is most relevant for practical systems. A visualization of the effect of surface roughness can be seen in Figure 3-4.

Esayanur [92] furthered this research by incorporating the friction coefficient, surface roughness, and the force of adhesion due to van der Waals forces into a single adhesion model. As a result, Equation 3-14 was developed:

$$f_c = \frac{4\gamma \cos \theta k_r n_l p (C n_c \rho_{sol})^{\frac{1}{2}}}{(k_h^{\frac{3}{2}}) R \cos \phi (3\rho_{liq})^{\frac{1}{2}}} + \frac{(k_r^{\frac{3}{2}}) \mu n n_l p}{R \cos \phi} \left(\frac{A_H}{12\pi H^2 K} + 2\gamma \cos \theta \right) \quad (3-14)$$

Here, the additional variables are: A_H , the Hamaker constant, H , the distance of closest approach, K , the roughness factor, and μ , the friction coefficient. The first term on the right side of Equation 3-14 represents the contribution of the liquid bridge (capillary) forces and the second term represents the adhesion force in the dry state.

Electrostatic Forces

Electrostatic force is also considered important for aerosol dispersion and has been the focus of research[9, 43, 46-48, 56, 58, 93-102]. Static electricity arises when charges on the surface of a material are not free to move to neutralize each other or do so slowly[45]. These

charges remain on the surface where they can interact with their surroundings. Particles with a similar net surface charge, greater in magnitude than the attractive forces, will experience coulombic repulsion, a force named after Charles Coulomb who was the first to measure these forces between glass spheres using a torsion balance he invented. Equation 3-15 shows the general equation for the electrostatic repulsive force.

$$F_e = \frac{q_1 q_2}{4 \pi \epsilon_0 r^2} \quad (3-15)$$

Here q_1 and q_2 are the charge on each particle, e_0 is the unit charge of an electron, and r is the radius of the particle.

Particles suspended in an aerosol continually gain, lose, and transfer charge between themselves and the surrounding environment. There are four basic ways by which charge can be imparted to the particle: (1) direct ionization, (2) ionization of particles by electromagnetic radiation, (3) static electrification, and (4) collisions with ions or ion clusters. Due to the low ratio of particle to air mass, the first mechanism is not considered significant[44, 45]. The latter two mechanisms are the most common and will be discussed in more detail.

Static electrification occurs when particles acquire charge from the surrounding environment. This can happen by any one or combination of the following five methods. (1) Electrolytic charging occurs when liquids of high dielectric constants exchange ions with the surfaces when they are in contact with particles. When the liquid is removed, a charge is left behind. This is not a significant source of charge for this reported research. (2) Electrons can also migrate from a clean, dry surface to another, dissimilar surface with a lower work function through contact electrification. This method is strictly electronic in nature and requires that there be no impurities between the surfaces making this unlikely to be important to real aerosols. (3) When particles come into contact with other particles or surfaces, charge can be imparted to

them because of this contact by tribo electrification, or frictional electrification. (4) In some cases the powders can be aerosolized as liquid suspensions and during evaporation the surface forces will increase the concentration of charges at the surface. (5) The last method is flame ionization where particles are ionized as they pass through the reaction zone of a flame.

Electromagnetic radiation such as ultraviolet or visible light can also be used to create charge by ionizing the particles instead of a flame.

Particles can also gain charge by collisions with electrons, ions, or ion clusters that can be produced from a number of different processes and types of electrical discharge. When an ion strikes a particle, it attaches to the surface[103, 104]. As charges accumulate on a particle an electric field will develop around the particle and prevent ions or electrons from reaching the particle. Therefore the accumulation will decrease as the charge on the particle increases and a point is reached where no further charging happens, this is called the saturation charge. Ions can move by thermal motion alone requiring no external force and as a result of diffusion charging. In order to make the process more efficient, an external electric field is applied to control the movement of ions[105-107]. Often, it is the combined occurrence of diffusion and field charging that leads to particle charging.

The most common method of ion production is by corona discharge. Two electrodes are arranged such that the field strength between them is constant, e.g. with a wire/tube or point/plane construction. The potential is increased until there is electrical breakdown of the gas around the point or wire and ions are forced to leave. These ions collide with gas molecules leading to electrical breakdown in the gas. Oppositely charges ions are drawn towards the wire and produce additional ions upon impact. This process creates a rapidly growing number of ions

with the same charge moving towards the electrode between which passing aerosol particles can be charged by collisions with these ions[15].

The amount of charge a particle can obtain by any of these methods is material dependent. The method is also ineffective above 50 percent relative humidity since the presence of water will nullify the charge[45, 47]. The presence of water does, however, lead to cohesion due to capillary forces, as discussed above.

Now that an understanding of the fundamental forces underlying adhesion between particles has been developed, their significance to the dispersion of powder in air will be presented through the experimental studies outlined in the following chapters.

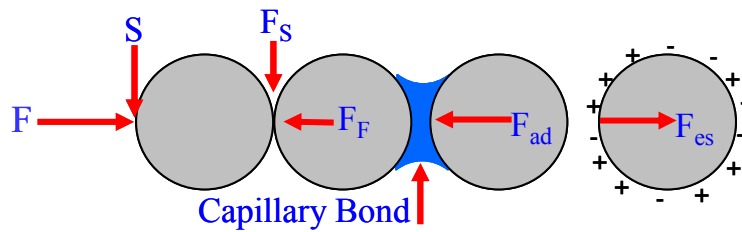


Figure 3-1. Illustration of important interparticle forces in powders and aerosols. Here F_{ad} is the force of adhesion due to van der Waals and capillary bridge forces, F_{es} is the electrostatic force, F_F and F_S are the friction and shear forces respectively acting at the particle level, and F and S are the overall normal and shear forces acting on the ensemble of particles.

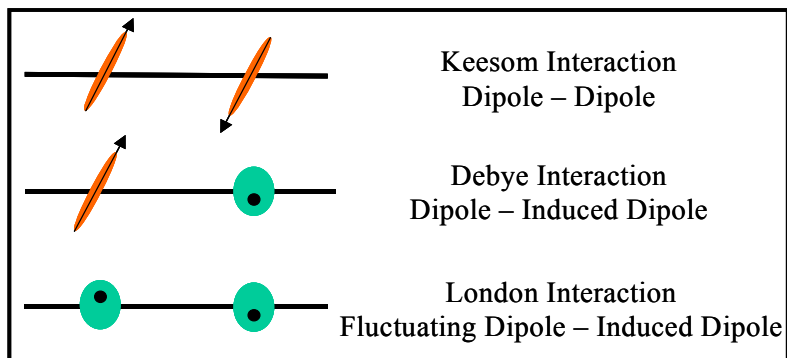


Figure 3-2. A depiction of the three interactions that are collectively known as van der Waals forces. van der Waals forces include: Keesom interactions, or dipole-dipole interactions; Debye interactions, or dipole – induced dipole interactions; and London dispersion interactions, or instantaneous, fluctuating dipole – induced dipole interactions.

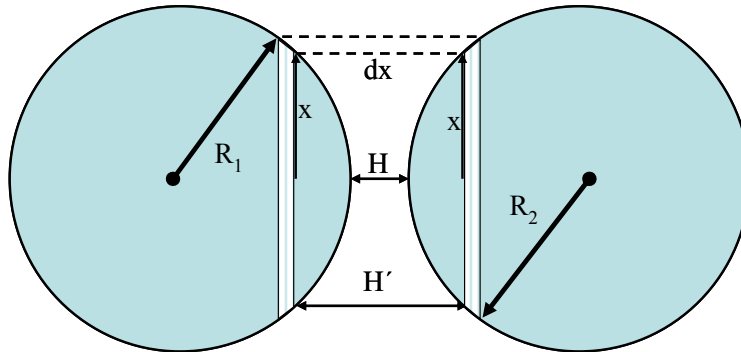


Figure 3-3. Depiction of the calculation of interparticle force using the Derjaguin Approximation. An approximation developed to relate the force of an interaction between a body of some geometry to the energy of interaction per unit area of two parallel flat surfaces. The force is integrated over infinitely small, flat concentric rings of radius x and thickness dx on each body as the separation distance between the bodies, H' , goes from H to infinity[75].



Figure 3-4. Change in contact area with increasing roughness. The illustration shows the decrease in contact area that occurs with increasing surface roughness and is attributed to the difference in interparticle forces between smooth and rough surfaces. Rumpf [19, 20] initially derived the equation for the contribution of surface asperities to the decrease in van der Waals forces. This work was later expanded by Rabinovich et al to more closely define surface roughness[53, 54] and include the effect of roughness on capillary forces[49, 55, 91, 108].

Table 3-1. van der Waals interaction forces and energies for different geometries. The theoretical equations for comparing interaction force and energy where A is the Hamaker Constant, H is surface separation distance, and R₁ and R₂ are the plate or sphere radii.

Interaction Geometry	Interaction Force	Interaction Energy
Plate – Plate	$\frac{A}{12\pi H^2}$	$\frac{A}{6\pi H^3}$
Sphere – Plate	$\frac{AR}{6H}$	$\frac{AR}{6H^2}$
Sphere – Sphere	$\frac{A}{6H} \frac{R_1 R_2}{(R_1 + R_2)}$	$\frac{A}{6H^2} \frac{R_1 R_2}{(R_1 + R_2)}$

Table 3-2. Interaction energy using the Derjaguin Approximation. A list of factors used to calculate interaction force from the interaction energy of two flat plates as determined by the Derjaguin Approximation. The interaction force, F, between different geometries can be calculated by multiplying the energy of interaction between two plates, W_{plt/plt}, by a geometry factor.

Interaction Geometries	Force	Energy
Plate – Sphere	F _{plt/sph}	(2πR)W _{plt/plt}
Sphere – Sphere	F _{sph/sph}	(πR)W _{plt/plt}

CHAPTER 4 MATERIALS AND METHODS

The first step towards realizing an increase in aerosol dispersion is a complete understanding of all interparticle forces significant to a given system. This requires a systematic study of single particle and bulk interaction measurements to determine the dominant forces between the powder particles on both the micro and macro scale. By measuring and understanding the dominant interparticle forces and how they change with the different factors, processing methods can be developed to reduce their magnitude so that the energy needed for dispersion is within the range of the current dissemination methods. Statistical experimental design was used to systematically investigate these factors to establish those significant to the aerosol dispersion as determined by particle size and settling measurements; bulk properties through shear cell experiments; and the magnitude of significant interparticle forces using the atomic force microscope. Figure 4-1 is a depiction of the direction of this research and is explained in more detail below.

Material

In this study, a variety of materials were used to investigate interparticle forces. To study the interactions between flakes, a vapor phase deposited (VPD) aluminum flake material was used, Sigma 1215, provided by Sigma Technologies, Inc. The material is vapor deposited onto a Mylar sheet using a continuous process until the desired thickness is achieved. The VPD process uses a laser to sputter molecules from a bulk of the pure material that then adsorb onto the substrate surface. The metal layer is then removed from the Mylar and milled into flakes in ethyl alcohol to dissolve any residual polymer and inhibit oxidation of the aluminum. Through this process the flake thickness can be carefully controlled and is designated by the numeric value following the name. For example Sigma 1215 signifies that those flakes are 12-15 nanometers

thick. Unlike flakes produced by milling, which requires milling aids such as stearic acid that change the surface chemistry of the particles, the VPD result is a bare aluminum flake with a thin controllable native oxide layer suspended in alcohol.

Flakes are not suitable for compaction and shear tests, however, because they are susceptible to mechanical deformation leading to physical interlocking under those conditions. Once the flakes are mechanically connected, the investigation of interparticle forces is impossible since the particles can no longer slide past each other, a condition required for bulk powder testing. For this reason, atomized aluminum spherical powder from Valimet, Inc was used for the shear measurements.

To create a surface for contact angle and interparticle force measurements, aluminum was also deposited onto a silicon wafer using a chemical vapor deposition (CVD) process. By this process, the precursor is vaporized and the gaseous molecules flow into the reactor. At the reaction zone, they adsorb onto the substrate surface after which thermal energy is added to aid in their decomposition and formation of a solid film. This produces a smooth, near-ideal surface that enables the investigation of surface energy and how it changed with surface modification.

Experimental Factors and Processing Methods

A number of factors are involved in powder dispersion and will vary between systems. They include powder drying method, relative humidity, surface modification, flow aids such as second phase particles, and dispersion medium. These parameters were systematically varied and the resulting powder was characterized in order to determine the degree of dispersion. First, the material itself was characterized before and after processing to determine the particle size and morphology of the materials. The surface energy was determined for the ideal surfaces using contact angle measurements. Next, the aerosol dispersion was characterized experimentally through particle size, airborne concentration and settling. The first means used to characterize

the degree of dispersion of the aerosol was by comparing the particle size distribution in a well-dispersed state; i.e. measurement of the primary particle size, to that measured after processing in the dry state. The settling rate and disseminated concentration of the powders in an Air Dispersion Chamber fabricated in house was also employed to study the aerosol by using laser attenuation and the Beer-Lambert Law as will be explained in more detail below.

Dispersion is complex and the change in the significant forces involved and their magnitude must also be investigated. Therefore dispersion was also studied theoretically on the macro scale by treating the powder as a continuum using shear cell measurements and on the micro scale by investigating the interparticle forces between individual particles using the Atomic Force Microscope (AFM). These results, coupled with the aerosolized particle size distribution data under different conditions, give insight into the mechanism of adhesion and the processing methods that can be used to successfully lower adhesion and thereby improve dispersion. As seen in Figure 4-1, the experimental factors chosen for this research were drying methods, surface modification, humidity, spacer materials, and dispersion medium. Each effect was determined by two sets of experiments. First, experiments were performed to investigate the change in particle size, aerosolization, and, settling. Second, those results were compared to the change in micro and macro scale force measurements made using the shear cell and atomic force microscope (AFM) measurements.

Drying Method

Liquid, whether water due to humidity or processing methods, must be removed from the powder in a way that does not lead to the formation of liquid bridges and capillary forces. Common drying methods were described in detail in Chapter 2. For this investigation, material was dried using evaporation under vacuum, freeze drying, and a liquid CO₂ supercritical fluid processing method for powders developed during this research, then the particle size of the

resulting powder was measured using laser diffraction. A depiction of each of these drying methods as they relate to a general thermodynamic phase diagram is given in Figure 4-2.

For evaporation and freeze drying, the effect of liquid surface tension was investigated by dispersing the powder in water and isopropyl alcohol. It was found that water is not miscible in liquid CO₂ thus only isopropyl alcohol was used. For the evaporation process, the dispersed suspensions were placed in a vacuum oven at 40°C and -20psi for 24 hours. The resulting cake was broken up with a spatula followed by particle size analysis. The process for freeze drying included placing the water suspensions in the freezer overnight then transferring them to the freeze drying vacuum chamber. Suspensions in alcohol were frozen by mixing the suspension in liquid nitrogen then transferring the frozen sample to the freeze drying vacuum chamber.

The supercritical drying method developed for the research involved a slightly different process than the conventional methods and is shown by the green line in Figure 4-2. To avoid the inherent challenges of mixing the powder directly in liquid CO₂, i.e. the laws of thermodynamics that made CO₂ a liquid only above 800psi, the powder was first dispersed in isopropyl alcohol then solvent exchanged with liquid CO₂ in a pressure reactor using a batch solvent exchange process. Once no alcohol was left, the pressure reactor was heated above 32°C at which point the pressure in the reactor was above 1060psi, the critical point of CO₂. Above the critical point, the surface tension of CO₂ is negligible and capillary forces cease to exist. The supercritical fluid is vented from the chamber as a gas and as long as the temperature is above the critical temperature, T_c, it cannot re-condense back to a liquid and capillary forces are eliminated.

Spacer Material

High aspect ratio particles have a very high mass to surface area ratio. That is, because the thickness of the flake is an order of magnitude smaller than the diameter the contact area between

the flakes is very high while the mass to which momentum can be applied is very low. Associated with the high surface area are also high attractive surface forces, especially van der Waals forces. For these reasons, once the surfaces come into contact, dispersion can become impossible. If the contact area between flakes is decreased, the adhesion between them will also be decreased and dispersion can be improved, as described in Chapter 3. The spacer material used was a 10nm mean diameter superhydrophobic fumed silica, Degussa Aerosil® LE2. The addition of the silica can also have a negative effect: since the silica is not the material of interest, the addition of silica past the point of improving dispersion will decrease the amount of desired material available to be dispersed. Therefore, the spacer was added at 0, 5, 10 weight percent.

Relative Humidity

Powders can be subjected to a wide range of humidity levels during processing and aerosolization. Adsorption of water onto the particle due to humidity leads to particle adhesion by the formation of liquid bridges and capillary adhesion. It was shown in Chapter 3 that there is a critical humidity at which the liquid bridge forms. Since the effect of humidity has such a profound effect on adhesion, it is important to understand at what point it becomes significant (critical humidity level) and how this factor will change the powder system. Therefore, humidity levels in the range of 10-90 percent have been selected. The relative humidity will be increased in 40 percent intervals to allow the full range of possible environments to be studied. Each powder was conditioned at the given humidity for 48 hours to allow for equilibration prior to experimentation. To do so, the samples were placed into the chamber and humid air was pumped through the chamber for 48 hours prior to measurements to allow the powders time to equilibrate. Humidity was controlled by pumping dry, compressed air through a water trap and by controlling the temperature of the water. Humidity levels were controlled to within $\pm 2\%$.

Surface Modification

Capillary forces are determined by the amount of water adsorbed onto the particle surfaces at their point of contact. The ability of water to condense on the surface of a particle is determined by the ability of the water to wet the particle surface and controlled by surface energy of the water and of the particle surface. By changing the surface energy of the powder through surface modification, the powder can be made hydrophobic and thus water cannot wet the surface. This can be done by attaching monomers to the surface with hydrocarbon chain tails. Water molecules no longer can see the aluminum surface, but instead see a surface with which it is not thermodynamically favorable for them to interact. In order to investigate this, the aluminum surface was modified with two types of silanes. The first, Octydecyltrimethoxysilane (ODTMS), is a tri-functional monomer. That is, the silicon has three bonds that are used to create a two dimensional structure on the aluminum. One bond attaches to the surface and the other two attach to the neighboring monomers. The second silane used was (TDFS). In addition to creating a hydrophobic surface, the Teflon aspect of this particular silane is thought to also decrease the surface energy between the particles much like it can between eggs and a Teflon coated frying pan. The reaction time between the silane and the surface was also investigated to determine the optimum processing time needed to achieve the highest hydrophobicity.

Dispersion Medium

Liquid Carbon Dioxide Assisted Aerosolization: As part of the experimental research, a novel dispersion method has also been developed. This dispersion method utilizes liquid CO₂ as a propellant and source of energy for dispersion. Powder particles to be aerosolized are suspended in Liquid CO₂. The suspension is then released such that the liquid instantaneously undergoes a phase change to a gas, the thermodynamically stable phase at standard room temperature and pressure. The phase change causes an expansion in the volume of the CO₂ and

in turn creates added stresses from within the agglomerate pushing outward significantly increasing the degree of dispersion.

This dispersion method has advantages over other dispersion methods regardless of the dominant interparticle forces. Liquid CO₂ at room temperature resides at a pressure of 800psi. This pressure will supply a large amount of energy to the agglomerates in the form of high velocities leading to tremendous shear, turbulence, and impaction. Pressure changes can also be increased further with the use of nozzles. The instantaneous phase change and expansion of the CO₂ will add to the energy of dispersion by supplying dispersion force in an outward direction.

The state of dispersion of the powder in the liquid CO₂ is also important as an increased state of dispersion in the liquid phase is expected to lead to higher dispersion upon aerosolization. Technology for the dispersion of particles in liquid CO₂ has been developed and implemented in the dry cleaning industry already[59, 60, 109, 110]. Surfactants have been developed with a “CO₂-philic” end and a “CO₂-phobic”. This surfactant is used to disperse particles in a similar way to surfactants in aqueous mediums such as detergents. This technology can be leveraged to aid in this dispersion method.

Characterization Methods

Particle Size and Morphology

All materials underwent the same rigorous characterization protocol upon receipt. For particle size, this included using the appropriate light scattering instrument for the size range of the powder, optical image analysis, and scanning electron microscopy (SEM).

Laser Light Scattering The light scattering instrument used for particle between 40nm and 2mm was the Beckman Coulter LS13320. It is based on the principle that particles scatter and diffract light at certain angles based on their size, shape, and optical properties. A 750nm diode laser is used for analysis of particles in the size range of 0.4µm to 2000µm. The beam

passes through filters as well as projection and Fourier lenses and is spatially recorded on 126 photodiode detectors. The Polarization Intensity Differential Scattering (PIDS) assembly is used to measure particles from 40 nm to 400 nm and improves resolution in the 400 nm to 800 nm range. PIDS uses a tungsten-halogen lamp and three sets of vertically and horizontally polarized color filters at 450, 600, and 900 nm as the light source. The technique is based on the principle that at high scattering angles (~ 90 degrees) the difference in scattering intensity of the two polarizations is a function of the particle size to wavelength ratio.

The advantages of this technique include ease of operation, large range of detectable particle sizes, and accuracy in the micron and submicron range. The calculations assume the scattering pattern is due to single scattering events by spherical particles of the same refractive index. This raised some questions since this study involved high aspect ratio particles, i.e. flakes, and mixtures. For flakes moving in turbulence past that laser, it is not the actual diameter being measured but the average random orientation of the flake. However, when using a differential volume distribution, the particle size is weighted towards large particles, which in this case is the maximum diameter. Mixtures on the other hand, could not be measured using this instrument as there is no way to simultaneously determine the scattering pattern from two materials of a different refractive index and other methods were used. The LS13320 has two sample modules which made it ideal for this research: a fluid module and a dry powder module. This allows for the measurement of the powders in a wet, well dispersed state and again after processing and drying using the same instrument. All samples in liquid were placed in a sonic bath for twenty minutes before measurement to insure complete dispersion. While all dry materials were sampled according to the appropriate methods before the measurements. The results presented in this work are an average of at least three measurements.

Dynamic Light Scattering Powders with a mean diameter less than 10 nm, particularly the spacer materials, were measured using the Microtrac Nanotrak NPA250 dynamic light scattering instrument. It is capable of measuring particles between 0.8nm and 6.5 μm based on dynamic light scattering by measurement of the velocities of particles undergoing Brownian motion in a liquid. This motion is detected by measuring the spectrum of Doppler-shifted photons from light scattered by the particles. Photons scattered from particles moving away from the scattering photon have their frequency lowered. A photon scattering from a particle moving towards it has its scattered frequency increased. The instrument compares the frequency shifted photons to unshifted photons, recording the difference or beat frequency of the interfering photons. The Brownian velocity of particles is inversely proportional to particle size and becomes quite significant if the particle dimensions are less than 1 μm . By measuring the spectrum of Doppler shifted frequencies, the particle velocity distribution and, hence, the particle size distribution can be determined. All materials in a liquid medium were placed in an ultrasonic bath for a minimum of twenty minutes prior to measurement to insure dispersion. Small and more agglomerated materials required up to one hour of ultrasonication. All results presented are an average of at least three measurements.

Scanning Electron Microscopy SEM images of the particles were taken using the JEOL 6330, a cold field emission scanning electron microscope. Cold field emission scopes have the advantage of high brightness and high resolution even at low accelerating voltages to allow imaging of a wide variety of materials including soft polymeric materials without causing sample damage. Resolution of the instrument is around 15 Angstroms depending on the sample. The JEOL 6330 is equipped with an energy dispersive X-ray spectrometer (EDS) for elemental analysis and a backscattered electron detector that allows compositional analysis.

Optical Microscopy and Image Analysis The Olympus BX60 optical microscope is equipped with a SPOT Insight Digital Camera. The SPOT RT is a "three pass" charge coupled device (CCD) digital color camera suitable for taking digital images of a particulate sample. The SPOT RT is cooled to 37°C below room temperature to reduce thermal noise inherent in CCD devices. It is equipped with dual light sources for both transmitted and reflectance imaging. It can be operated in the bright field, dark field, and differential interference contrast (DIC) modes. Five objectives from 5 – 100 times magnification are available. Image Pro v. 6.2 Optical Analysis Software analyzes digital pictures taken of particles. Particle properties such as size, shape, roundness, aspect ratio, and percent image coverage can be measured. All particle size distributions were made from images of at least 10,000 particles to insure statistical significance[19].

Material Surface Energy

Ramé-Hart Contact Angle Goniometer In order to understand the effect of surface modification on the material, advancing and receding contact angle measurements were made before and after surface modification of the material with a Rame-Hart Contact Angle Goniometer. This instrument consists of a stage for droplet formation on a material surface, a digital camera for image acquisition, and software for data analysis. Ten to fifteen images of the advancing and receding contact angle of a water drop on each surface were taken and the average of the measurement made from these images is reported. The significance of the different contact angles is presented in Chapter 3.

Dispersion Characterization

To determine the effect of processing methods on improving dispersion, the degree of dispersion, or dispersability, of the aerosol was measured by two methods. For single materials the comparing the particle size measured by laser light scattering was used. By comparing the

primary particle size measured in a wet, well dispersed state, to that of the powder after processing and drying, the degree of dispersion can be seen by the shift in mean particle size. For mixtures with different indices of refraction, airborne concentration and settling rate measurements of the powders were made in a chamber fabricated for the FTIR.

Particle size comparison

The first method used to determine the degree of dispersion was by measuring the particle size using the Beckman/Coulter LS13 320. The LS13320 has two sample modules that made it ideal for this research: a fluid module and a dry powder module. Because of this, powders could be measured in a wet, well dispersed state then processed and dried and measured as a dry powder in the same particle size instrument. A comparison of the two particle size distributions yields a measurement of the degree of dispersion. Agglomeration can be seen by both an increase in the mean particle size, and an increase in the width of the particle size distribution. Complete dispersion is achieved if both particle size measurements are equal.

Settling measurements

Air Dispersion Chamber for the Fourier Transform Infrared Spectrometer: In order to characterize dispersion as aerosols, a lab scale air dispersion chamber was fabricated that fits into the Thermo Electron Magna 760 FTIR Microscope. The chamber, with a volume of five liters, fits into the FTIR such that the IR laser can pass through the windows of the chamber to the detector. A picture of the FTIR Air Chamber in place can be seen in Figure 4-3A. The design of the chamber allows for the induction of powder by low vacuum, -12.5psi, or a variety of positive pressures produced by the use of an N₂ cylinder, 5-90psi, or a CO₂ cylinder, 800psi gas or liquid. The IR laser passes through the disseminated aerosol cloud and the intensity is measured by the FTIR detector and reported at percent transmission. A schematic of an aerosol measurement in the chamber after dissemination can be seen in Figure 4-3B. Transmission (T) is

measured over time and graphed as the negative log of one divided by transmission. The graph of time versus the log of one divided by transmission is indicative of settling rate. A slower settling rate would result from a smaller particle size by increased dispersion. If a constant mass of material is used, from which a constant concentration is assumed immediately after dissemination, the mass extinction coefficient of the Beer-Lambert Law, Equation 4-1, can be calculated and used to determine the airborne concentration over time.

$$\text{Beer-Lambert Law:} \quad -\text{Log}(1/T) = M_e * C * PL \quad (4-1)$$

Here T is transmission, M_e is the mass extinction coefficient, C is concentration, and PL is the path length of the laser through the aerosol cloud and assumed to be the diameter of the chamber.

Powder Mechanics

Shear Cell There are many methods available to measure the cohesive forces of bulk powders including measurement of the shear strength or tensile strength of a powder compact, angle of repose, and powder flow behavior. In this study the bulk properties was measured using the Sci-Tec ShearScan bulk powder tester. A diagram of the Sci-Tec ShearScan is seen in Figure 4-4. This method offers the most simplicity and several models have been developed to relate the tensile strength to interparticle force.

For a typical measurement, powder is loaded into the cell, which has an annular geometry and covered by a lid. A load is applied to the lid by the overhead piston pushing down onto the powder causing consolidation. The lid of the cell is then rotated by the piston and the torque applied to the lid by the powder is measured with a load cell connected to the base of the test cell. The shear stress versus distance sheared data recorded at each normal load is used to generate the Yield Locus. Mohr's circles are drawn tangent to the Yield Locus, one of which will pass through the origin. The Mohr circle is a two dimensional representation of all the equivalent states of stress that describes the Unconfined Yield Stress (f_c) in terms of a shear

stress (τ) and a normal stress (σ) that correspond to the major principal stresses (σ_1, σ_3) acting on the system.

A typical direct shear test of a powder is performed by consolidating the sample at a given normal load then lowering the normal load and determining the shear stress required to initiate flow (failure) in the sample. From a graph of the stress versus distance sheared consolidation state of a powder and the subsequent failure stress that leads to incipient flow in the system can be determined, as shown in Figure 4-5. The yield locus is the line tangent to the failure Mohr circles, and the slope of the yield locus is called the angle of internal friction of the powder. The unconfined yield strength is defined as the yield stress of a bulk sample at a given consolidation load where one of the major principal stresses equal to zero. A zero stress on one of the axes represents a powder not confined in the direction of the stress, which is the case during powder flow of powder.

A set of yield loci is generated at consolidation loads of 2.5kpa, 5kpa, 10kpa, 20kpa, and 30kpa. The unconfined yield strength verses the major principle stress, σ_1 , is plotted at each consolidation load to generate a flow function. The flow function defines the change in strength of the powder, measured as f_c , as a function of the applied consolidation load. A flow function is generated for each powder at each relative humidity level to determine the change in f_c . Each flow function reported in this research is an average of at least four repeats of a given relative humidity and consolidation load.

Apart from the unconfined yield strength, the Mohr circle also enables the determination of the cohesion (C) and the angle of internal friction (angle of repose, ϕ) both of which are bulk parameters characterizing the flow characteristics of the powder. The unconfined yield strength (f_c) and principle stresses ($\sigma_{1,2}$) can then be determined as shown in Figure 4-5.

Interparticle Forces

Atomic Force Microscope (AFM) The properties of the powder as a bulk give insight about the strength and flowability of the powder but not all of the information needed to understand powder cohesion and how it relates to dispersion. In order to determine the forces on the particle level, an Asylum Research AFM was used. A humidity cell accessory was utilized to measure and control the humidity in the sample chamber. With this instrument, the significant interparticle forces and their magnitude can be measured for each of the surfaces at the relative humidity values. This is done to determine the effect of the surface coatings and humidity on the interparticle forces that are dominant at different conditions and methods that can be used to help overcome them.

Interparticle force measurements were made on each surface with an AFM cantilever according to the methods described by Ducker et al and Rabinovich[111, 112]. For the measurement, the cantilever was positioned close to the flat substrate. Then, as the AFM tip assembly is moved towards and away from the surface by a piezoelectric column, the deflection of the cantilever is monitored by a diode laser that reflected off the top of the cantilever onto a position sensitive photodiode. As the cantilever is attracted to or repelled from the surface, depending on the situation, the amount of deflection is measured by the position of the laser on the photodiode, as shown in Figure 4-6A. By this procedure, the force between the two surfaces as a function of separation distance and cantilever spring constant was obtained, and representation of this can be seen in Figure 4-6B. The approaching portion of the force curve is characterized by a jump-to point as the tip is attracted to the surface and can be seen by the black solid line in Figure 4-7. Once the tip is in contact with the surface, the piezoelectric column raises the assembly away from the surface. The cantilever will bend until the force holding the cantilever tip to the surface is greater than its spring constant at which time it springs back to the

normal position. The retraction portion of the force/distance curve can be represented by the red dotted line in Figure 4-7.

The force/distance profiles were then normalized by dividing the measured force by the radius of the sphere thereby allowing the data to be presented in terms of energy per unit area of a flat surface. This enables the determination of interaction force for different geometries as long as the range of the forces is much less than the radius of curvature of the particles interacting. Force measurements were taken at four different spots on each surface and an average force of fifteen measurements at each spot was reported.

Design of Experiments

The order of experiments performed was determined by developing a statistical design using the Design Expert 6 software package. Doing so has two advantages. First, it allows evaluation of the error associated both within the experiments of one condition and that between the different conditions. This will help separate experimental error from the results allowing a more accurate evaluation of the factors under investigation. Second, the software will provide an equation based on the model developed to fit that data and the factors chosen to be significant. From this equation, the optimum result within the experimental design space can be reached. In addition, it will also aid in determining what direction to move the experimental space if the highest value has not been reached. A design was developed for the airborne concentration experiments, shear cell measurements, and interparticle force measurements. A comparison of the results was used to develop the correlation between the change in processing, powder forces, and dispersion.

The results to the work outlined in Chapter 4 will be presented in Chapter 5. The results for the particle size and settling and the bulk and interparticle force measurements will be

discussed as well as a correlation of the data. The conclusions developed during this research will be explained in Chapter 6 and applied in a case study described in Chapter 7.

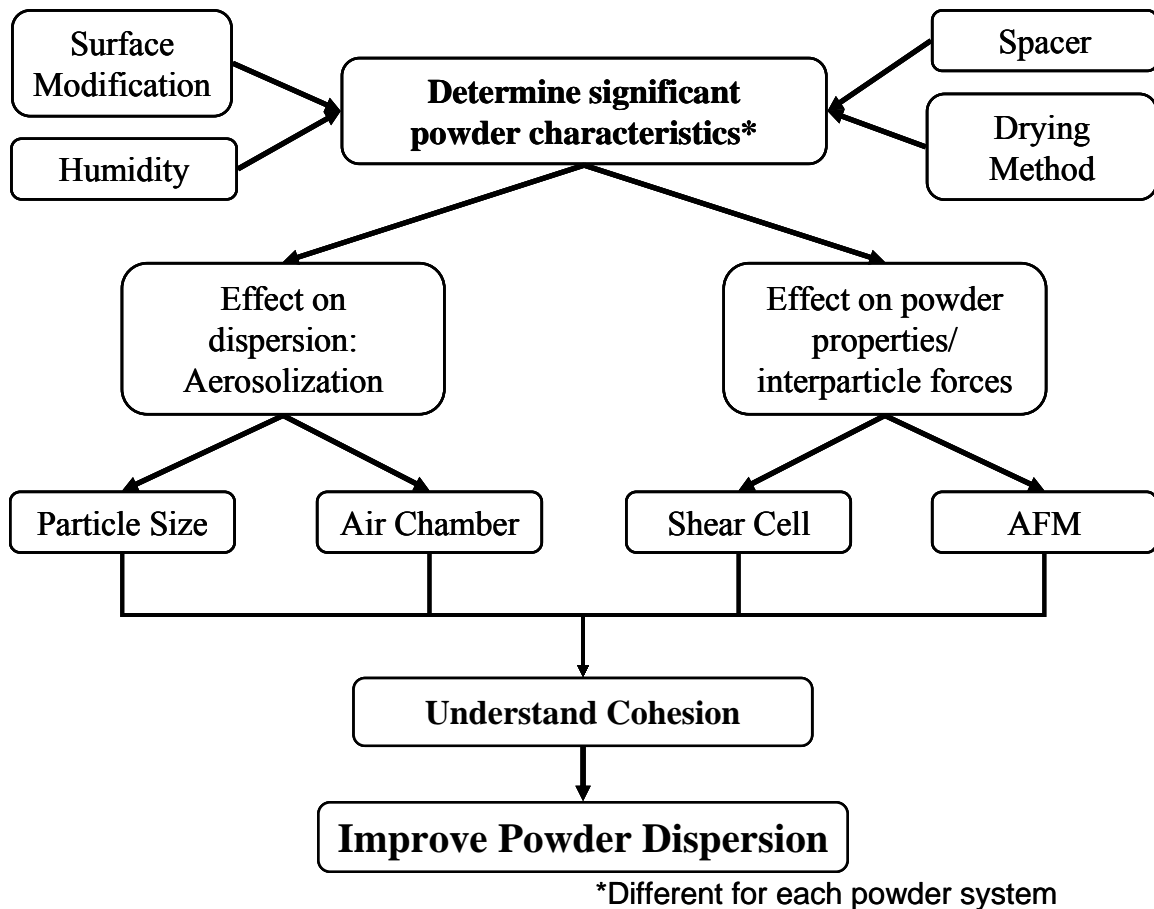


Figure 4-1. A roadmap to dispersion: depiction of the direction for the presented research. Design of experiments was employed to determine the magnitude of the effect of factors that have been shown in literature to effect dispersion in air. Experimental results are compared to theory and micro and macro scale force measurements to develop an understanding of their significance, magnitude, and change with processing.

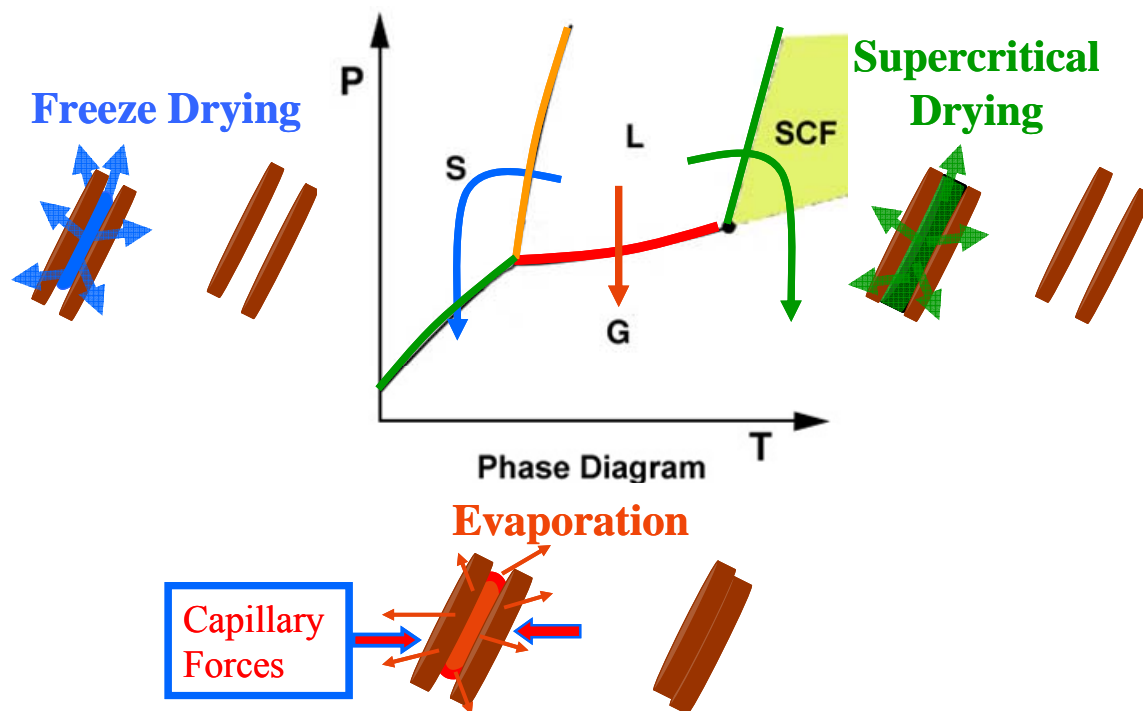


Figure 4-2. Thermodynamic path of drying methods investigated. A depiction of the thermodynamic path across phase boundaries followed by each of the three drying processes investigated in this research. Evaporation crosses the gas-liquid phase boundary leading to capillary forces and agglomeration. Freeze drying takes the liquid to low pressure and temperature as it is first frozen then removed by sublimation. If the pressure is not sufficiently low, condensation is possible and will lead to capillary forces. Supercritical drying takes a path to high temperature and pressure completely avoiding the formation of capillary forces through the entire process. The best results were found using the supercritical process.

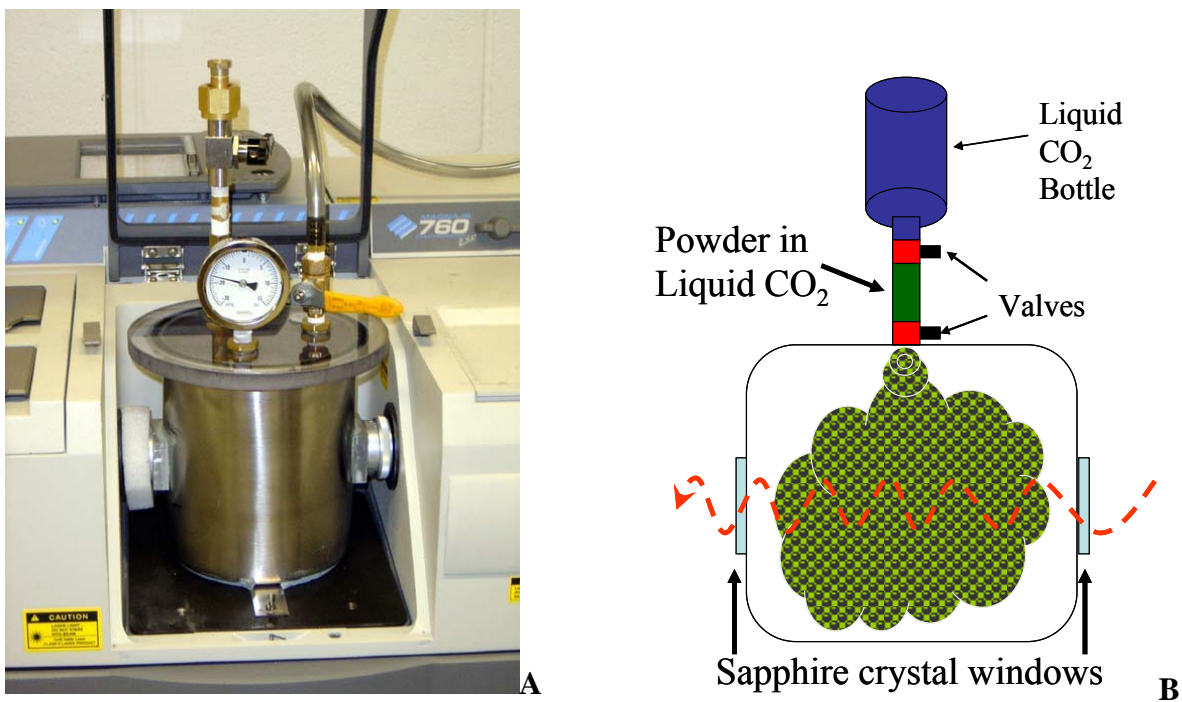


Figure 4-3. Images of the Air dispersion chamber. A) is a photograph of the air dispersion chamber when positioned in the FTIR during an experiment. B) is a schematic of the chamber showing the laser path through an aerosol cloud produced in the chamber. The aerosol can be produce by high pressure gas or a volatile medium.

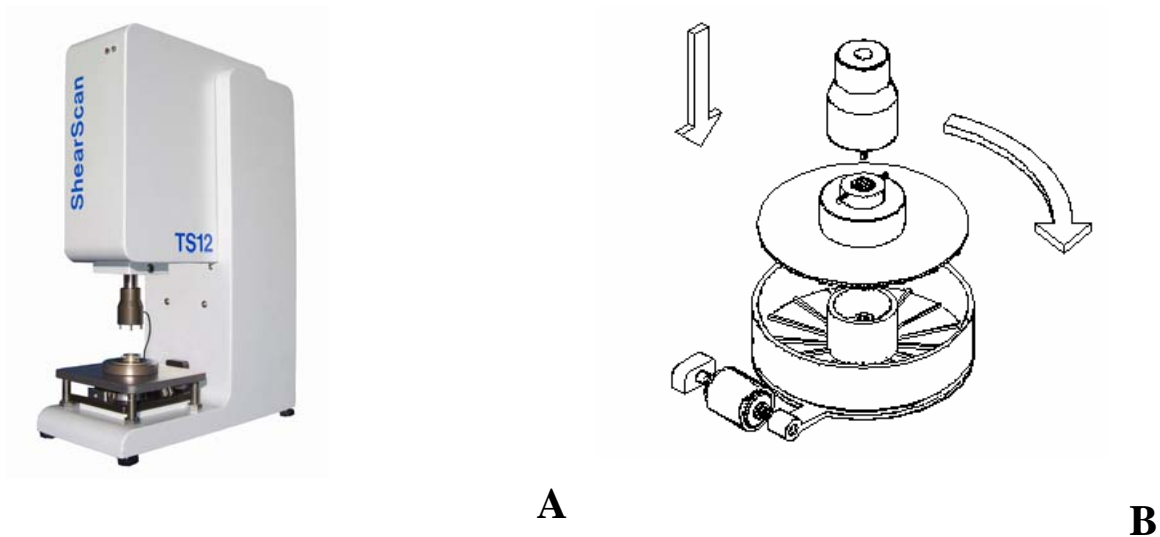


Figure 4-4. The Sci-Tec ShearScan TS12 shear tester and test cell. A) shows a photograph of the Sci-Tec ShearScan instrument. B) depicts the compression cell used for the measurements. Powder is loaded into the cell and a consolidation load is applied by the piston from above as it rotates. The torque applied is measured by the load cell attached to the base.

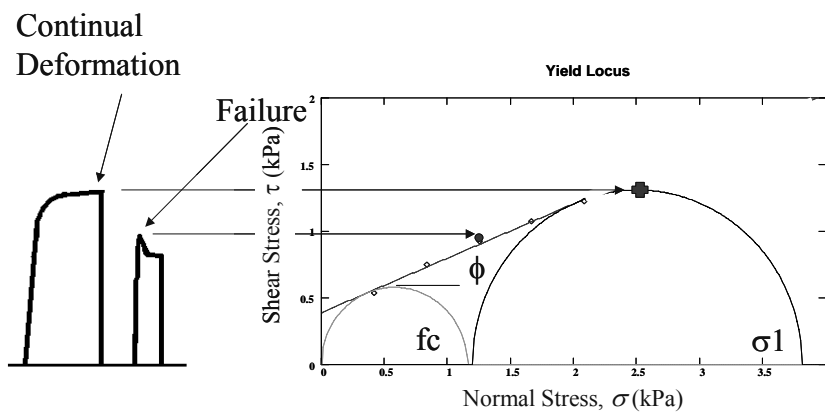


Figure 4-5. A typical result from the consolidation and failure of a powder sample. The corresponding points on the Mohr circle are shown to illustrate the procedure of generating the Yield Locus, the major principle stress, sigma one, and the unconfined yield strength, f_c .

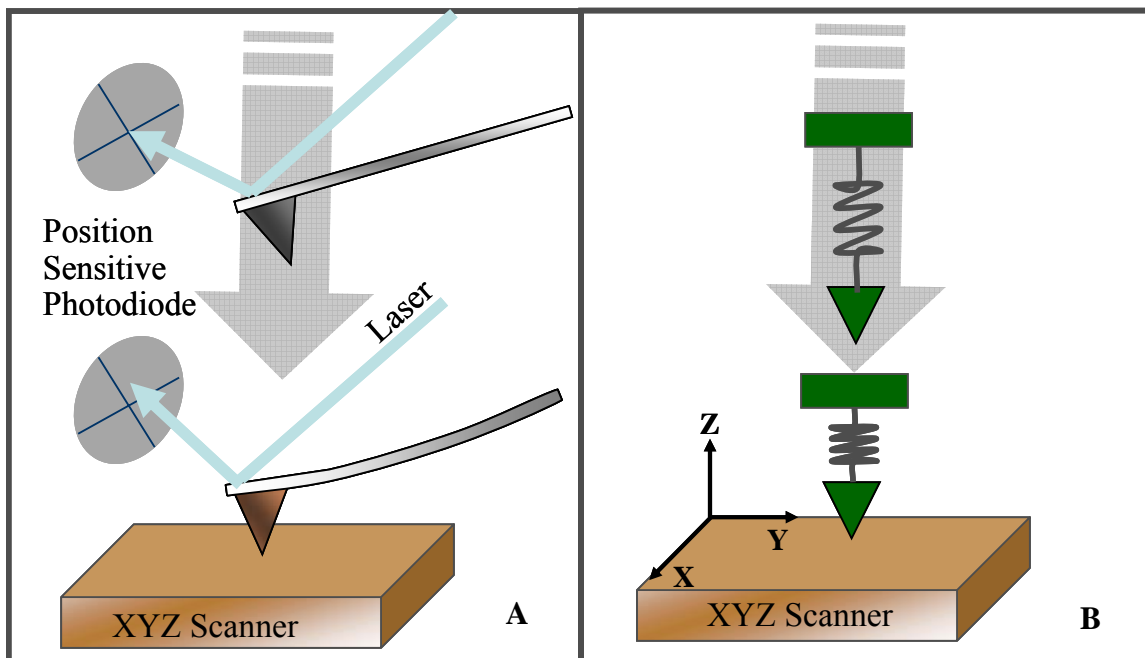


Figure 4-6. Schematic of how the AFM works. A) A laser is reflected off the end of the cantilever onto a position sensitive photodiode. The cantilever is brought close to the sample, on a moveable stage, and the interaction between them causes the cantilever to move. The movement is measured by the change in position of the laser on the photodiode. B) The measured cantilever movement and its spring constant allow calculation of the interaction forces. Cantilevers of varying compositions and spring constants allow for a large range of measurement options.

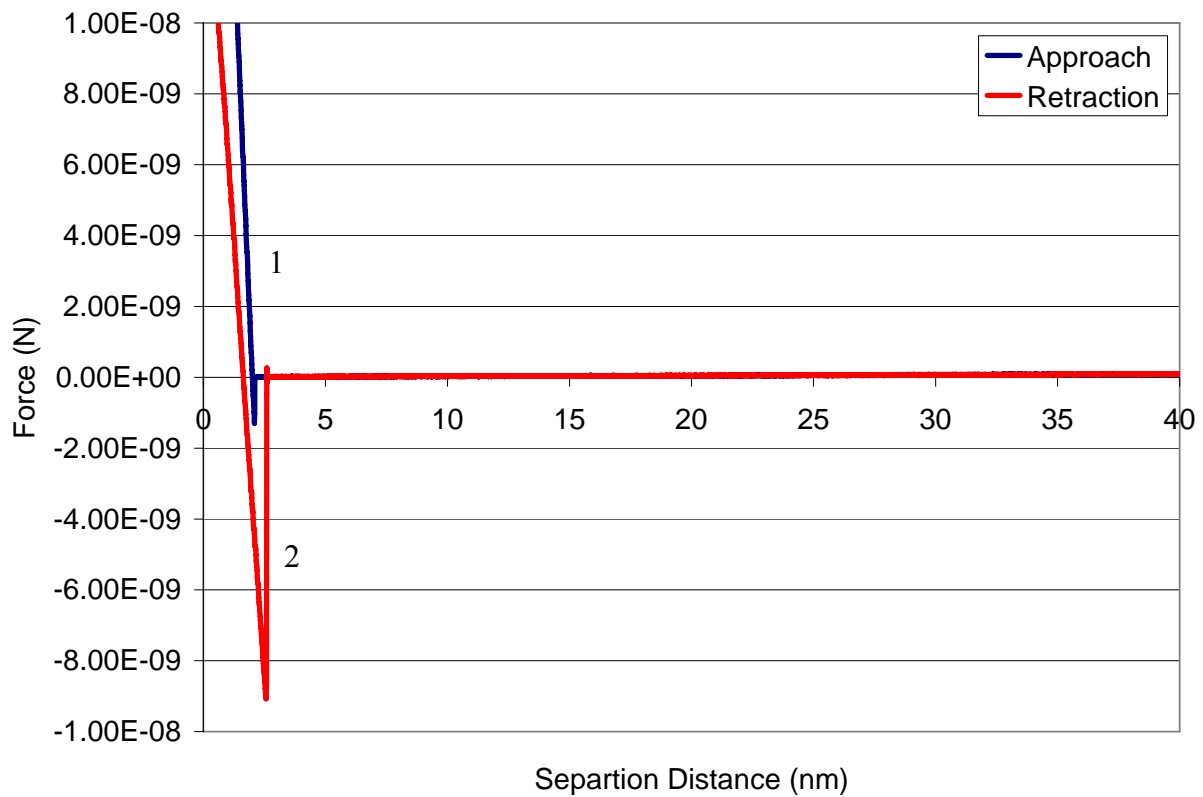


Figure 4-7. Example of a force distance curve for the AFM. The cantilever approach is depicted by line 1 and characterized by the jump to surface point at 2.5nm. After this point, the piezoelectric increases the separation distance and the adhesion force is calculated using the height of the retraction curve shown by line 2.

CHAPTER 5 RESULTS AND DISCUSSION

Characterization

Particle Size of Single Materials

All materials were characterized prior to experimentation. Particle size was measured using laser diffraction and compared to image analysis and SEM images. The non-spherical nature of the aluminum material and the mixture of materials with a different index of refraction presented new challenges for common characterization techniques such as laser diffraction. Laser diffraction uses the scattering pattern produced by the laser interaction with the particles and the index of refraction of the material to calculate a particle size. The first assumption required to make accurate measurements is that the particles are spherical and the second is that the scattering pattern is produced by only one index of refraction. Laser light scattering is an efficient and repeatable sizing method; therefore the use of this method for flakes was further investigated. To do so, both assumptions must be further understood.

The orientation of the particles as they move past the laser is random and cannot be controlled. A spherical particle does not have an effect due to orientation, a flake, however, does. Although flakes can be considered spherical in two dimensions, they cannot be considered spherical in the third, their thickness. Two important concepts must also be taken into account. First, the differential volume distribution produced by light scattering is weighted towards the larger particle sizes. This is because only a few 10 μ m particles will have a much larger volume than an even higher number of sub micron particles. Second, statistically the instrument will measure the average random orientation of the particles being measured due to the fact that the flow field past the laser is turbulent and therefore the orientation of the particles will constantly be changing. For these reasons it can be expected that light scattering will measure the average

random orientation of the flake and, using a volume distribution, the size will be weighted towards the diameter of the particles. To test this hypothesis, particle size distribution measurements made of pure aluminum flakes suspended in isopropyl alcohol using the Beckman/Coulter LS 13320 laser diffraction instrument were compared to those made using image analysis as describe in Chapter 4. The results can be seen in Figure 5-1, which shows the graph of particle size distribution produced by both laser diffraction and image analysis. The difference can be explained by the method of particle size measurement used for each instrument. Image analysis measures the maximum particle diameter of the flakes as they lay flat on the microscope slide, whereas laser diffraction is measuring the average random orientation of the flakes as they move pass the laser in a liquid suspension; the average random orientation always being smaller than the maximum diameter. However, the difference between them is consistent. It was therefore determined that laser diffraction is suitable to measure the size of flakes if it is acknowledged that the reported particle size is typically 25 percent smaller than the maximum dimension.

The laser diffraction pattern used to calculate the particle size is obtained by a simultaneous measurement of the laser intensity on a number of detectors placed at different angles from the normal laser position. It is impossible to decipher which particles produce the pattern. For this reason the particle size measure of a sample made up of a mixture of materials each with a different index of refraction is inaccurate. This led to the use of other measurement methods to determine the degree of dispersion of the samples to which spacer materials were added and will be described below.

The spherical aluminum material from Valimet, Inc used for the shear cell measurements was also characterized using laser diffraction. Figure 5-2 shows the particle size distribution with a mean diameter of 4 μ m and a log normal distribution from 1-10 μ m.

Particle Size of Mixtures

The characterization of mixtures and the degree of dispersion posed new challenges. Due to each material having a unique index of refraction, laser diffraction could not be used to characterize dispersion. A new method was developed using the attenuation of light in a settling chamber built for the FTIR. The powder can be disseminated by pulling a partial vacuum on the chamber or by pressure using a compressed gas or liquid cylinder. Once the powder is disseminated, measurements of the laser transmission through the particle cloud are made over time. These transmission measurements can then be used to calculate airborne concentration using the Beer-Lambert Law, Equation 4-1, and effective particle size using the Stokes settling equation explained in more detail below[113, 114]. From these the degree of dispersion can be determined and with it the effectiveness of the processing and dissemination methods for that sample.

Morphology

To obtain a better understanding of particle morphology, images of all of the particles were taken using the scanning electron microscope (SEM). Figure 5-3 shows SEM images of the VPD aluminum flakes. A face of one flake is shown in Figure 5-3A. The irregular shape of the flake shown in this image is indicative of the milling process which was used to produce it after vapor deposition onto the Mylar sheet. Edges of a number of flakes can be seen in Figure 5-3B and the large diameter to thickness ratio can be readily appreciated. It is interesting to note in Figure 5-3B, that the flakes are so thin that some are becoming transparent to the electron beam and the stack of flakes can be seen under the flakes laying on top. Transmission electron

microscope pictures were also taken of the flakes to study the formation of the oxide coating at the flake edges. The images were taken with the assistance of Kerry Siebein at the Major Analytical Instrumentation Center, Department of Materials Science and Engineering, University of Florida. As seen in Figure 5-4 a uniform and continuous oxide layer is present and the aluminum below the oxide layer is preserved.

The atomic force microscope (AFM) was also used to characterize the flake morphology as well as surface roughness. A standard silicon nitride cantilever was used to image the flakes deposited onto a silica surface. The image of two flakes can be seen in Figure 5-5. The irregular edges of the flakes can be seen as well as some large scale roughness which is expected to be attrited pieces of aluminum generated during the milling process. Higher magnification images of the flake surface can be seen in Figure 5-6 and show that the flake itself has a very smooth surface. The root mean squared (rms) surface roughness of the flakes was measured, using the AFM, to be 4nm.

SEM images of the Valimet spherical aluminum were also taken and seen in Figure 5-7. It is apparent from the image that the material has a broad particle size as observed in the particle size measurements, Figure 5-2.

Drying Methods

For drying, each sample was mixed in water or isopropyl alcohol (IPA) and sonicated for 30 minutes to insure the powder was dispersed. For oven drying, the suspension was then placed in a vacuum oven at 60°C and -25 inches Hg for 24 hours to dry. For freeze drying, the samples were pipetted into liquid nitrogen to freeze them, and then placed in the freeze dryer. For SC fluid drying with liquid CO₂, the powders were dispersed in IPA, as water is not highly miscible in CO₂. As this is a new process for drying powders, it will be looked at in more detail.

A custom designed Parr Instruments pressure reactor was used for the supercritical drying. Solvent exchanges were performed to completely replace the isopropyl alcohol medium with liquid CO₂. After this was completed, the chamber was heated to a temperature above the supercritical state of liquid CO₂, held to allow for the temperature throughout pressure vessel to reach equilibrium, and then slowly released. This process is depicted by the CO₂ phase diagram in Figure 5-8. The process starts at room temperature where the liquid CO₂ is at 800psi inside the pressurized chamber, point A in Figure 5-8. The chamber is heated until a temperature above 31°Celsius at which point a pressure above 1072 psi is reached, the critical point of carbon dioxide, and held for at least thirty minutes to insure the chamber and its contents equilibrate to this temperature, seen as point B in Figure 5-8. A pin valve on the top of the chamber is then opened to release the supercritical fluid as a gas at a rate no greater than three liters per minute until the pressure in the chamber returned to 0 psi.

The results for drying can be seen in Figure 5-9, the particle size distribution of each material made after drying. Evaporation is represented by the red curve. As the liquid evaporates, capillary forces draw the particles together, so that attractive van der Waals forces cause the particles to agglomerate. The agglomeration can be seen in the particle size distribution which has a large mean particle size and wide distribution. During freeze drying, the inability to maintain sufficiently low pressure during the length of the drying process leads to the condensation of water vapor and the formation of liquid bridges and capillary forces. This was determined to be due to the limitations of the vacuum pump to maintain the pressure required to sublime the frozen liquid. The resulting material produced by supercritical drying using liquid CO₂ is shown to be the most dispersible in Figure 5-9. This material has the smallest particle size and narrowest distribution of all the processes investigated due to the fact that supercritical

drying completely avoids the gas-liquid phase boundary throughout all steps of the process. The primary particle size distribution of the material, measured by dispersion in isopropyl alcohol is shown for a comparison. Despite the improvement provided by supercritical processing, completely removing the capillary forces during drying was not alone sufficient enough to produce a completely dispersible powder. Although drying was shown to have a significant effect on powder dispersion, other factors that influence dispersion must also be taken into account in order to achieve a fully dispersed powder. Aside from capillary forces, van der Waals forces are always present between particles and are very significant when particles are in close proximity. Reducing the van der Waals attraction will increase the dispersability of the powder and will now be discussed.

Aerosol Experiments

Spacer Addition

van der Waals forces are generally accepted to be significant only at short ranges, often considered less than 50nm. Therefore, by maintaining some separation between the particles the van der Waals attraction will decrease. Surface roughness also impacts van der Waals forces in two ways. First, the asperities on the surface lead to a less intimate contact and a lower total contact area. Second, distance between the average surface plane is increased. This can be seen in Figure 5-10, an illustration of the effect of roughness on two flat surfaces. The surfaces to the left are smooth and are seen to be in intimate contact. The surfaces in the center and to the right illustrate increasing roughness. The contact area between the flakes can be seen to decrease and the distance between the average surface plains increase with increasing roughness. This was first shown by Rumpf [88, 89] who derived an equation for the effect of roughness on van der Waals forces to explain the difference between the calculated and measured adhesion force of two surfaces as seen by Equation 3-12.

Recently, Rabinovich et al. further expanded this equation to better account for the true geometry of the surface taking into account not only asperity height but asperity width and peak to peak distance as well[53, 54] and shown in Equation 3-13. The effect roughness has on van der Waals force can be seen by comparing the force distance curves the smooth rough surfaces as shown in Figure 5-11. Here the van der Waals force of attraction is plotted versus separation distance. Curve 1 shows the attractive forces for two smooth surfaces using the plate-plate equation in Table 3-1 and curve 2 shows the attractive forces for the same size flakes with a 4nm RMS surface roughness as calculated by the PERC Model, Equation 3-13. As seen in Figure 5-11, this increase in surface roughness has a dramatic effect of decreasing surface forces. By applying this idea towards particles to be disseminated, decreasing the attractive forces will lead to an improvement in dispersion.

The surface roughness of the aluminum flakes cannot be altered easily. However, by adding a spacer particle between the flakes, roughness can be in effect simulated as illustrated in Figure 5-12. The fumed silica is nearly the same size as the flake thickness, 10nm, and has a lower Hamaker constant than aluminum 6.55×10^{-20} J as opposed to 1.5×10^{-19} J respectively[83]. The combination of these two effects will reduce the interparticle forces. The significant decrease in the magnitude of the forces can be seen in Figure 5-13, a comparison of the calculated force distance curve for smooth aluminum flakes 12 μ m in diameter and 12nm thick alone; with the addition of five weight percent fumed silica; and with the addition of ten weight percent fumed silica. There is a slight increase in interaction forces at ten weight percent silica because of the increasing number of contacts with increasing silica addition. Based on these calculations, experiments were conducted to investigate the true effect of adding Degussa Aerosil LE2 fumed silica to the flakes.

The silica was added to the aluminum flakes suspended in isopropyl alcohol before supercritical drying. SEM images of the flakes alone and mixtures with silica can be seen in Figure 5-14 A-C. Figure 5-14 A shows the flakes themselves, their smooth surface can easily be seen. Figure 5-14 B is an image of the mixture of flakes with five weight percent silica added. The silica is seen to be attached to the flake surfaces thereby increasing the interparticle spacing. Figure 5-14 C shows the mixture with ten weight percent silica added. The silica is distributed evenly throughout the sample; however large agglomerates of the silica can be seen indicating that dispersion of the spacer material is also important. It was determined from this information that ten weight percent silica was in excess of what was needed therefore experiments were carried out with mixtures of five weight percent Degussa Aerosil LE2 fumed silica added to the aluminum flakes.

For each experiment, a sample of 3.85 ± 0.05 mg of material was disseminated into the FTIR Air Chamber and measurements were taken as the powder settled. The data was plotted as the log of inverse transmission over time as seen by the blue points connected by a line in Figure 5-15. The slope of this line is indicative of the settling rate since the transmission is decreasing due to the powder settling out of suspension in the air[114]. A trend line is added to the data and the trend line equation displayed on the graph, which is shown in Figure 5-15. Repeats of each sample were run and the trend line equations used to determine the average and standard deviation for each condition. This was used to insure statistical significance between results. The graph in Figure 5-16 shows a typical standard deviation for a given set of conditions. The average is depicted by the solid line and the standard deviation is given by the dashed lines.

Settling times of interest were chosen to be one second, taken to be the maximum initial dispersion; ten seconds, a time of interest for both pharmaceutical powders and other aerosol

applications; and one hundred seconds, a length of time considered to be in excess of most applications but interesting for the point of view of total aerosol lifetime. Using the average settling rate, as shown in Figure 5-16, along with knowledge of the initial material mass and the Beer Lambert Law, Equation 4-1, the airborne concentration can be calculated. An example of the results can be shown in Figure 5-17, the airborne concentration of aluminum flakes produced by 12psig vacuum induction into the chamber. From the graph, it is seen the 66% of the powder was introduced into the aerosol. Using this type of graph, the maximum airborne concentration of powder produced and the effective settling rate can be compared for the different conditions. These measurements are made by laser attenuation, thus increasing airborne concentration is accomplished by increasing the number of flakes scattering the light and thus increasing dispersion. Very large agglomerates will not be aerosolized and fall directly to the bottom of the chamber. Smaller agglomerates settle out very quickly and will be seen in a rapid settling rate. A well dispersed powder will have a high initial airborne concentration and maintain a higher concentration over the selected measurement time.

Samples containing five weight percent silica were then disseminated using the same partial vacuum pressure. As determined above, the silica is expected to reduce the interparticle forces and this is, in fact, confirmed by the settling results. Figure 5-18 shows a comparison of the airborne concentration for the vacuum disseminated aluminum and aluminum containing the silica. The addition of the silica increased dispersion and lead to a seven percent increase in airborne concentration. The settling rate was comparable to the aluminum alone and the airborne concentration has room for further improvement. The partial vacuum induction method uses a relatively low pressure and so the effect of increasing dissemination pressure was subsequently investigated.

To study the effect of pressure a compressed gas cylinder was attached to the induction tube after the sample was loaded. Using compressed nitrogen pressures from 5-90psig were safely attainable. However, experimentation at a higher pressure was also desired and for this a compressed gas carbon dioxide cylinder was employed for a test pressure of 800psig. The results are seen in Figure 5-19, a plot of the airborne concentration over time of aluminum disseminated using the varying pressure. As expected, increasing pressure resulted in a higher airborne concentration and a slower settling rate. The addition of silica was also investigated at 800psi. Figure 5-20 shows the airborne concentration for samples disseminated with and without silica. The sample with silica disseminated by 800psig gas carbon dioxide showed a decrease in airborne concentration. In none of these experiments, did the airborne concentration reach 100 percent, thus inviting further consideration of the dispersion method.

As discussed in Chapter 3, turbulent flow is associated with fluctuations in velocity called eddies which impart energy to break up agglomerates, and a minimum eddy size determined by pipe diameter and air flow velocity. Particles smaller than the minimum eddy size would be able to follow the velocity gradient and not be dispersed[45]. Using the maximum pressure, 800psig, the minimum eddy size for this system was determined to be 1.2 μ m. Taking into consideration that the flakes are 12 μ m in diameter but only 12nm thick and that the force needs to be applied along the thickness such that the flakes can be separated, it was determined that even at high pressures, the minimum eddy size was larger than that needed to separate flakes from intimate contact. To do so would require higher pressures or the application of the pressure in a different way. Instead of applying the dispersion force only by linear methods such as turbulence and drag, perhaps adding a radial component from inside the agglomerate acting outward would increase dispersion.

Dispersion Medium

Turbulence, although effective for larger particles, has a minimum turbulent eddy size of $1.2\mu\text{m}$ for this setup that limits the smallest agglomerate that can experience dispersion forces during dissemination. In order to overcome this challenge, turbulence was coupled with a volatile medium, liquid carbon dioxide. By this method, not only will there be the high pressure, 800psi, available to create turbulence for dispersion, in addition there will be a radial outward force that will develop as the liquid carbon dioxide is released and undergoes a phase change from liquid to gas. An illustration of this idea is provided in Figure 5-21. Taking into account the change in density, the change in volume associated with the phase change under ideal conditions and neglecting any temperature change due to Joule cooling, an increase in volume of approximately 500 times is calculated. Taking the sample chamber volume to be 3cc, this is calculated to be a force of $3\mu\text{N}$ per flake. Considering that the van der Waals force calculated by the PERC Model and shown in Figure 5-11 is $132\mu\text{N}$ this force is two orders of magnitude less than that required for dispersion. If the flake and silica mixture is considered, an interparticle force of $16\mu\text{N}$ is calculated. For this case, neglecting all other forces acting on the particles, the expansion force of the liquid CO_2 alone is near the force needed for dispersion. This additional force, in combination with the 800psi dissemination pressure is expected to further improve dispersion.

For these experiments, after the sample was loaded, a liquid carbon dioxide cylinder with a siphon tube was connected and the sample chamber filled. The measurement protocol described above was used. The aluminum flakes were disseminated using the liquid and the results are seen in Figure 5-22, a plot of airborne concentration at select times. The maximum initial airborne concentration was calculated to be only 65%, a value less than that measured previously

by 800psi gas dispersion as seen in Figure 5-23. From this result and further consideration of the phase change process, the following two conclusions were drawn. First, the volume of liquid actually between the flakes must be considered. The flakes are smooth and once in contact, very little liquid will be able to penetrate the space between them. If this happens, the liquid does not expand from between the flakes and no extra dispersion force is achieved. Second, it is considered that the liquid to gas phase change was not, in actuality, instantaneous. Because of this time delay, a meniscus of liquid carbon dioxide can form between the flakes. The low surface tension of liquid carbon dioxide would wet the particles and capillary forces would draw the particles closer together increasing the adhesion force. The addition of a spacer in this case would increase the interparticle spacing, increasing the amount of liquid carbon dioxide between the flakes and decrease the area over which capillary forces can act.

A simple evaluation of the interparticle volume for two flakes with an rms roughness of 4nm is calculated to be 0.6nm^3 , while adding five weight percent spacer increases that volume by a factor of three to 1.5nm^3 . Experimentally the effect can be seen by the increase in airborne concentration in Figure 5-24. The addition of the spacer shows a twenty percent increase in airborne concentration over that of liquid alone. In addition, the settling rate of the mixture is shown to be slower a second indication of improved dispersion. The same conclusion is drawn when the liquid carbon dioxide results are compared to those of the gas, Figure 5-25; the mixture disseminated using liquid carbon dioxide provides the best results.

Perfect dispersion has not yet been achieved and other factors must also be considered. Due to the readiness of moisture from the environment to adsorb onto the particles, and the significant increase in adhesion created by capillary forces, surface modification to neutralize the effect of humidity will next be investigated.

Surface Modification

Capillary forces between particles caused by the condensation of water from the atmosphere can lead to a significant increase in particle adhesion and in turn decrease the dispersability of the powder. This can readily be seen by the change in particle size distribution of aluminum flakes in Figure 5-26 after conditioning at 20, 50, and 80% relative humidity for 48 hours. The particle size is seen to increase with relative humidity as capillary forces increase the adhesion between the particles. The primary particle size is shown for a comparison.

The surface hydrophobicity of aluminum was changed by surface modification using *n*-octadecyltrimethoxysilane (ODTMS) and tridecafluoro-1,1,2,2-tetrahydrooctyl-1-triethoxysilane (TDFS). For surface modification, 2% (by volume) solutions of ODTMS and TDFS were made as follows. 2 mL of silane and 0.5 mL of water was placed into 100 mL of ethanol which was adjusted to a pH of 5 using glacial acetic acid.

Measuring the macroscopic contact angle of a drop on powders is challenging due to particle surface roughness and the porosity of a packed bed of powder and due to the small particle diameter, traditional particle contact angle methods were not employed. Thus, in order to determine the optimum reaction time to produce the most hydrophobic surface, surfaces were produced by chemical vapor deposition of aluminum onto polished silicon wafers were used which is more conducive to contact angle measurements. 1 cm x 1 cm square samples were cut from larger wafers and the samples were reacted with ODTMS and TDFS as described above. Samples were stored in a clean and dry desiccator and prior to contact angle measurement, samples were rinsed with methanol and water and then dried in a clean drying oven.

High purity water (Barnstead Nanopure Infinity, $18 \text{ M}\Omega\cdot\text{cm}^{-1}$) was used to measure advancing and receding contact angles with a Ramé Hart contact angle goniometer as described previously and contact angle images were captured with a digital camera. Contact angles were

determined from digital images using the ImageJ software package (Version 1.36b). All contact angle measurements were performed at 22°C, atmospheric pressure and 50% RH. Figure 5-27 shows examples of digital images used for contact angle measurements of bare aluminum, A, and aluminum surface modified with ODTMS and TDFS, B and C respectively.

The results for reaction time can be seen in Figure 5-28, a plot of the change in advancing and receding contact angle of water on the ODTMS modified aluminum surface at varying reaction times. The contact angle on the bare aluminum surface is represented at time zero with a contact angle of $67 \pm 3^\circ$. The advancing contact angle is represented by the solid line and measurement points are indicated by the closed diamonds. As the aluminum surface was mixed in the solution, an increase in contact angle was seen and a maximum of $114 \pm 1^\circ$ obtained at one hour. After this point, a plateau is reached and the contact angle remained constant up to 12 hours of mixing after which there was a decrease. This is expected, as with time a bi-layer or other surface complex begins to form causing polar end groups to be exposed to the environment as opposed to the hydrophobic non-polar ends. The receding contact angle is represented by the dashed line and the corresponding measurement points are indicated by the open circles. The receding contact angle followed a similar trend to that observed by the advancing measurements.

The change in the contact angle of water on surfaces modified with TDFS is shown in Figure 5-29. Again, the bare aluminum, with a contact angle of $67 \pm 3^\circ$ is seen at time zero. The advancing contact angle is shown by the solid line and closed circles to rapidly increase to a maximum of $111 \pm 3^\circ$ after one hour. As with the ODTMS, a plateau is reached between 1 and 12 hours after which a decrease in contact angle is seen. The receding contact angle, represented by the dashed line and open circles, also shows similar trends to that of the advancing measurements.

Contact angle measurements were also used to calculate the work of adhesion between the surface and a water droplet, shown in Table 5-1. The effect of the hydrophobic silane surface coating on the work of adhesion is most pronounced in the advancing measurements where on an untreated surface, the work of adhesion was 101 mJ/m^2 , and in comparison, the work of adhesion on the treated aluminum surfaces was 43 and 44 mJ/m^2 for TDFS and ODTMS respectively. Similar decreases were observed in the work of adhesion calculated from receding measurements.

The advancing and receding work of adhesion are both important to consider with respect to the agglomeration and separation between two surfaces where condensed liquids are present. Hydrophobic surfaces with low contact angle hysteresis exhibit lower values of work of adhesion. Thus two hydrophobic surfaces joined by a liquid bridge would be less likely to agglomerate by capillary forces and therefore should also be easier to separate. Hydrophobic particles under humid conditions should therefore display lower values for bulk powder strength compared with hydrophilic particles and also be easier to disperse back to their primary particle size.

Based on the preceding results, the aluminum flakes were surface modified with ODTMS for one hour, rinsed by dilution and centrifugation, and supercritical dried. Figure 5-30A-C shows examples of digital images taken of a water drop on a layer of the aluminum flakes deposited on a glass slide. Figure 5-30A shows the contact angle of a water drop on a bed of bare aluminum flakes, Figure 5-30B shows a water drop on a bed of aluminum flakes modified with ODTMS, and Figure 5-30C shows a water drop on TDFS modified flakes. It is important to note that due to the particle surface roughness and flake bed porosity, these measurements do not

represent the contact angle of water on the flake but instead are the effective contact angle of a similarly treated flat surface.

After drying, all three samples of the flakes were conditioned at 50% relative humidity for 48 hours prior to dissemination in the air chamber. Liquid carbon dioxide was used to disseminate the flakes for measurement. The airborne concentration of the bare and ODTMS surface modified flakes at 50% relative humidity disseminated using liquid CO₂ can be seen in Figure 5-31. No significant change in airborne concentration is observed. To further investigate this, bare aluminum flakes were conditioned at 20, 50, and 80% relative humidity for 48 hrs then disseminated into the air chamber using liquid CO₂. As seen in Figure 5-32 no significant change in airborne concentration or settling rate can be seen with increasing humidity. This led to the conclusion that using liquid carbon dioxide to disseminate the powder overwhelmed any effect of prior powder conditioning on dispersion.

Design of Experiments

The order of the airborne concentration experiments performed above was determined using Design Expert 6 software package. The results can be seen in Figure 5-33, a 3D representation of the design space. Each side of the cube represents one experimental factor with the corners signifying the minimum and maximum levels. The airborne concentration obtained from each level of each set of the three factors is designated by the number at each corner inside the cube. From these results, the best results can be seen using liquid CO₂, 5 weight % silica, and using surface modification. Based on the data, a model described by Equation 5-1 was developed by the software.

$$\begin{aligned} \text{Airborne Concentration} = & 73.55 + 0.70A (\text{Medium}) - 1.80B(\text{Surface Modification}) \\ & + 3.95C (\text{Spacer}) + 6.80AC + 1.80BC \end{aligned} \quad (5-1)$$

In Equation 5-1, the factors that have a significant effect on airborne concentration are shown along with the magnitude of their effect by the factor coefficient. The standard deviation for the coefficients was ± 0.6 . Half the coefficient value is the factor effect. It is seen that the spacer and the interaction between the spacer and the medium have the largest effect on dispersion. Using this model, a maximum airborne concentration can be calculated based on different levels of these parameters. Within this design space, a maximum airborne concentration of 85% is predicted and experimentally obtained.

Up to this point experiments have been performed to investigate the effect of important parameters on the particle size and airborne concentration. The effect of chosen parameters on interparticle forces has been calculated and compared to the experimental results. In order to obtain a better understanding of the effect of these factors on the interparticle forces measurements of the macro and micro scale must be performed. To do so, bulk properties were studied using the shear cell and interparticle force measurements using the atomic force microscope. A comparison of the change in magnitude of the interparticle forces as they relate to these factors results in a correlation between the significant interparticle forces and their relationship to dispersion is discussed in the next section.

Interparticle Forces on the Macro and Micro Scale

In order to develop the knowledge base about dispersion that will apply, in general, to many different powder systems, an understanding of the changes in a powder system that occur following processing is required. The above research investigated important factors of dispersion, from which an expression of their effect on dispersion was developed. Now, the interparticle forces on both the macro-scale, the forces of powder as a continuum, and on the micro-scale, forces between individual particles, will be investigated. From this work,

knowledge of the change in interparticle forces will be developed. The correlation of the results of these two aspects will lead to an understanding of why processing parameters have an effect on dispersion, from which an extension to other powder systems will be possible.

Bulk Powder Strength

Most aerosol applications begin with the powder being drawn from a reservoir in the bulk state before forming the aerosol. Knowledge of powder as a continuum, specifically macro-scale powder properties such as strength and flow, is therefore important to optimizing dispersion. In order to better understand the cohesive behavior of powder due to the effect of capillary forces, a monodispersed spherical aluminum powder was tested in a bulk powder shear tester, the Sci-Tec ShearScan, with and without hydrophobic surface modification at varying relative humidity values.

Experimental methods

The aluminum powder was divided into three samples. Two of the powder samples were modified by ODTMS and TDFS using the parameters determined previously, after which both powder samples were supercritical dried. The third sample was left in the as received state with a minimal native aluminum oxide surface. The powder was conditioned for 48 hours at a constant relative humidity after which the powder strength was measured using the shear tester.

Preconditioning of aluminum powders for shear testing was performed inside a humidifying chamber. Samples were placed into the chamber and humid air was pumped through the chamber for 48 hours prior to measurements to allow the powders time to equilibrate. Humidity was controlled by pumping dry, compressed air through a water trap and by controlling the temperature of the water. Humidity levels were controlled to within $\pm 2\%$.

Approximately 30 cm^3 of conditioned powder was loaded into the annular shear cell inside the humidity chamber and then mounted on the shear tester. Samples were sheared under normal

consolidation loads of 2.5, 5, 10, 20 and 30 kPa. The linear rotational speed of the shearing lid was maintained at 5 mm/min. Outlying data points, greater than one standard deviation, were removed from the yield locus and the unconfined yield strength and maximum principal stress recorded and plotted as a powder flow function.

Shear test results

The results for unconfined yield strength, f_c , versus maximum principal stress, σ_1 , at the different relative humidity levels have been plotted in Figure 5-34, Figure 5-35, and Figure 5-36. In each graph the bare aluminum is represented by squares, the ODTMS modified aluminum is represented by circles, and that of TDFS by triangles. Measurement points are designated by the markers. Figure 5-34 shows the results for f_c after conditioning at 20 percent relative humidity. At this condition, all three powders have the same unconfined yield strength, a maximum f_c of 12kPa at the highest normal load of 30kPa. The cohesion in this case is dominated only by van der Waals attractive forces and frictional forces between the powder particles. Figure 5-35 shows the powder flow function measured for the aluminum powders treated at 50 percent humidity. It can be seen there that the strength of the bare aluminum increased at the higher consolidation loads, 37%, to a maximum of 18kPa, while the surface modified aluminum powders, which each had the same strength, increased 20% to a maximum of 15kPa. The results of f_c vs. σ_1 for the three powders at 80 percent humidity are seen in Figure 5-36. The powder strength of the bare aluminum again increases an additional 25 percent to 26kPa while no significant increase in the strength was seen for the surface modified powders.

In order to better understand the effect of relative humidity on each of the powders themselves, the unconfined yield strength, f_c , versus major consolidation stress, σ_1 , for each powder at the three relative humidity levels were compared. The shear testing results on bare aluminum powder is shown in Figure 5-37. The powder strength at the three measured humidity

levels is within experimental error at principal stresses below about 20kPa. Principal stresses above 20 kPa show differences in powder behavior with respect to relative humidity. There is a 40 percent increase in strength which is a result of increasing the relative humidity from 20 percent to 50 percent humidity. An additional 25 percent increase is observed as the relative humidity was increased to 80 percent. Hence it is shown that the powder strength is directly affected by relative humidity. The mechanism for the increase in particle strength is the formation of pendular liquid bonds between particles that cause capillary forces adhering particles together. As a result of the increase in interparticle forces, a corresponding increase in cohesion is seen.

Shear test discussion

The results for the aluminum powder modified with TDFS are seen in Figure 5-38. There is a 25% increase in strength as humidity is increased from 20 to 50 percent; however the subsequent increase in relative humidity does not result in a significant increase of strength. The initial increase is significantly lower than that observed for the bare aluminum samples hence the hydrophobic coating has decreased the powder strength due to less adsorbed moisture and therefore less capillary forces acting on the particles.

Similar conclusions were drawn for the ODTMS modified aluminum powder results seen in Figure 5-39. As humidity is increased there is a trend towards slightly higher bulk strength, however the increase is not significant when compared to the experimental error of 10% for these measurements. This indicates that humidity did not significantly change the unconfined yield strength of this material and the capillary forces were controlled.

Comparing the powder flow functions of bare aluminum, Figure 5-40, to that of the TDFS and ODTMS surface modified aluminum, Figure 5-41 and Figure 5-42 respectively, it is seen that at 20% relative humidity, the modified and unmodified powders have very similar behavior.

When the relative humidity is increased to 50% the unconfined yield strength for modified and unmodified aluminum, 19 kPa and 14.5 kPa respectively, begins to deviate. A similar difference is seen for measurements at 80% relative humidity where the unconfined yield stress for the bare aluminum increases while there is not significant change in the surface modified powders.

These results indicate that the hydrophobic surface coatings directly influenced the mechanical strength measured on bulk powders by reducing adsorbed moisture on the surface of the particles. From the data presented above, it can be seen that the use of surface modification can be successfully used to maintain the unconfined yield strength of a spherical aluminum powder in an environment of high relative humidity. The powder modified with ODTMS showed no significant change in strength under any conditions. Even at the high relative humidity levels a significant amount of water did not adsorb onto the hydrophobic surface. The powder modified with TDFS showed a slight increase in strength from 20 to 50 percent relative humidity but no further change in strength from 50 to 80 percent relative humidity. This implies that the powder is not completely hydrophobic, yet humidity can still affect the bulk strength. This could be due to incomplete modification of the surface or because of the powder morphology, roughness, or particle size distribution.

After adding these results into the Design Expert software, a model is fit to the data. From the model, a contour plot of the results within the design space can be made. The plot for the results of the shear tests are shown in Figure 5-43. From the plot it is seen that surface modification reduces the adhesion force at higher humidity levels, which verifies the results described for the shear cell above.

Interparticle Forces

The adhesion force measurements are now taken one step further from the macro-scale down to the micro-scale to investigate the magnitude of the change in interparticle forces as a

function of surface modification and relative humidity. This set of experiments involved the measurement of particle adhesion force and followed the methods described by Ducker [111] and Rabinovich [112].

Experimental methods

The first attempt to measure interparticle forces was by using silicon cantilevers that were coated with aluminum by chemical vapor deposition (CVD). The cantilevers themselves were then surface modified such that each combination of tip and surface could be investigated. Using the CVD process, however, the tip diameters could not be controlled, so that the force measurements would be difficult to interpret. In addition, after inspection of the tips after the first set of measurements using the transmission electron microscope, it was found that the aluminum coating was soft and easily damaged during the experiments. The force exerted on the tip during the measurements was enough to actually remove the aluminum coating and expose the underlying silicon nitride tip. This can be seen in Figure 5-44, a TEM image of one such cantilever tip. Therefore, for remainder of the measurements, particle probes were employed.

Each particle probe was made by mounting either a modified or bare Valimet aluminum particle, as used for the shear tests, to a tipless silicon cantilever employing a standard quick set epoxy. Figure 5-45 shows an SEM image of a bare aluminum particle mounted to the cantilever and Figure 5-46 shows the same for an ODTMS surface modified aluminum sphere. These particles, however, are near the same size as the flakes. During force measurement there was a good chance they would lift the flakes off the substrate and hinder force measurement.

Therefore, the CVD aluminum surfaces made during the surface modification experiments were used. Contact mode topographical images of the bare aluminum surface can be seen in Figure 5-47 through Figure 6-15. Images of the ODTMS surface made through the same method can be seen in Figure 5-48 and Figure 5-49. Using the AFM, the root mean squared (rms) surface

roughness for the bare aluminum and ODTMS modified aluminum was measured to be 1.6nm and 1.8nm respectively.

For each force measurement, the sphere attached to a cantilever of known spring constant, was positioned close to the flat substrate. Then, as the substrate and particle were moved towards and away from each other by a piezoelectric, the deflection of the cantilever as it interacted with the surface was monitored by a laser that reflects off the top of the cantilever onto a position sensitive photodiode. In this manner, the force between the two surfaces as a function of separation distance was obtained. The force-distance data presented can be normalized by dividing the measured force by the radius of the sphere. The result is energy per unit surface area and thereby allows a straightforward comparison of the sphere-surface interaction forces to different geometries such as flakes.

A typical force-distance plot is given in Figure 5-50. As the particle and surface approach each other, the onset of interaction is shown by the jump-to-surface point. Once the particle is in contact with the surface, the cantilever bends slightly as seen by the upward slope of the line. After a maximum deflection equal to 5nN, the software triggers the piezoelectric to change direction and the particle and surface move apart. During retraction, the point of particle release is seen by the jump-off-surface point. From the deflection distance and cantilever spring constant the force of interaction is calculated.

The environment around the sample was controlled through the use of a humidity chamber, also by Asylum Research, which has a sensor to monitor the internal temperature and relative humidity. The standard room humidity varied between 45 and 50% as measured by the device. The humidity was decreased below this point by flowing dry compressed nitrogen at a controlled rate through the chamber. To raise the humidity, the nitrogen was first bubbled through water

then to the chamber. By this method, the humidity could easily be controlled between 5% and 85% and within $\pm 0.5\%$ relative humidity of the target value. The change in interparticle forces over a range of humidity levels from 10% to 80% were measured for modified and bare aluminum.

Interparticle force results and discussion

For the bare aluminum particle and bare aluminum surface, the measured forces over changing humidity are seen in Figure 5-51. In a dry state, between 10% and 20% relative humidity, the interparticle forces are seen to be $835 \pm 60 \text{ nN}$ and $800 \pm 60 \text{ nN}$ respectively. This value can then be compared to that calculated using the general van der Waals equation for the force of interaction between a smooth sphere and plate from Table 3-1, which yields a force of interaction of 888 nN . It should be noted that the contact angle was measured on the CVD aluminum surface with 1.6 nm rms surface roughness. Taking into account that the real material has surface roughness and other imperfections that will lower the adhesion force as discussed in Chapter 3, the values are favorably comparable.

After 20% relative humidity, the critical humidity is reached. It is at this point that enough water is adsorbed onto the surfaces that a meniscus forms between them and the onset of capillary forces between the surface and particle can be seen. To verify the data, the capillary forces can be calculated using Equation 3-10, the average particle size of $5 \mu\text{m}$, and the receding contact angle of 7.8° measured on the CVD aluminum surface. The result is an interaction force of 1800 nN which again is extremely close to the measured value of 1920 nN at 30% relative humidity for the onset of capillary forces. Here, again, the difference can be attributed to the variation between the real and ideal surface. The volume of water in the meniscus increases due

to the increase relative humidity from 20% to 40% relative humidity and accordingly so does the capillary force.

These results are in agreement with the work completed by Rabinovich et al.[55, 91] that there is a critical humidity to the onset of capillary forces and this value is proportional to roughness. Below this critical point there is no change in interparticle forces, which are dominated by van der Waals attraction. At the critical humidity, enough water is adsorbed onto the surface that a meniscus can form and along with it capillary forces. The forces will increase with the volume of the meniscus. Measurements above 40% relative humidity were not possible because the capillary forces exceeded the spring constant of the cantilever. Upon retraction, excess cantilever deflection leads to saturation of the photodiode and an incomplete force measurement. Despite this complication, the range of the van der Waals forces, the critical humidity required for the formation of a meniscus, and capillary forces have been calculated and verified by the AFM measurements.

Next, the effect of surface modification on interparticle forces was investigated. Since both silane coupling agents showed similar results, only ODTMS was used for the experiments. The results can be seen in Figure 5-52, a plot of adhesion force between an ODTMS modified particle and ODTMS modified surface. At low relative humidity, the adhesion force is significantly lower than that seen for the bare aluminum surfaces in Figure 5-53, 14nN for ODTMS as opposed to 800nN for the bare aluminum despite a similar particle size. The surface energy of the silane modified material is much lower than that of the bare aluminum as seen by the contact angle measurements made previously. Bare aluminum had an advancing water contact angle of 67° whereas the ODTMS modified surface has an advancing contact angle of 114° . These values were used to calculate a work of adhesion, W_A , of 101 J/m^2 for the bare

aluminum surface versus 43 J/m^2 of the modified surface. A decrease in the work of adhesion means less energy is needed to separate the materials and indicates a change in the interparticle forces.

This can be due to two different reasons. First, the ODTMS has a lower work of adhesion and therefore will decrease the value of the effective Hamaker constant below that of bare aluminum and in turn lead to a decrease in interparticle forces. A second effect of the coating is creating an increased separation distance between the aluminum particles themselves, and using the new, increased separation distance in the van der Waals equation from Table 3-1, a value of 24 nN is calculated. This value is quite comparable to the measured value of 15 nN using the AFM. From this it can be concluded that it is both of these effects of surface modification that contribute to the decrease in interparticle forces.

Upon increasing the relative humidity, an increase in adhesion force is seen. This trend is also comparable to that observed in the contact angle and shear cell measurements made previously. The contact angle measurements show that the ODTMS does not create a completely hydrophobic coating and a slight increase in bulk strength was seen in the bulk measurements. To check the validity of these values, Equation 3-10 can again be employed. Using the receding contact angle reported above of 68.5° and the average particle size of $5 \mu\text{m}$, an interparticle force of 415 nN is calculated. This value is in agreement with the onset of capillary forces measured here to be 460 nN at 40% relative humidity. The maximum increase in adhesion force for ODTMS of 770 nN at 80% relative humidity is less than the observed value for the bare aluminum or 3700 nN at the same relative humidity. This demonstrates that the surface modification changes the material hydrophobicity as well as control interparticle forces in the presence of humidity.

By dividing by the radius of the particle, the interaction energy per unit area can be calculated. This was done and reported in the graph in Figure 5-54, a plot of the interaction force divided by particle radius versus relative humidity. From this information, the energy of interaction of surfaces of different sized can be compared. This data can now be used to show that even for flakes, surface modification will reduce the van der Waals forces and improve dispersion.

Again the data was added into Design Expert and the ensuing contour plot developed also confirms these results. As seen in Figure 5-55, the minimum adhesion force at all relative humidity levels are found when the surface modified materials are used.

Data Correlation

The final step of this research was to take the experimental results for the dispersion experiments and correlate them to the change in magnitude of the interparticle forces. To aid in this, Design Expert 6, a statistical design software package, was used. During the analysis of the results from each set of experiments, contour plots of the results were made. By overlaying these plots the optimum levels of the factors for a set of experiments can be compared to those of the other experiments. Figure 5-56 shows the overlay for the shear cell and AFM results. From here it can be seen that for both the interparticle forces and the bulk forces the optimum conditions, lowest adhesion, require surface modification. This overlay can also be combined with the experimental cube developed above. By aligning the surface modification axis, thereby taking into account the optimum bulk forces and interparticle forces, the optimum results to satisfy all conditions will lie in the upper half of the cube which is shaded in Figure 5-57. The optimum results for airborne concentration, is found in the upper right corner of the design space corresponding to a surface modified powder, with 5 weight percent spacer, using liquid CO₂ dissemination. It was determined, based on the shear cell measurements, that these conditions

will have the lowest bulk strength; based on the AFM to have the lowest interparticle forces; and thus as seen in the airborne concentration, to yield the highest dispersion.

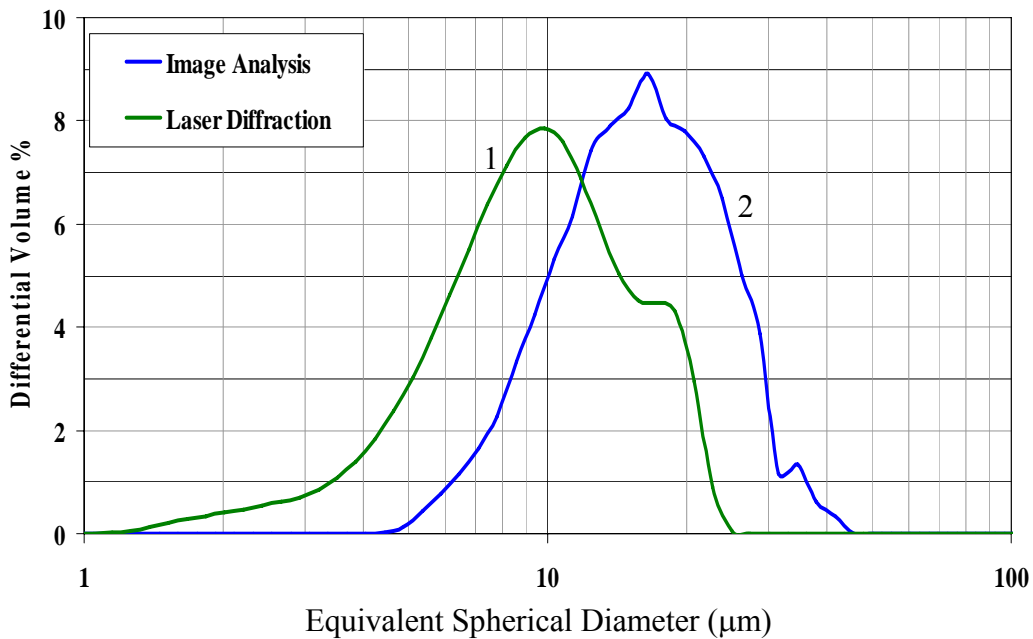


Figure 5-1. Particle size distribution of aluminum flakes. The graph of volume weighted equivalent spherical diameter, particle size, as measured by laser light scattering, shown a mean particle size of 10microns, represented by the curve labeled 1. The volume weighted particle diameter measured by image analysis shows a mean particle size of 17microns and is represented by curve 2.

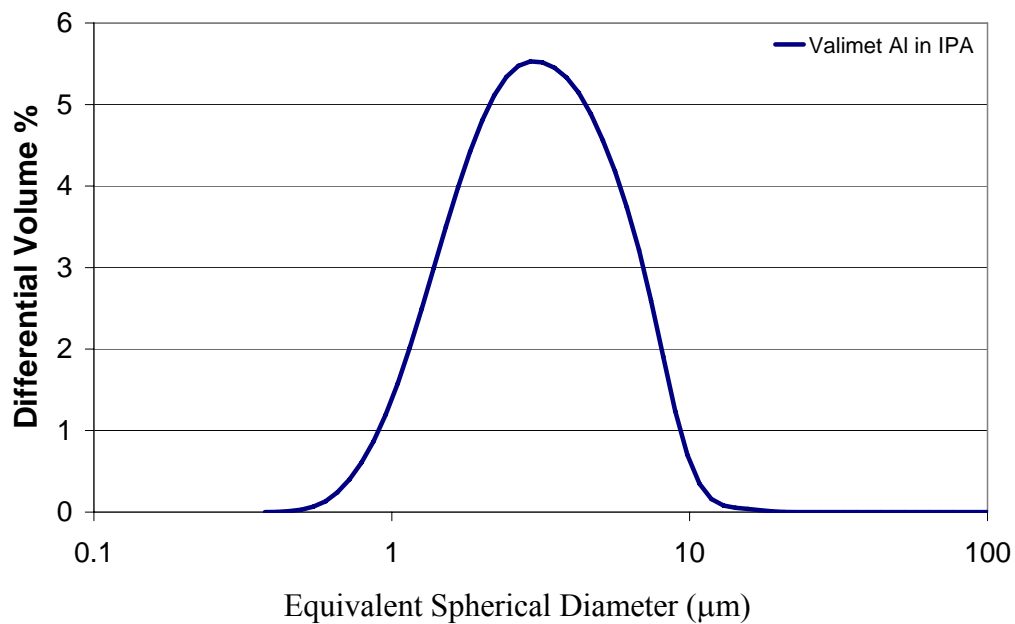


Figure 5-2. Particle size distribution of Valimet aluminum in isopropyl alcohol. The mean particle size is 4 microns.

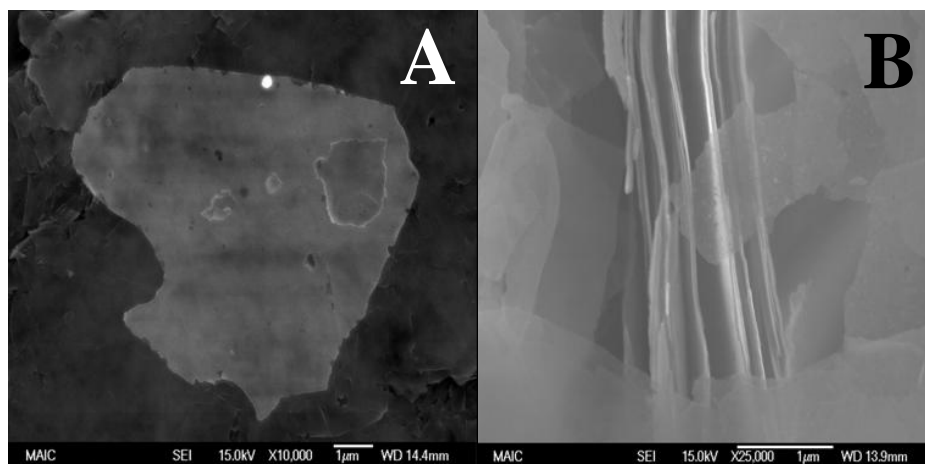


Figure 5-3. SEM images of Sigma VPD Aluminum flakes. A) is an image of the Sigma 1215 flake face. B) shows the edges of a stack of Sigma 1215 flakes. The 15nm flakes are so thin that they are partially transparent to the SEM as seen by the faint flake faces visible in B.

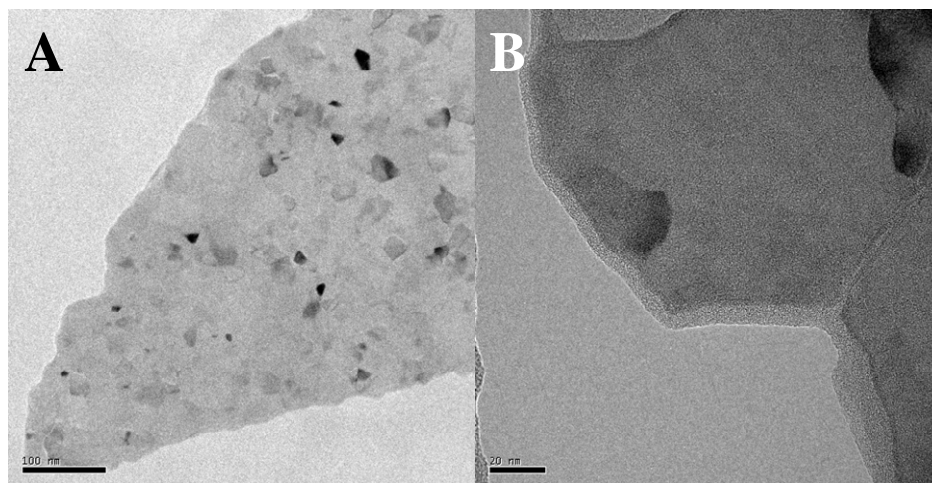


Figure 5-4. TEM images of Sigma 1215 aluminum flakes. Transmission electron microscope images taken by Kerry Siebein at the Major Analytical Instrumentation Center at the University of Florida. A) shows that the aluminum is polycrystalline. In B) the thin oxide layer can be seen.

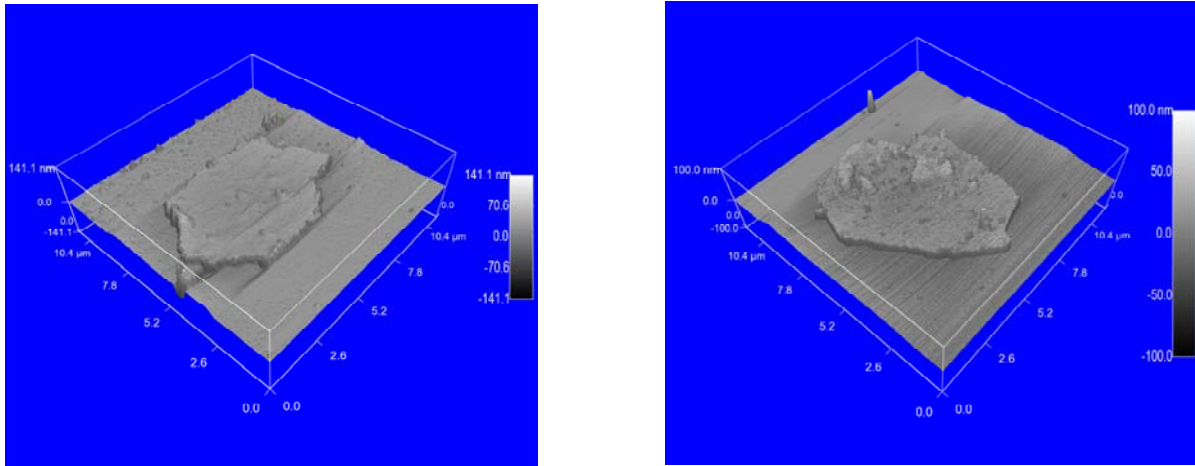


Figure 5-5. Contact mode topographical images of aluminum flakes. The contact mode of the AFM was used to make topographical images of the aluminum flakes deposited on a silicon substrate. The irregular shape of the flakes and infrequent large scale roughness are indicative of the milling process.

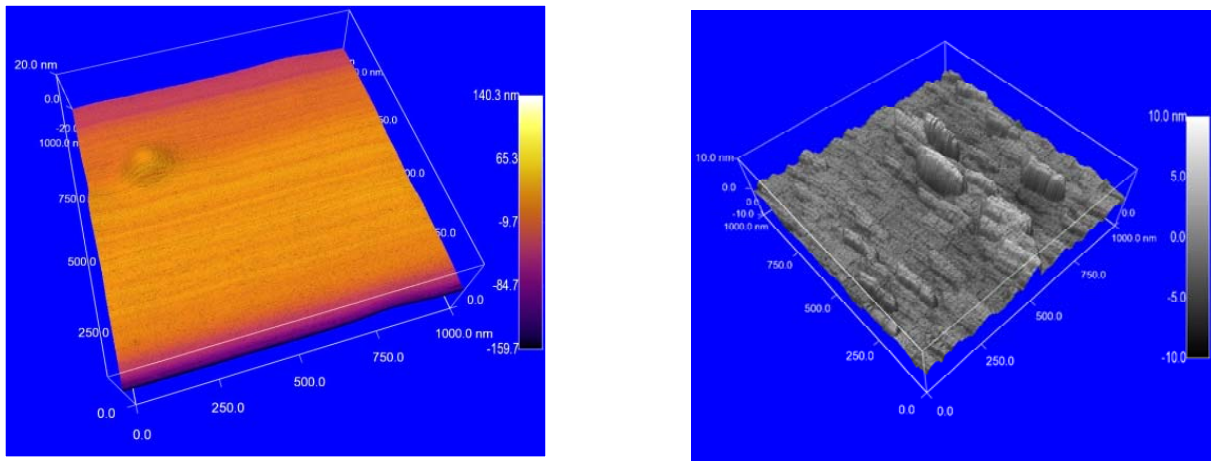


Figure 5-6. Detailed topographical image of flake surface. These contact mode topographical AFM images show the flakes themselves to have a very uniform and smooth surface. The roughness was measured to be 4nm rms.

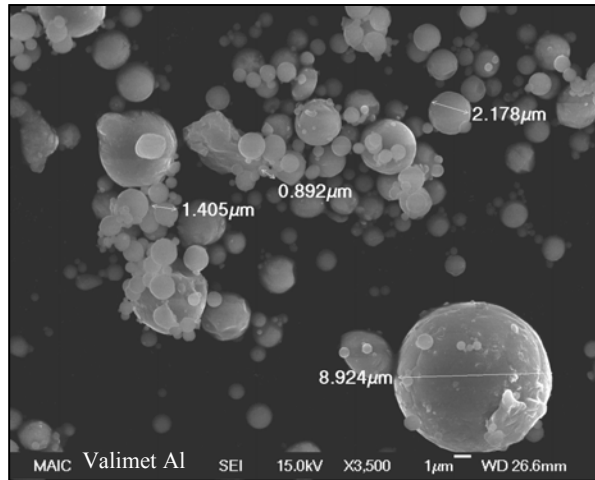


Figure 5-7. SEM Image of Valimet aluminum spheres. Atomization produces a spherical powder; however the particle size distribution is seen to be large.

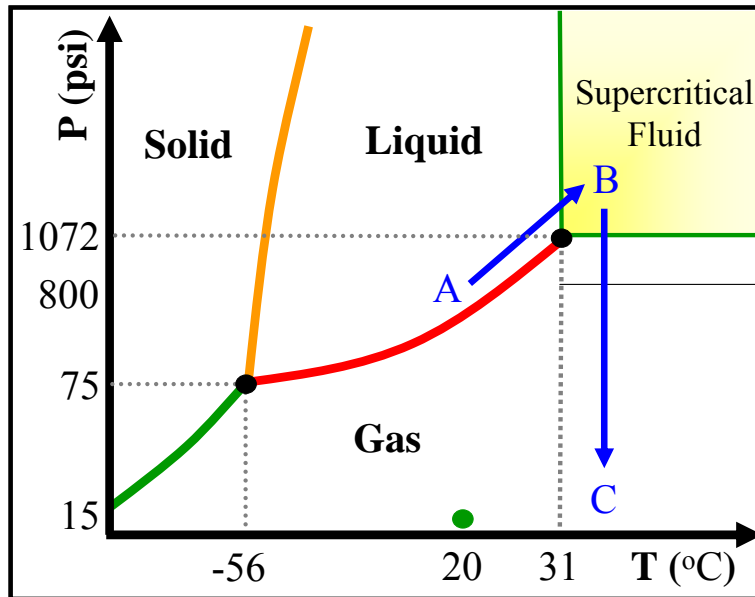


Figure 5-8. Phase diagram for carbon dioxide as related to supercritical drying. The thermodynamic path taken during supercritical drying is depicted by the lettered path. The process starts with CO₂ as a liquid (A). It is heated above the critical point (B) and then released as a gas (C). For comparison, standard room temperature and pressure is represented by the dot.

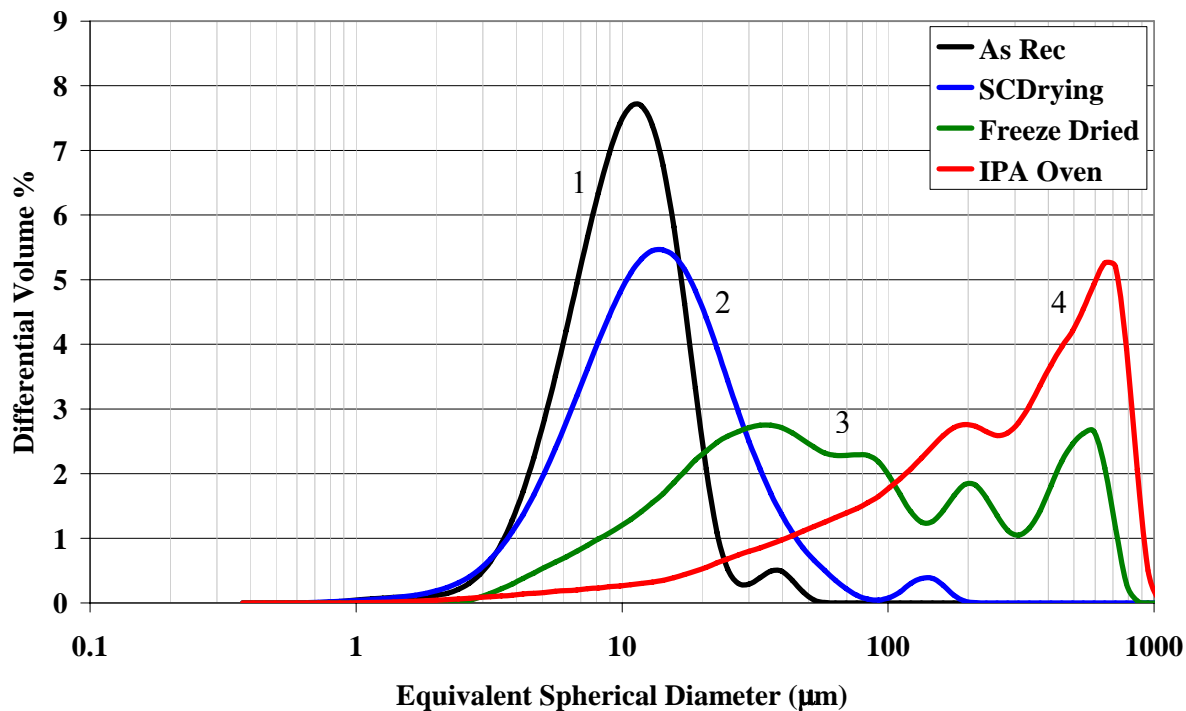


Figure 5-9. Particle size distribution measured following each drying method. The curve labeled 4 shows the results for evaporation, with the largest amount of agglomeration due to capillary forces that pull the particles together as the liquid evaporates. Freeze drying is represented by curve 3 and is the second most agglomerated powder. During freeze drying, capillary forces can also form if the pressure is not sufficiently low and the ice starts to melt before sublimation. Supercritical drying, shown by curve 2, completely avoids the gas-liquid phase boundary consistently producing the best results in the research. The primary particle size distribution of the material is shown for comparison and represented by curve 1.



Figure 5-10. Contact area with increasing roughness. Roughness has a large effect on interparticle forces due to its connection to contact area. As seen in this schematic, as the roughness of the surfaces increase, the contact area between them decrease. van der Waals forces are also decreased because with increasing roughness, the average surface plain of each body moves further away.

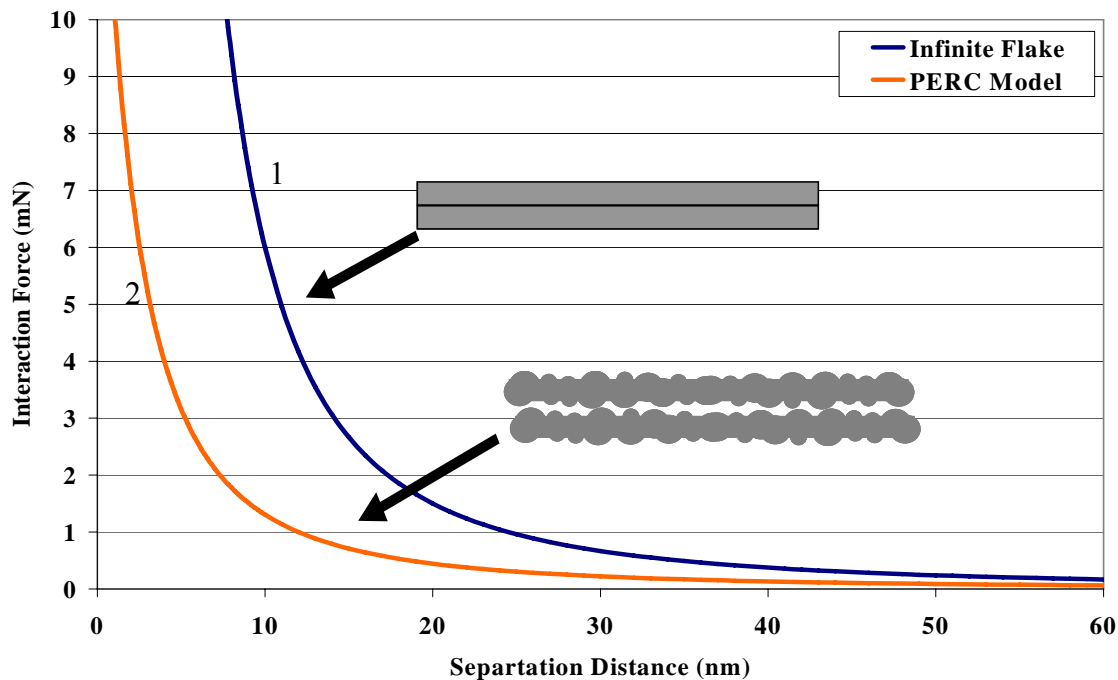


Figure 5-11. Calculated van der Waals forces of a smooth and rough surface. Surface roughness has a large effect on interparticle forces. The line 1 shows the calculation of van der Waals attraction for two smooth surfaces. Line 2 shows the effect of surface roughness incorporated by the PERC model[53, 54] which not only decreases the contact area, but also separates the average surface plane of each body. A significant decrease in the calculated interaction force is seen.



Figure 5-12. Illustration of the change in contact area as a result of the addition of fumed silica. The particle surface cannot be changed to reduce contact area; however, fumed silica can be added to simulate the effect.

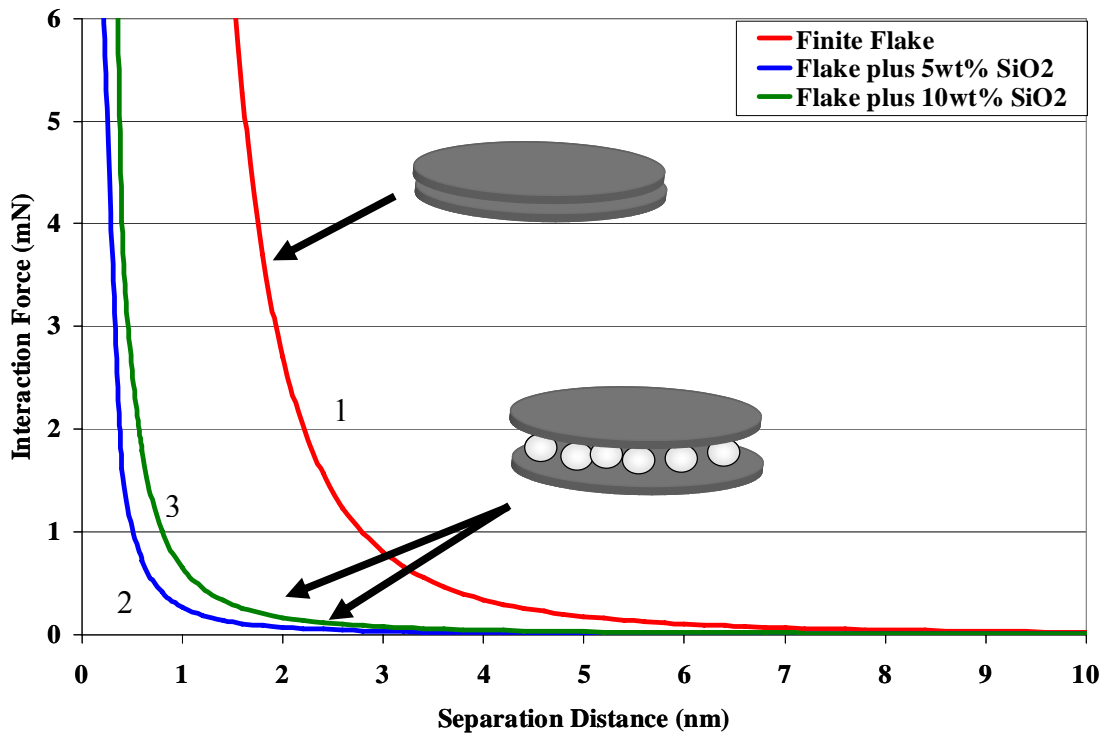


Figure 5-13. Calculated van der Waals forces with the addition of silica. A comparison of the calculated van der Waals forces for two smooth flakes is seen to be much higher than for two smooth flakes separated by silica spacer material. The line 1 shows the calculated van der Waals force for two smooth disks and line 2 shows the calculation for two disks separated by five weight percent added 10nm fumed silica particles. Line 3 shows the calculation when ten weight percent silica is added. The spacer has the same effect as increasing surface roughness, but done without having to alter the flakes themselves. The Hamaker constant of silica is also lower than that of aluminum which also contributes to a decrease in van der Waals forces.



Figure 5-14. SEM images of aluminum flakes with silica. In A) the edge of one flake, shows the smooth surface obtained from Physical Vapor Deposition. B) The aluminum/silica mixture at low silica concentrations. This silica can be seen around each flake. C) The aluminum/silica mixture at high silica concentrations. Note that the distribution of silica between the flakes increasing the interparticle spacing.

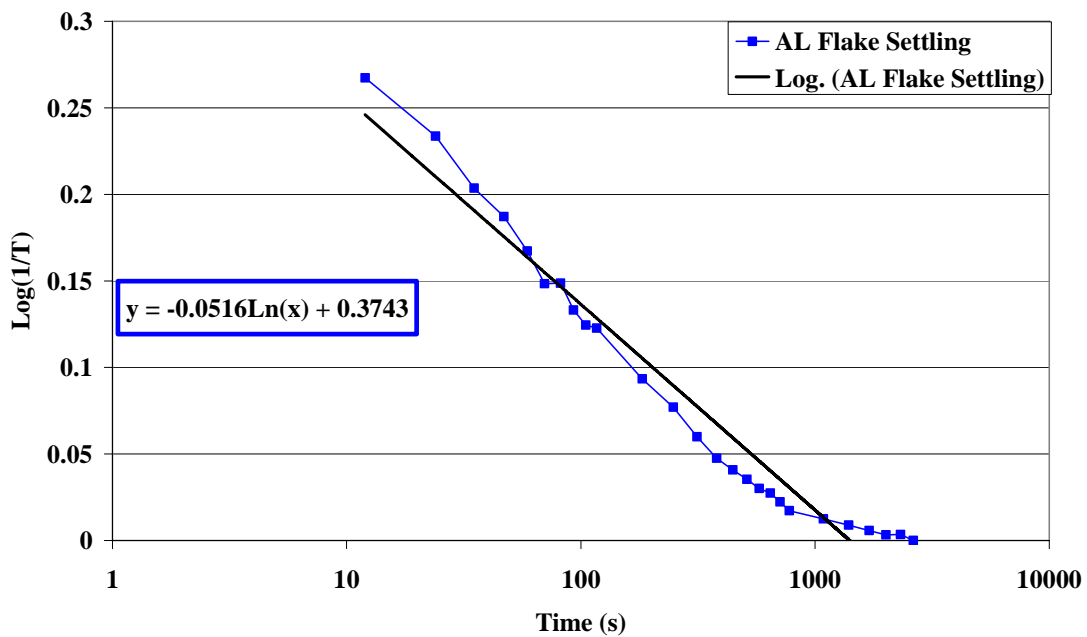


Figure 5-15. Air Chamber transmission measurement. In order to determine the settling rate of the materials, the log of inverse transmission is plotted over time on a log scale for each sample. A trend line is then added.

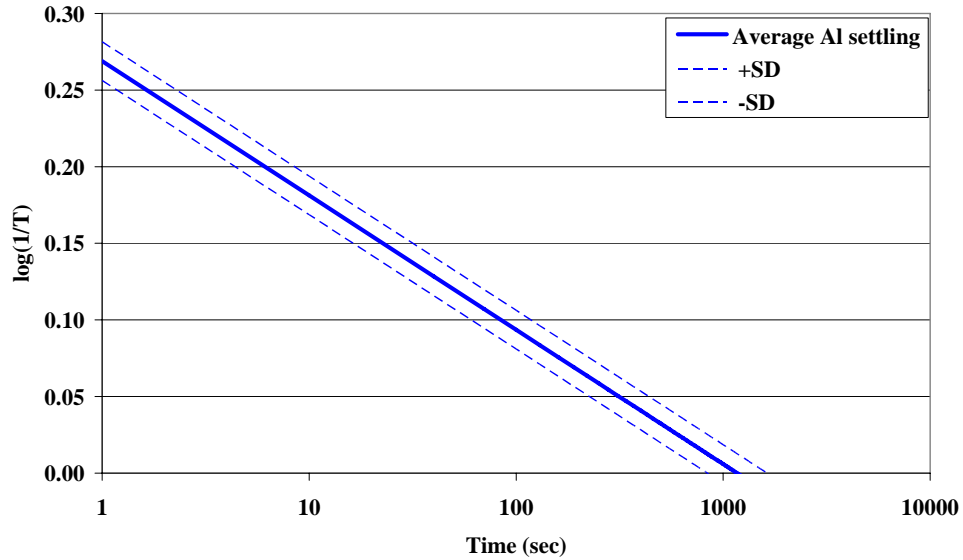


Figure 5-16. Average and standard deviation of settling rate. The trend line equation for each sample is averaged and the standard deviation is calculated in order to determine the statistical significance between factors. From this transmission data and the concentration of powder disseminated, the Beer Lambert Law, Equation 4-1, can be used to calculate the airborne concentration and its change over time.

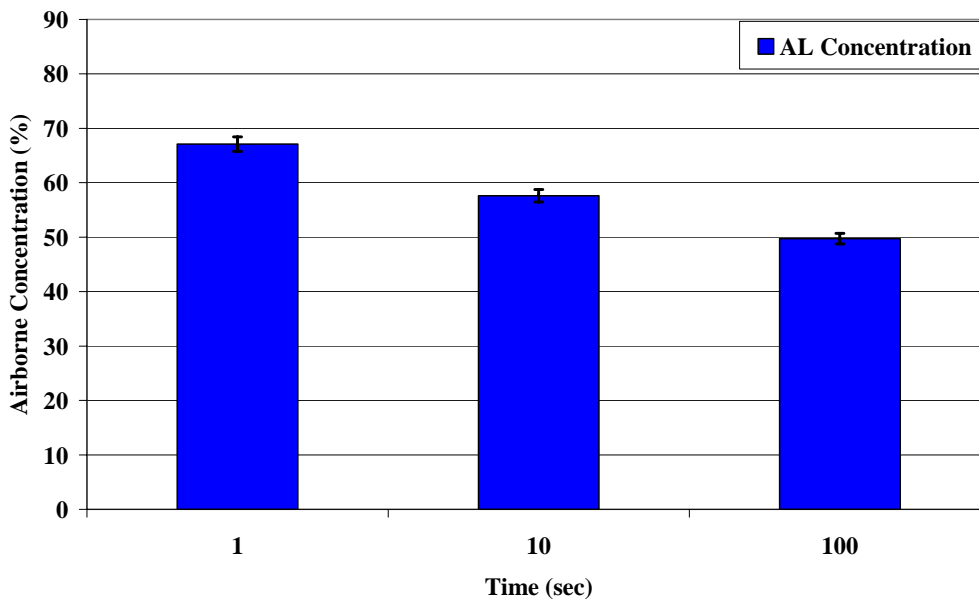


Figure 5-17. Airborne concentration at selected times after partial vacuum dispersion. Using the Beer Lambert Law, Equation 4-1, and the mass of powder disseminated, and the transmission at chosen times, the airborne concentration can be calculated and used to compare factors and their effect on dispersion. Transmission decreases due to an increased number of particles present to scatter the light; therefore, increasing airborne concentration is attributed to increased dispersion.

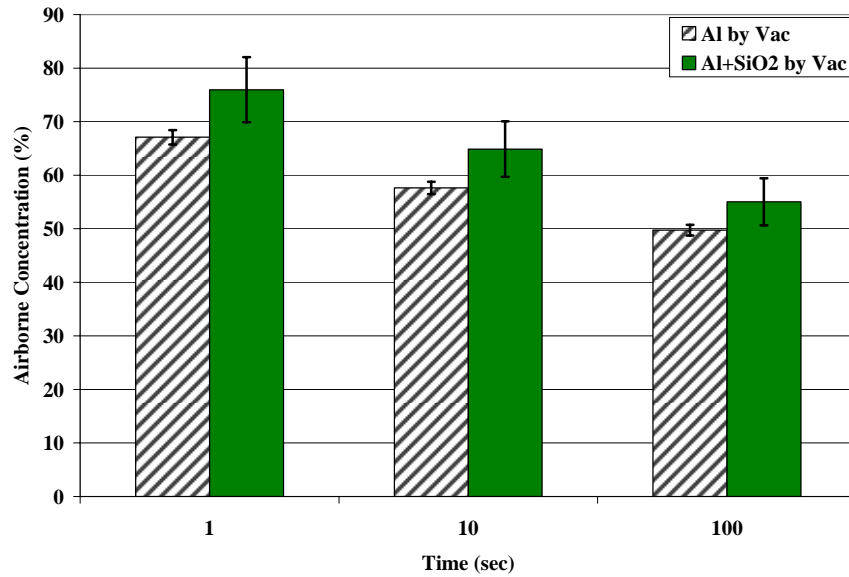


Figure 5-18. Airborne concentration by vacuum dissemination with silica. The addition of 5 weight percent silica to the aluminum is seen to increase dispersion ten percent. This increase is due to the decrease in contact area between flakes resulting in lower adhesion forces.

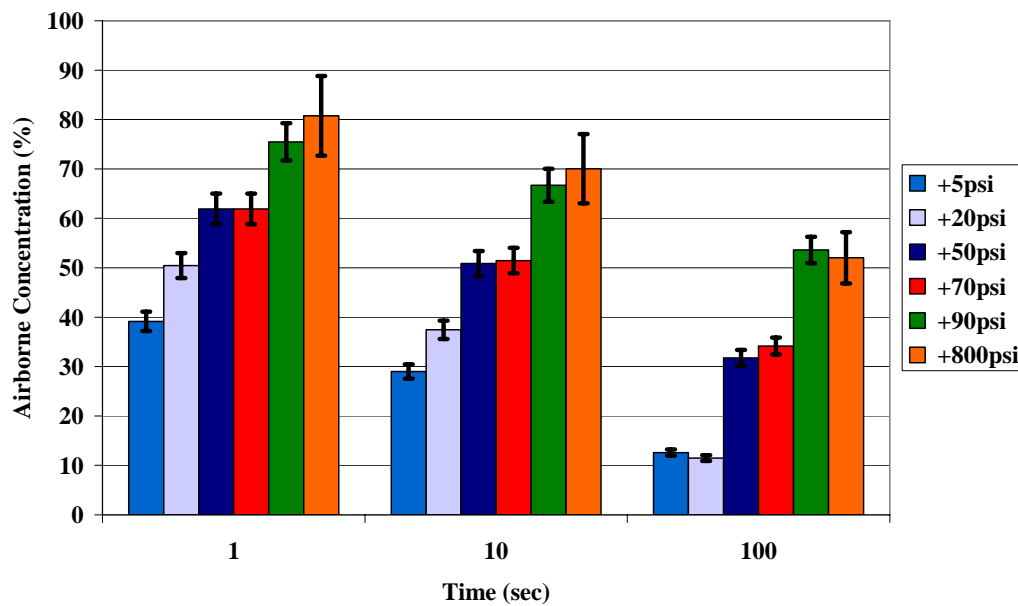


Figure 5-19. Dissemination pressure and airborne concentration. Increasing pressure leads to an increase in airborne concentration because of the larger force applied to the agglomerated and the reduction in the size of the turbulent eddy size.

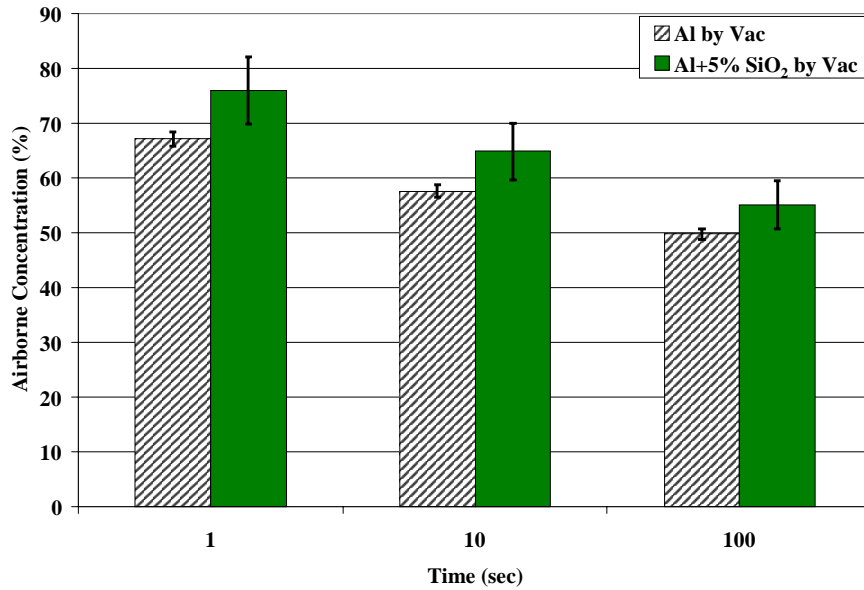


Figure 5-20. Airborne concentration by high pressure gas dissemination with silica. The addition of 5 weight percent silica to the aluminum decreases the airborne concentration when 800psi high pressure gas is used to disseminate the material. This is expected to be due to the inability of the gas to effectively impart enough force on the agglomerates.

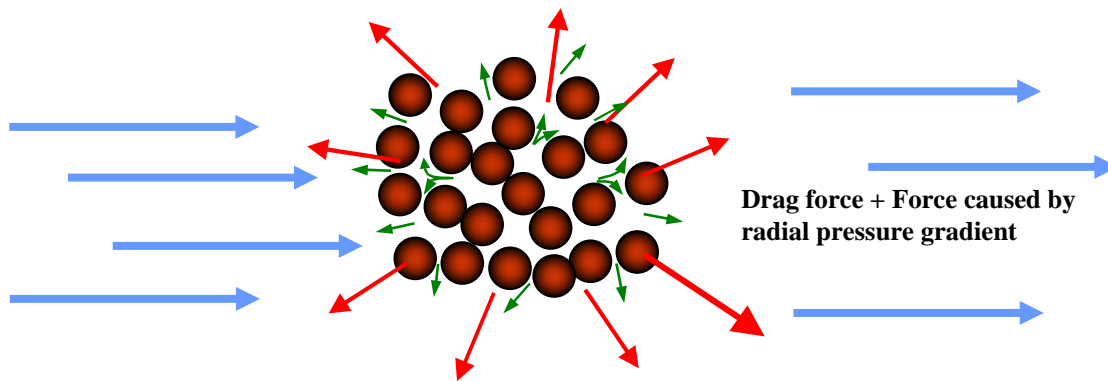


Figure 5-21. Illustration of the dispersion effect of liquid carbon dioxide. Upon release, the liquid carbon dioxide will undergo a phase transformation from a liquid to a gas resulting in an increase in volume of approximately 250 times. The high pressure of liquid carbon dioxide and the radial expansion of the liquid during the phase transformation will increase the amount of force applied to the agglomerate.

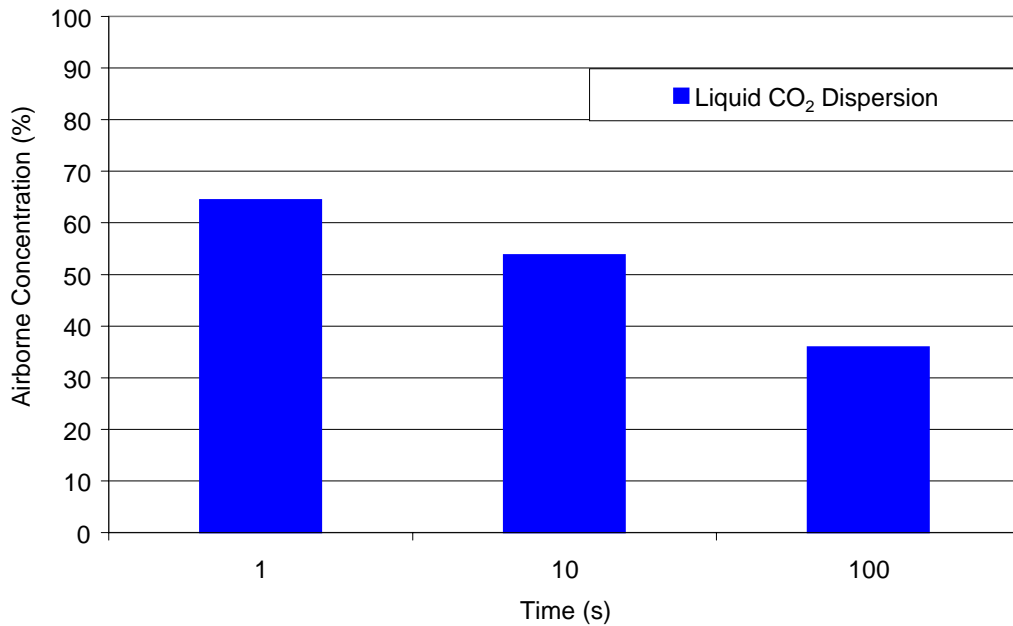


Figure 5-22. Airborne concentration produced by liquid carbon dioxide dissemination.

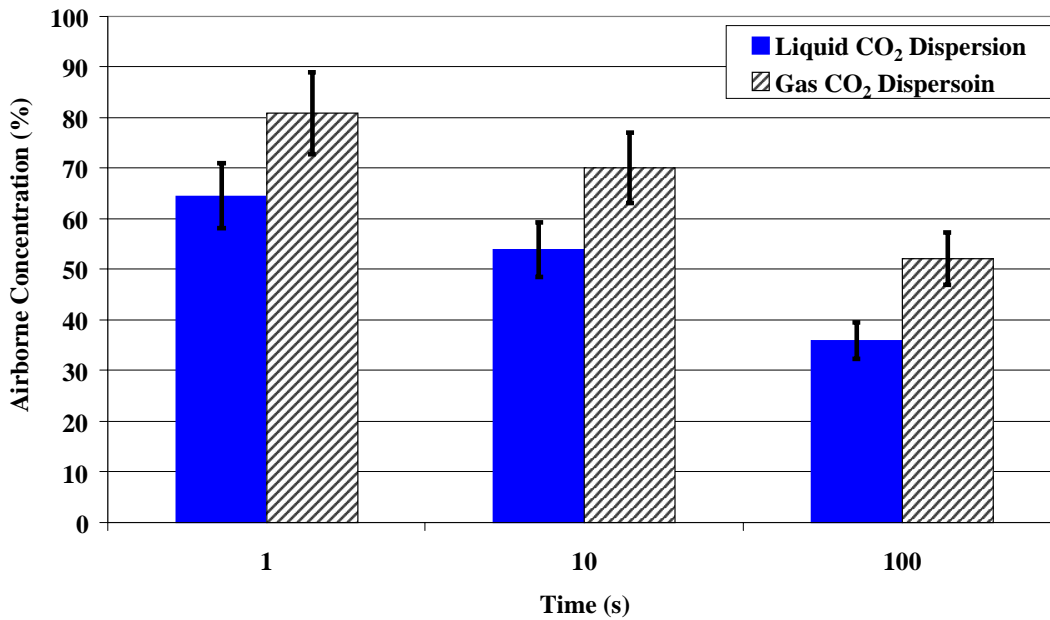


Figure 5-23. Airborne concentration for gas vs. liquid carbon dioxide. Gas CO₂ dispersion is seen to be higher than liquid CO₂ dispersion. This is attributed to the non instantaneous phase change from liquid to gas CO₂ resulting in the formation of capillary forces between the flakes.

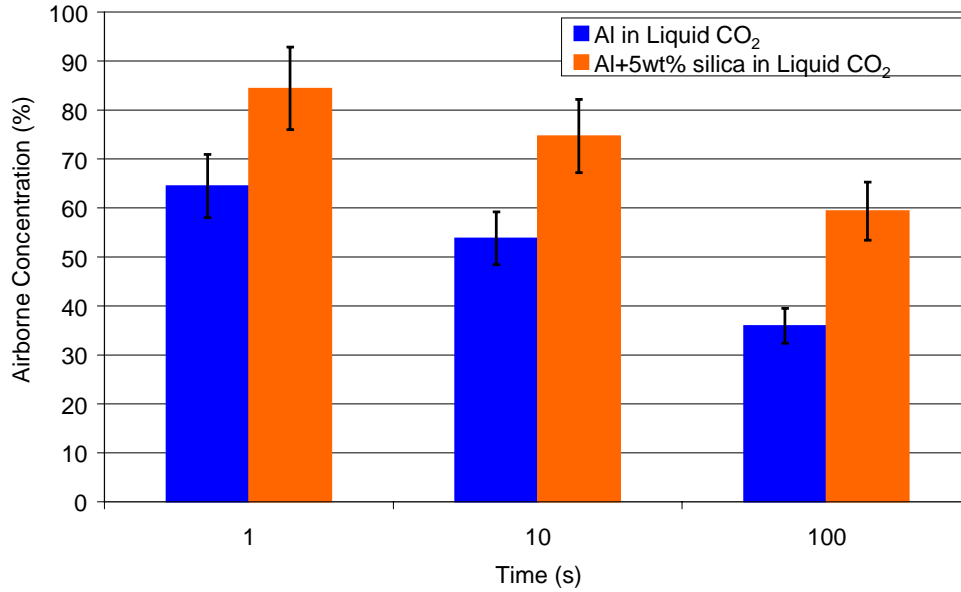


Figure 5-24. Airborne concentration using liquid carbon dioxide and silica. The addition of five weight percent silica has previously been shown to reduce the van der Waals forces between flakes by increasing the interparticle spacing. This also increases the volume of liquid carbon dioxide between the flakes and in turn the amount of pressure that can be generated upon dissemination.

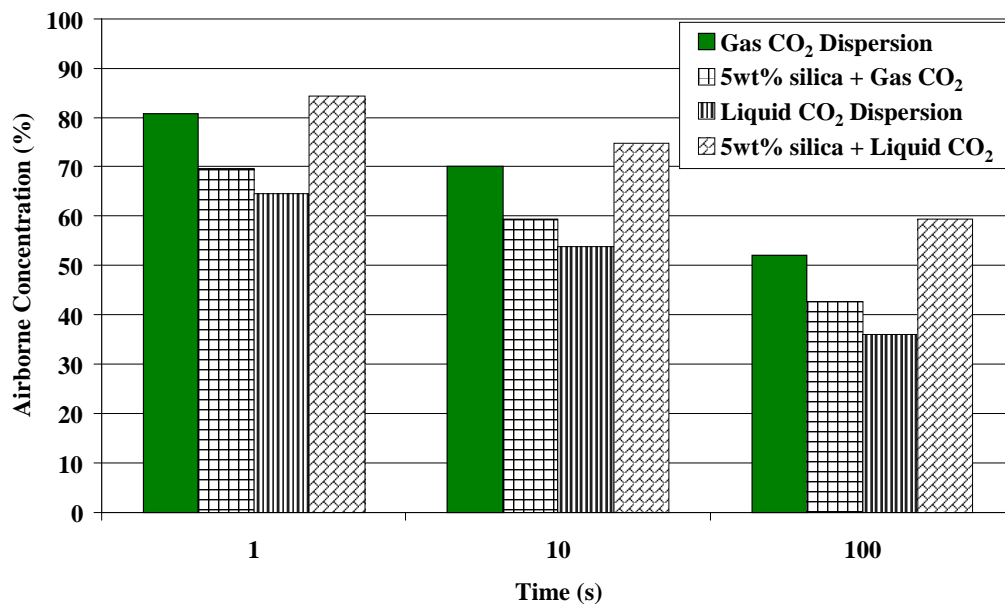


Figure 5-25. Summary of airborne concentration by carbon dioxide dispersion. The graph shows the airborne concentration produced by liquid and gas CO₂ and the addition of five weight percent silica added as a spacer. Liquid CO₂ with the five weight percent spacer yields the highest airborne concentration of eight five percent and thus the best dispersion.

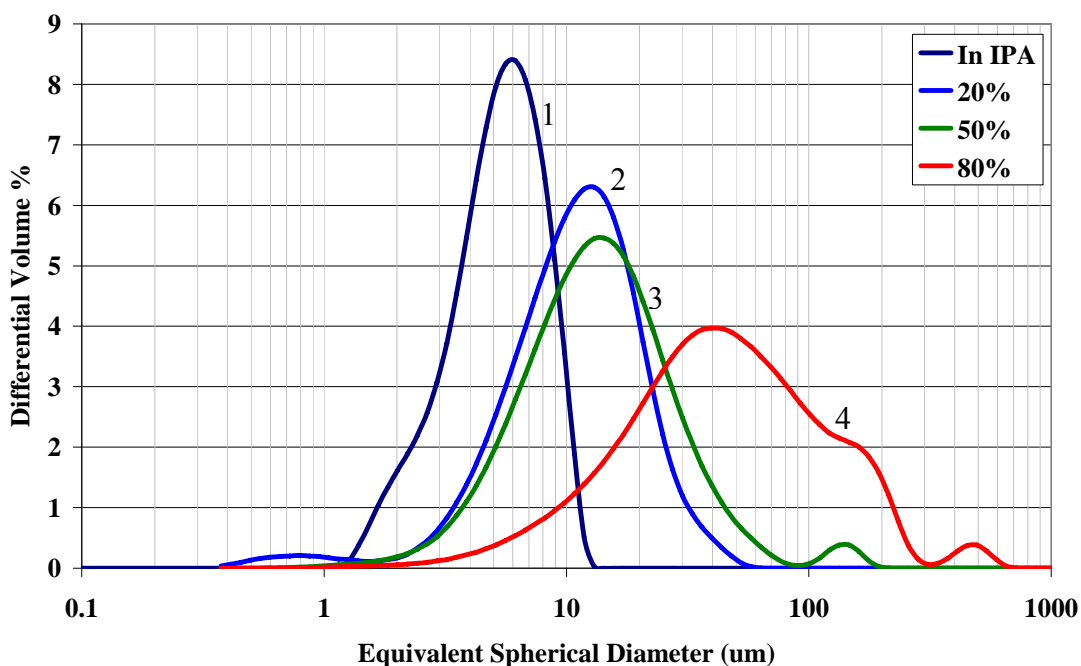


Figure 5-26. Particle size of aluminum flakes at 20, 50, and 80% relative humidity. The graph represents change in particle size of the aluminum flakes after supercritical drying and conditioning for 48 hours at 20% relative humidity, line 2, 50% relative humidity, line 3, and 80% relative humidity, line 4. Line 1 represents the primary particle size measured in isopropyl alcohol and provided as a comparison. The standard deviation for the measurement is $\pm 3\mu\text{m}$. The change in particle size and distribution due to changes in the relative humidity can readily be seen.

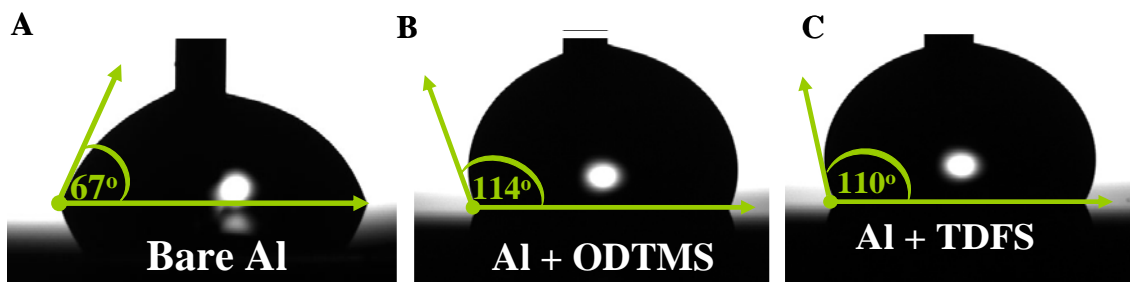


Figure 5-27. Digital image of water drops on aluminum as used for measurement. Contact angle was measured by taking digital images of water drops on the surfaces at varying reaction times. A) A water drop on a bare aluminum surface at time equal to zero with a contact angle of 67° . B) A water drop on an aluminum surface modified by ODTMS for 1hr and C) A water drop on an aluminum surface modified by TDFS for 1 hr.

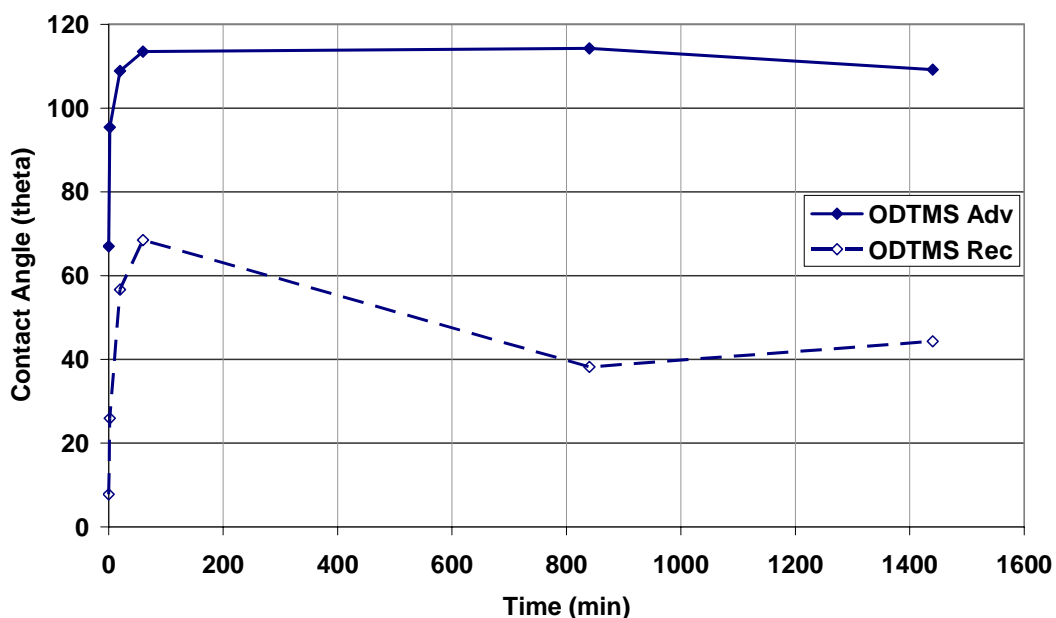


Figure 5-28. Contact angle on ODTMS surface modified aluminum. The change in the contact angle of water on an aluminum surface modified with *n*-octadecyltrimethoxysilane (ODTMS) after varying reaction time. Based on these results, one hour was chosen as the optimum reaction time.

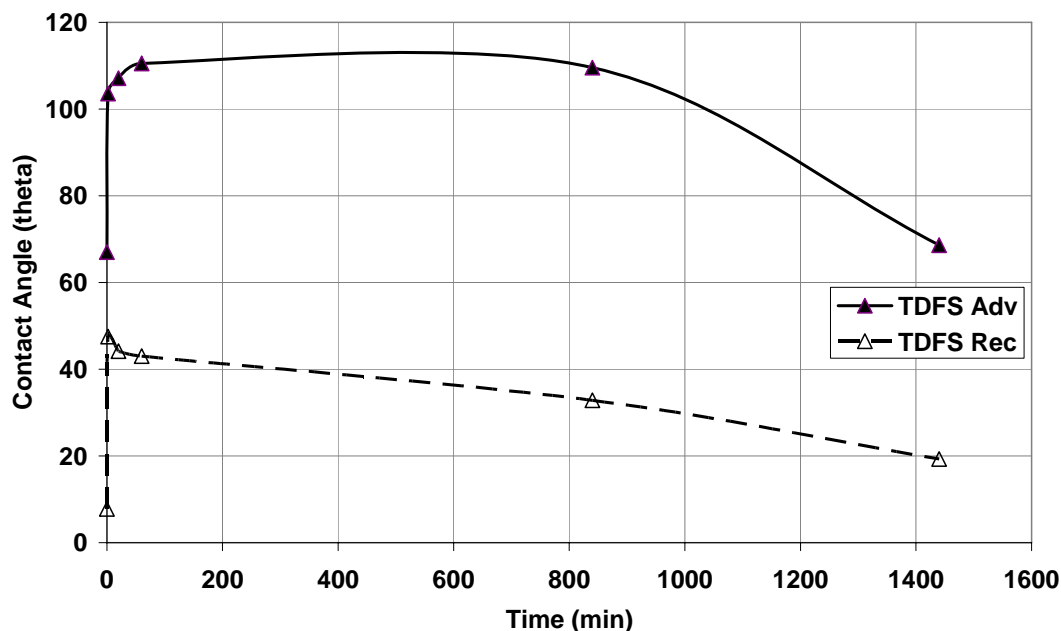


Figure 5-29. Change in contact angle of TDFS surface modified aluminum. The change in the contact angle of water on an aluminum surface modified tridecafluoro-1,1,2,2-tetrahydrooctyl-1-triethoxysilane (TDFS) with varying reaction time. Based on these results, one hour was chosen as the optimum reaction time.

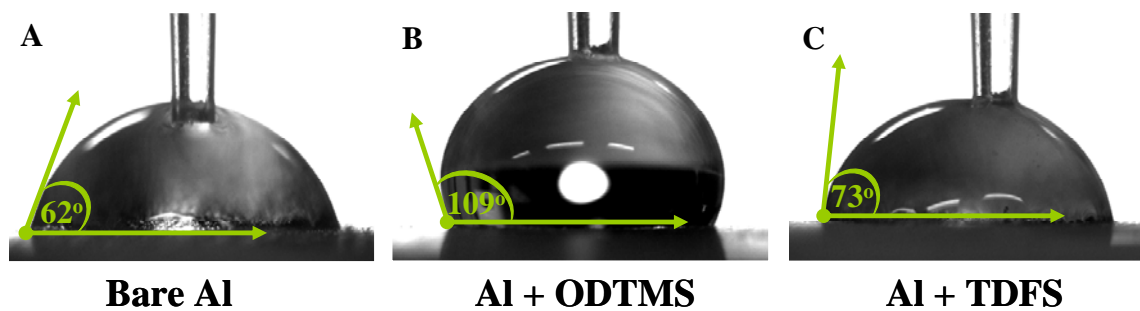


Figure 5-30. Digital image of water drop on modified flake bed. Contact angle was measured on the surface modified aluminum flakes by taking digital images of water drops on packed bed of flakes at varying reaction times. A) A water drop on a bed of bare aluminum flakes with a contact angle of 62° . B) A water drop on an bed of aluminum flakes modified by ODTMS for 1hr with a contact angle of 109° and C) A water drop on an aluminum surface modified by TDFS for 1 hr with a contact angle of 73° .

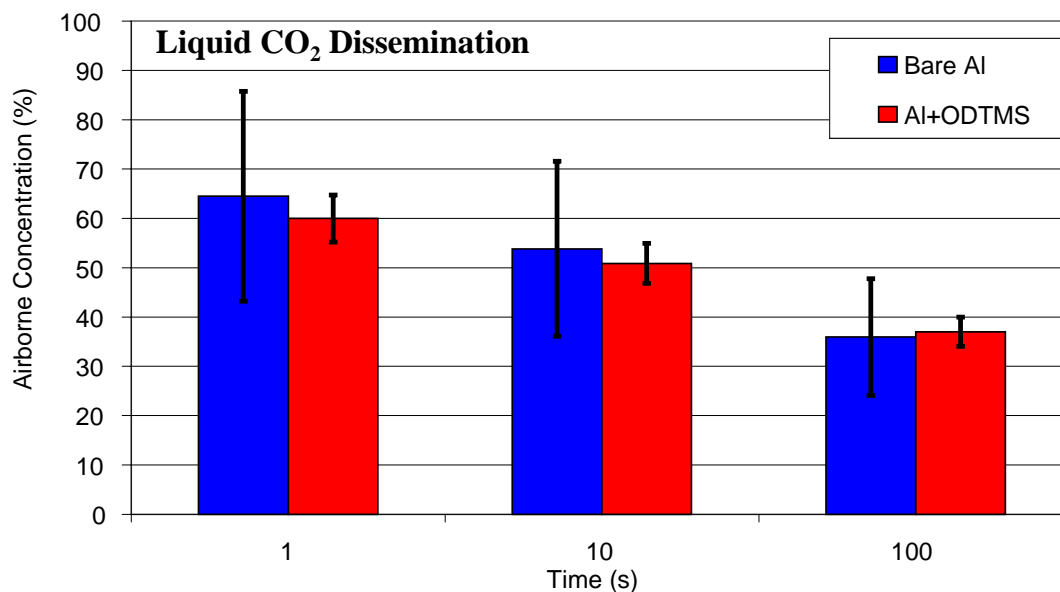


Figure 5-31. Airborne concentration of surface modified aluminum flakes at 50% humidity. The plot shows the airborne concentration of bare aluminum flakes, blue bars, and ODTMS surface modified aluminum flakes, red bars. Surface modification does not improve dispersion over liquid CO_2 dissemination alone.

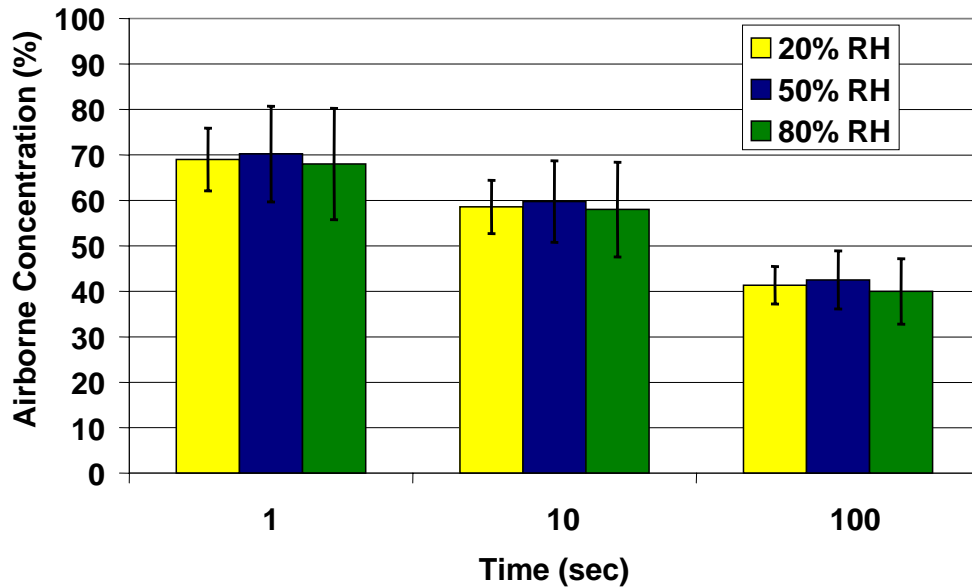


Figure 5-32. Airborne concentration of bare aluminum at 20, 50, and 80% humidity. Using liquid CO₂ dissemination, the usual effect of increasing relative humidity on increasing agglomeration is no longer a factor due to the improved dispersion method.

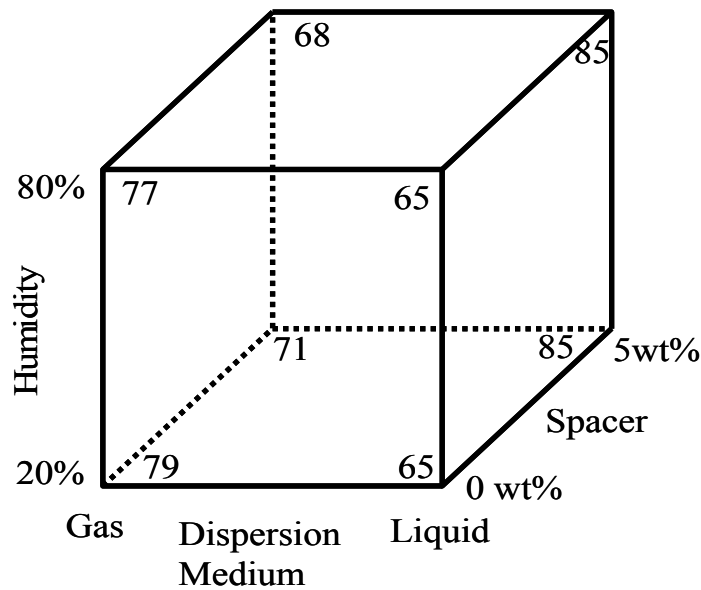


Figure 5-33. Experimental design dispersion results. The figure shows the results for airborne concentration for all of the experiments used to investigate the effect of humidity, spacer, and dispersion medium. The conditions for optimum dispersion can be seen to result from 5 wt% spacer and liquid CO₂.

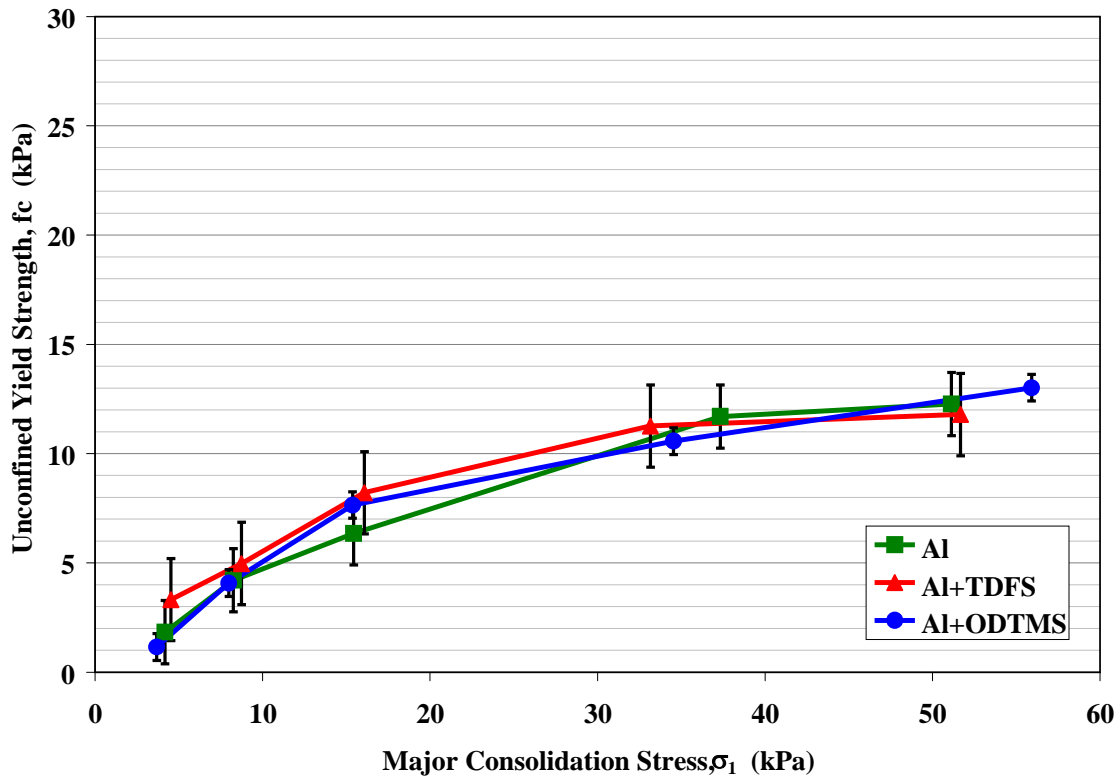


Figure 5-34. Unconfined yield strength versus major consolidation stress at 20% relative humidity. The plot shows the unconfined yield strength, f_c , versus major consolidation strength, σ_1 , for bare aluminum powder, diamonds, and aluminum powder surface modified with OTDMS, circles, and TDFS, squares, at 20 percent relative humidity. van der Waals and frictional forces dominate the interparticle forces and no significant difference in f_c is seen.

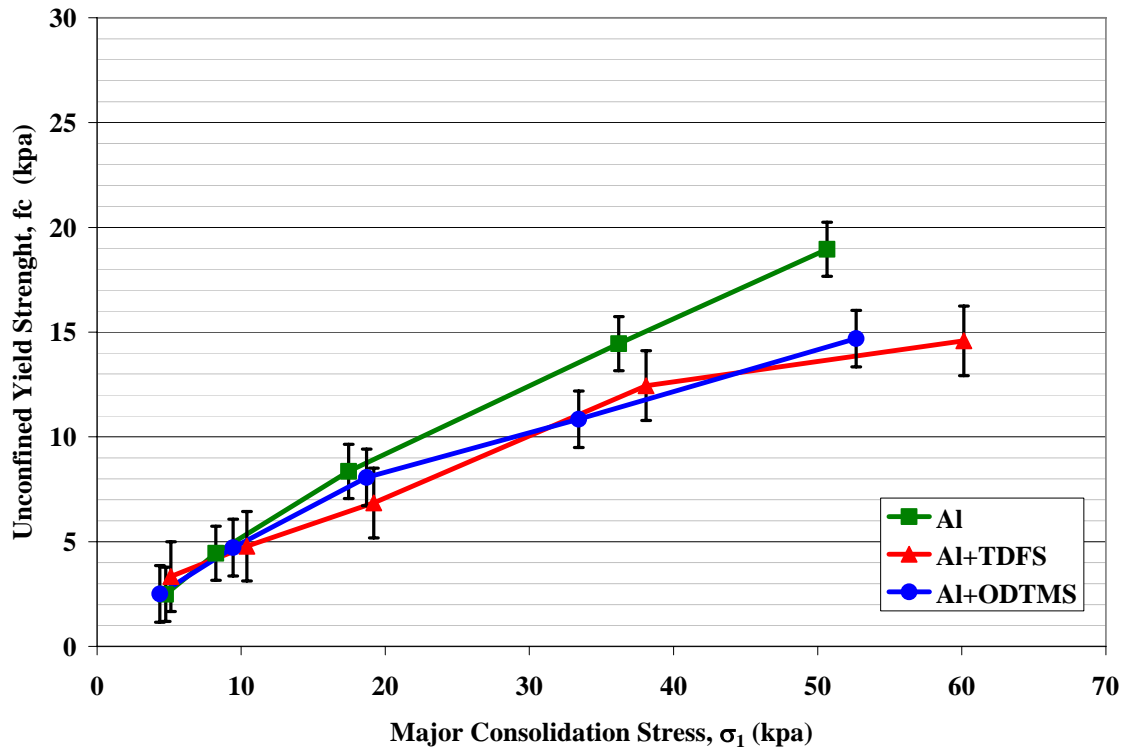


Figure 5-35. Unconfined yield strength versus major consolidation stress at 50% relative humidity. The plot shows the unconfined yield strength, f_c , versus major consolidation strength, σ_1 , for bare aluminum powder, squares, and aluminum powder surface modified with OTDMS, circles, and TDFS, triangles, at 50 percent relative humidity. A significant increase in strength of 37% is seen in the bare aluminum, while a smaller increase of 17% is seen for the surface modified powders. Capillary forces in the liquid pendulums between particles increase the adhesion force and in turn the unconfined yield strength.

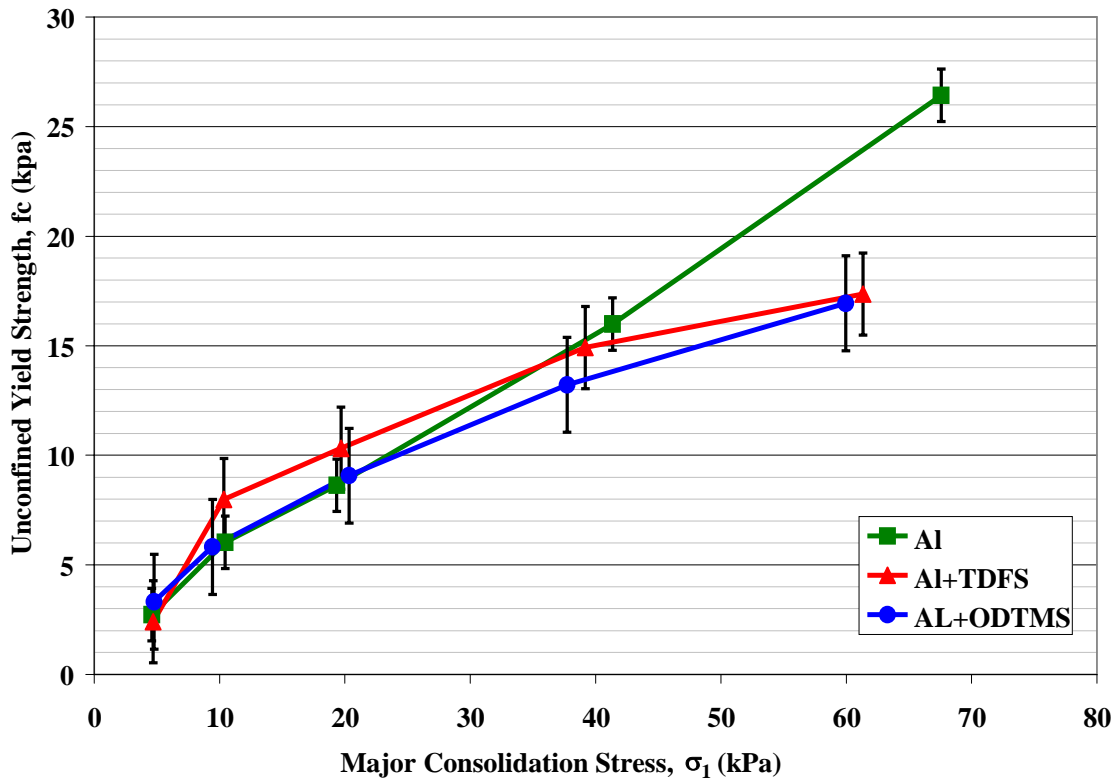


Figure 5-36. Unconfined yield strength versus major consolidation stress at 80% relative humidity. The plot shows the unconfined yield strength, f_c , versus major consolidation strength, σ_1 , for bare aluminum powder, squares, and aluminum powder surface modified with OTDMS, circles, and TDFS, triangles, at 80 percent relative humidity. A further increase in strength of 25% is seen in the bare aluminum, while no significant increase is seen for the surface modified powders. Capillary forces in the liquid pendulums between particles increase in the bare material as more water is adsorbed. There is no significant increase in adsorbed water on the modified materials as seen by the constant unconfined yield strength.

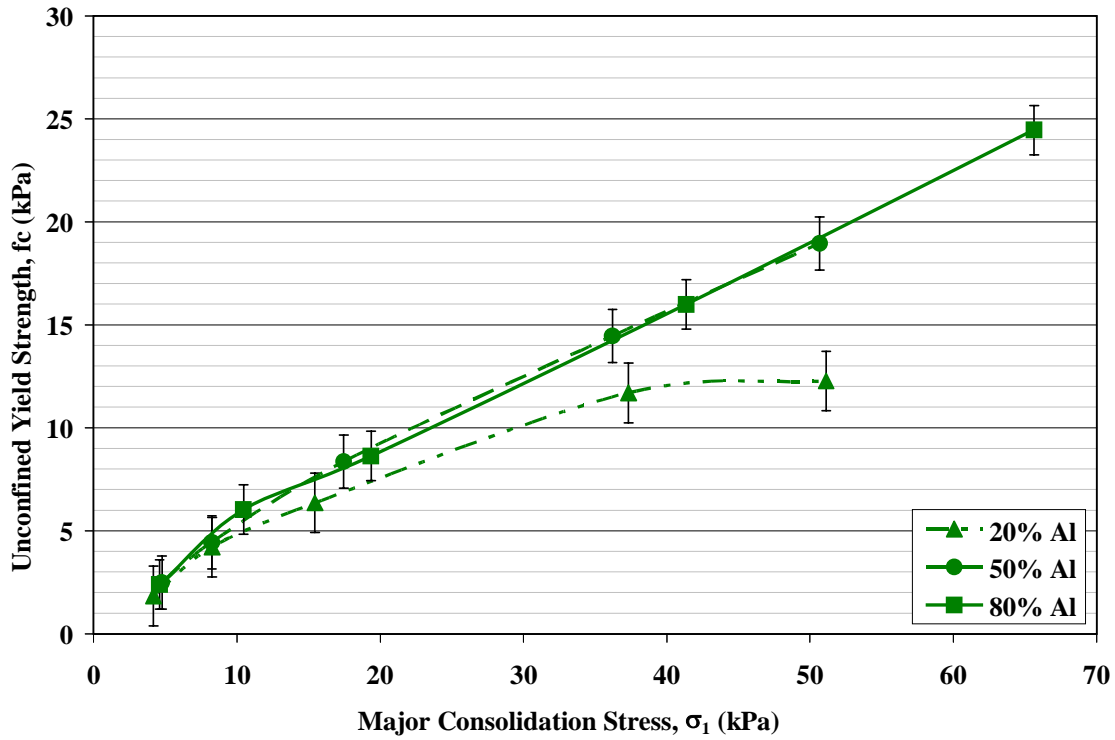


Figure 5-37. Unconfined yield strength versus major consolidation stress for bare aluminum. The plot shows the unconfined yield strength, f_c , versus major consolidation strength, σ_1 , for bare aluminum powder at 20%, 50%, and 80% humidity. An increase in strength can be clearly seen as the relative humidity increases. This is due to the additional capillary adhesion force between the particles due to liquid adsorbed from the increased relative humidity.

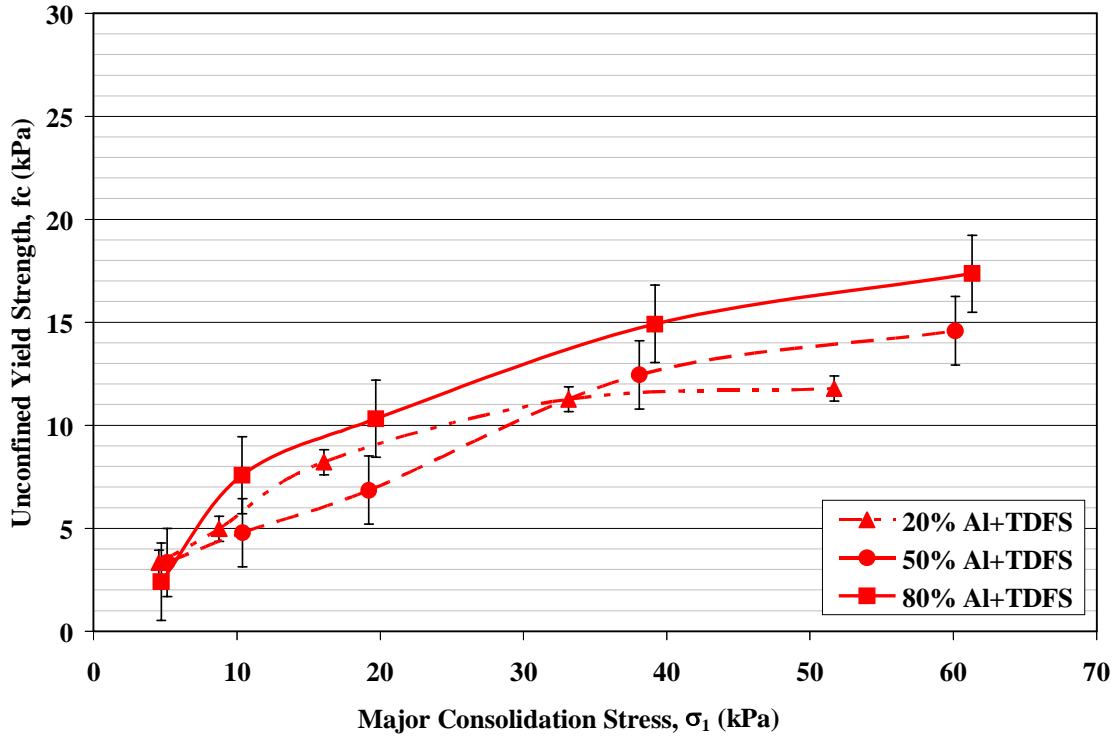


Figure 5-38. Unconfined yield strength versus major consolidation stress for TDFS modified aluminum. The plot shows the unconfined yield strength, f_c , versus major consolidation strength, σ_1 , for aluminum powder surface modified with TDFS at 20%, 50%, and 80% humidity. A small increase in strength can be seen as the relative humidity increase from 20 -50%, however no significant increase in seen as the relative humidity is further increased to 80%. These results indicate that the powder is not completely hydrophobic and due to some adsorbed water additional capillary adhesion force between the particles lead to the initial increase in strength at 50% relative humidity. Since there is not significant increase in strength at 80% relative humidity, it is concluded that no further adsorption occurs.

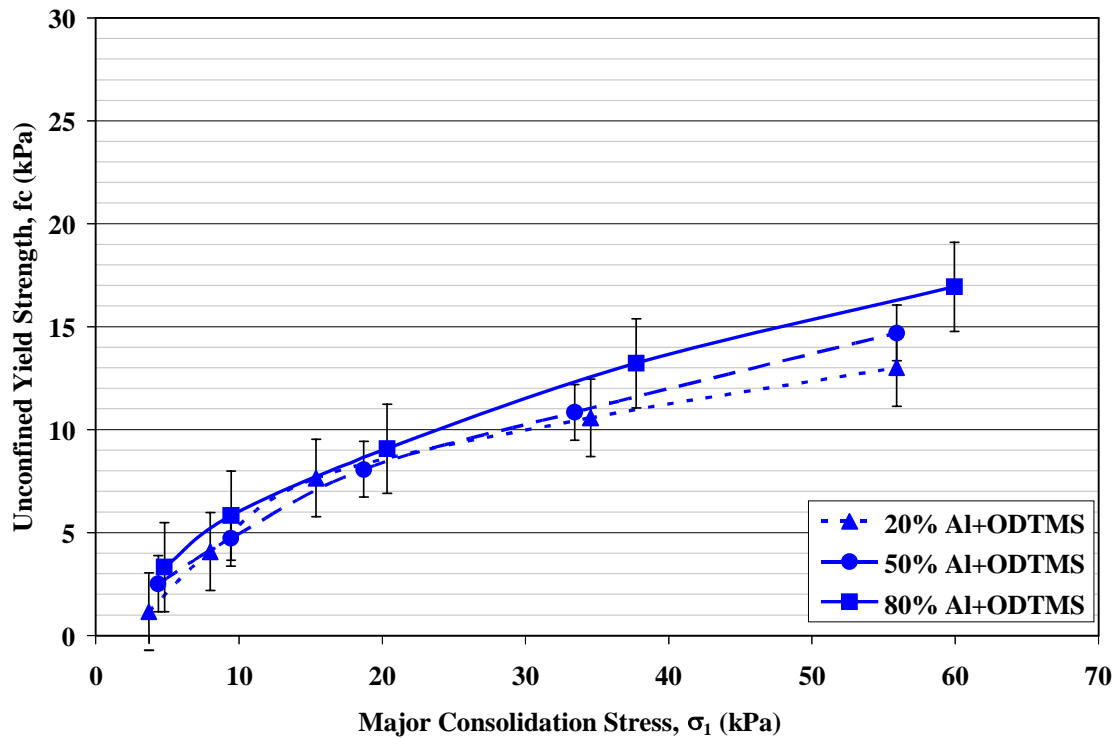


Figure 5-39. Unconfined yield strength versus major consolidation stress for ODTMS modified aluminum. The plot shows the unconfined yield strength, f_c , versus major consolidation strength, σ_1 , for aluminum powder surface modified with TDFS at 20%, 50%, and 80% humidity. A trend towards an increase in strength can be seen as the relative humidity increase from 20 -80%, however no significant increase in seen. These results indicate that the powder is hydrophobic and no significant adsorption of water occurs. By controlling capillary forces the powder strength can be controlled.

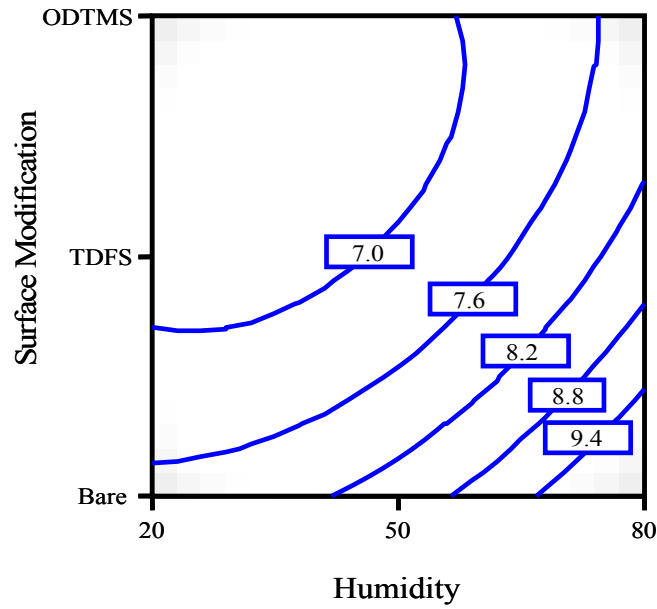


Figure 5-40. Response plot for unconfined yield strength. The contour plot from Design Expert shows the effect of humidity and surface modification on the unconfined yield strength of the bulk powder. Surface modification can be used to control the effect of humidity.

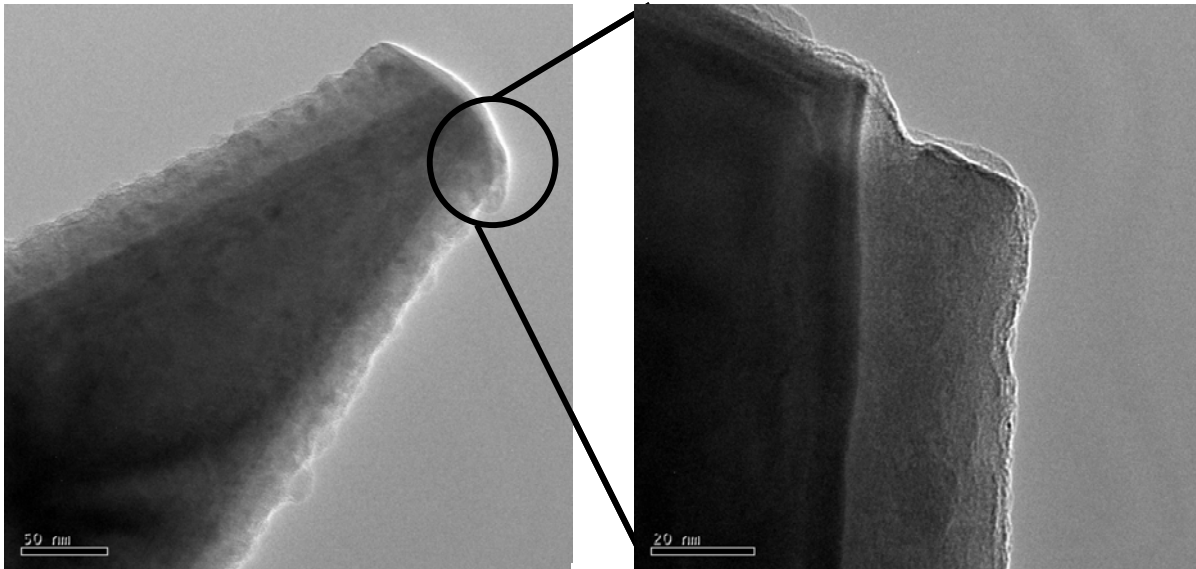


Figure 5-41. Damaged aluminum coating on cantilever tip. The CVP aluminum coating was not hard enough for force measurements and was damaged after contact with the aluminum substrate. This led to the use of aluminum particle probes.

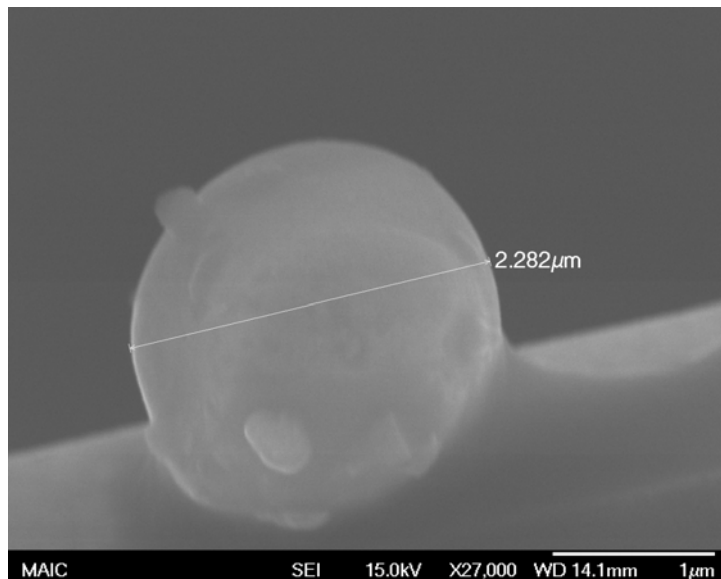


Figure 5-42. Bare aluminum particle probe. A bare spherical aluminum particle attached to tipless silicon cantilevers can be seen in this SEM image. A particle probe such as this one was used in order to measure interparticle forces at varying relative humidity levels. The spheres' diameters were measured using a line analysis tool in the SEM software.

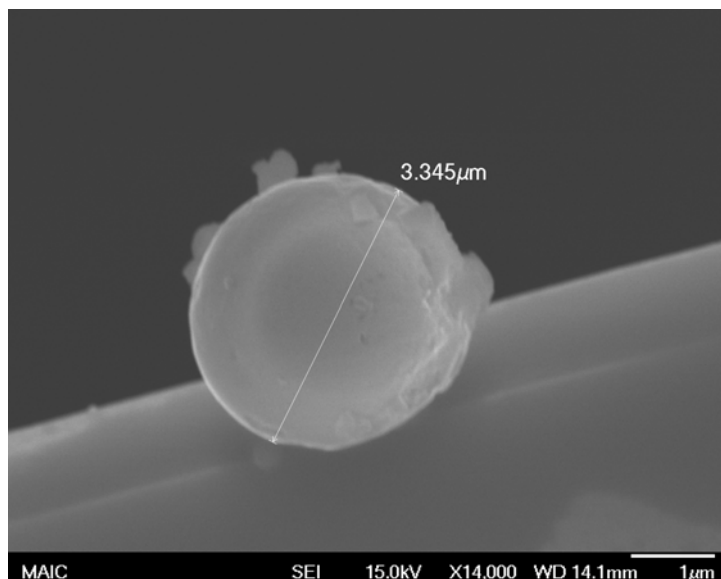


Figure 5-43. ODTMS modified Aluminum particle probe. SEM image of an ODTMS modified aluminum particle attached to a tipless cantilever, one of the particle probes used to measure the interparticle forces between surface modified aluminum at varying relative humidity.

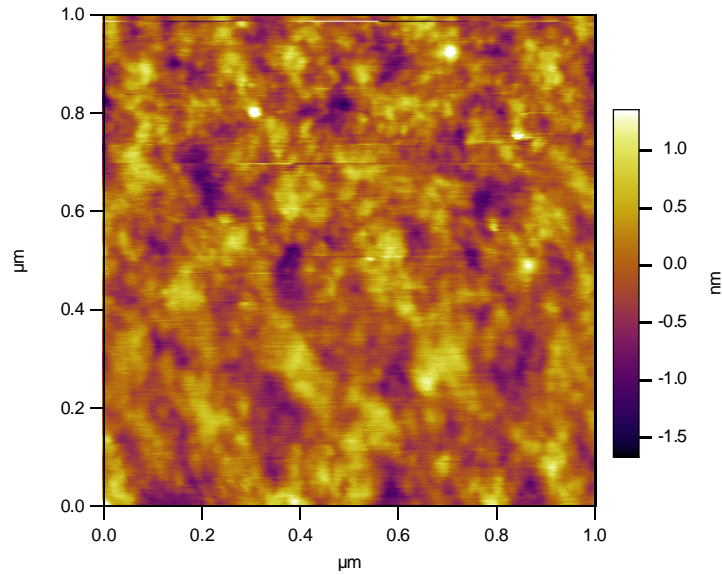


Figure 5-44. Contact mode image of the CVD bare aluminum surface. Using a $1\mu\text{m} \times 1\mu\text{m}$ 2D contact mode image of bare CVD aluminum the rms surface roughness was measured to be 1.6nm.

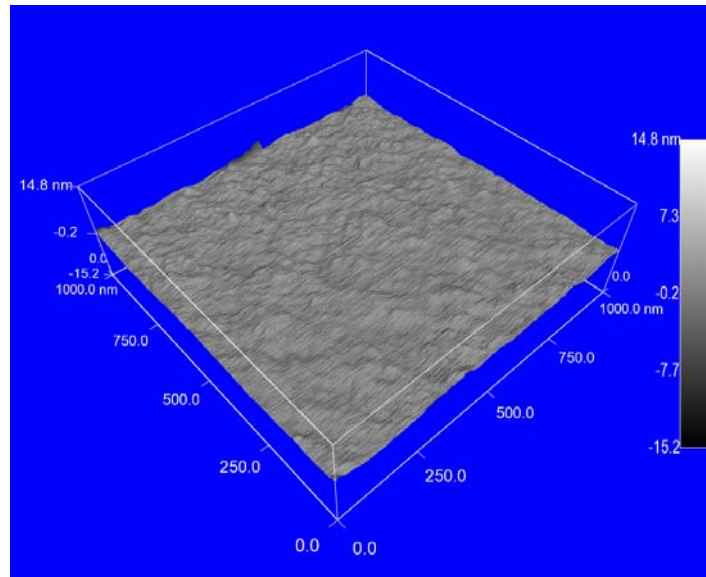


Figure 5-45. Contact mode image of bare aluminum in 3D. The surface roughness of the bare CVD aluminum surface can be seen in this $1\mu\text{m} \times 1\mu\text{m}$ 3D contact mode.

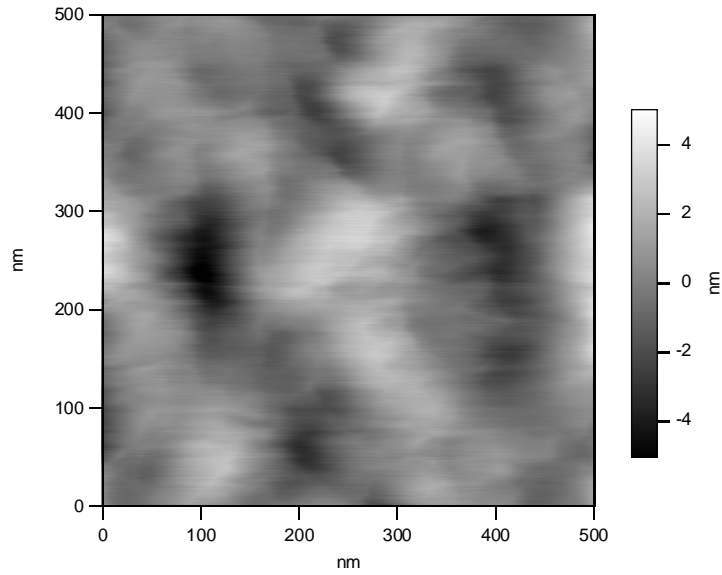


Figure 5-46. Detailed contact mode image of bare CVD aluminum. The surface roughness of the aluminum can be seen in this 500nm x 500nm 2D contact mode image of bare CVD aluminum.

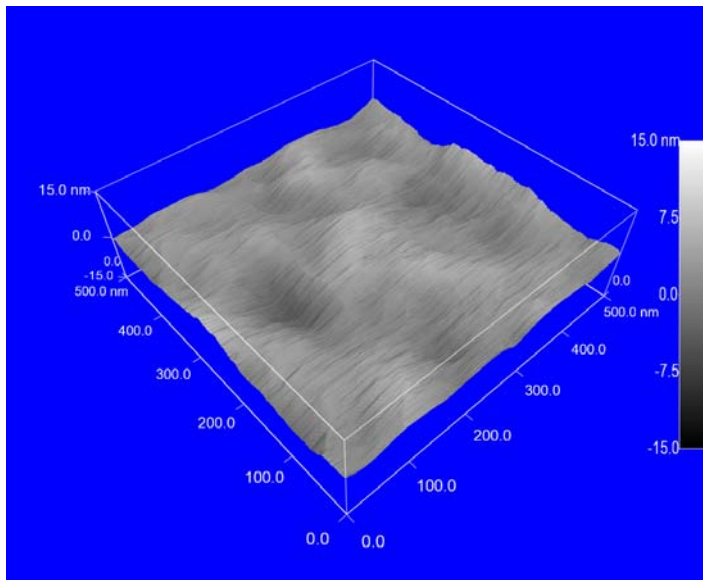


Figure 5-47. Contact mode image of bare aluminum in 3D. The surface roughness can be better appreciated in this 500nm x 500nm 3D contact mode image of bare CVD aluminum.

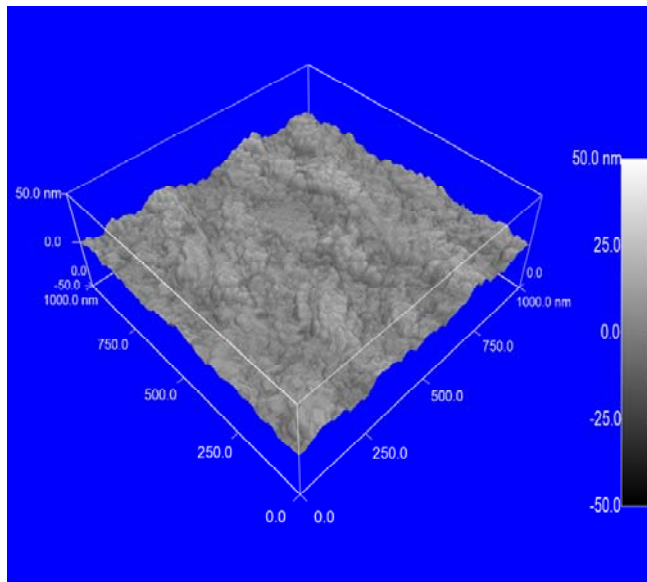


Figure 5-48. Contact mode image of ODTMS modified aluminum. A $1\mu\text{m} \times 1\mu\text{m}$ 3D contact mode image of a ODTMS modified CVD aluminum surface. The average rms surface roughness for these samples was measured to be 1.8nm.

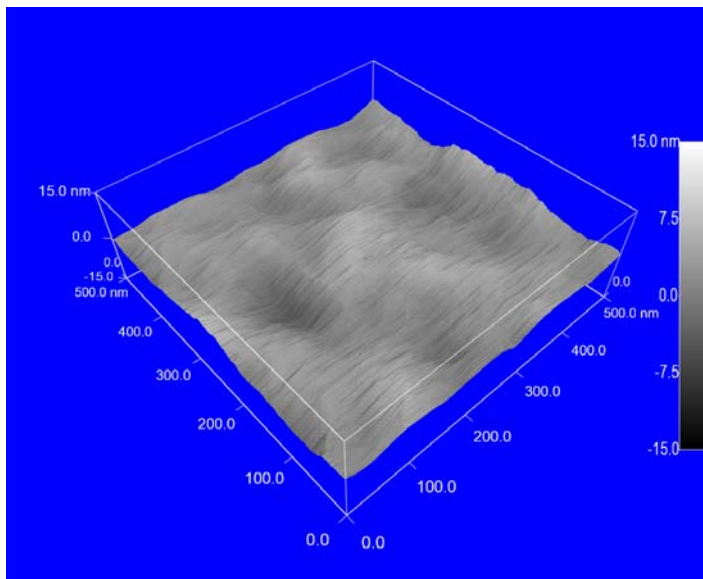


Figure 5-49. Contact mode image of ODTMS aluminum in 3D. To obtain a better sense of the surface roughness, a 500nm x 500nm 3D contact mode image of ODTMS modified CVD aluminum.

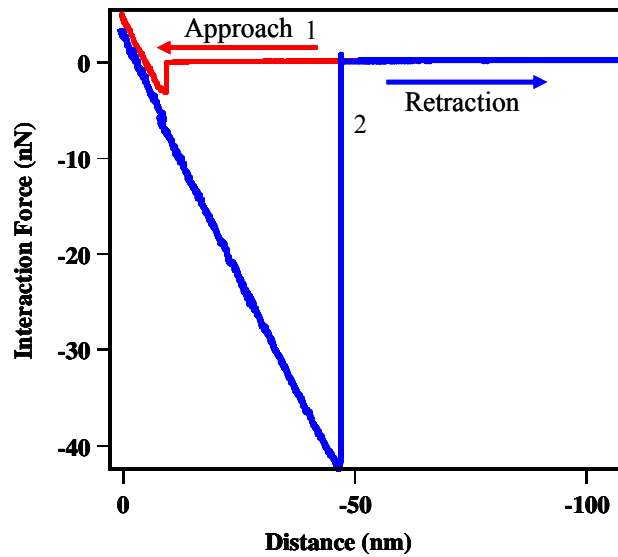


Figure 5-50. Typical force distance curve. As the particle and surface approach each other, represented by line 1, the onset of interaction is shown by the jump-to-surface point. Once the particle is in contact with the surface, the cantilever bends slightly as seen by the upward slope of the line. After a maximum deflection equal to 5nN, the software triggers the piezoelectric changes direction and the particle and surface move apart. During retraction, represented by line 2, the point of particle release is seen by the jump-off-surface point. From the deflection distance and cantilever spring constant the force of interaction is calculated.

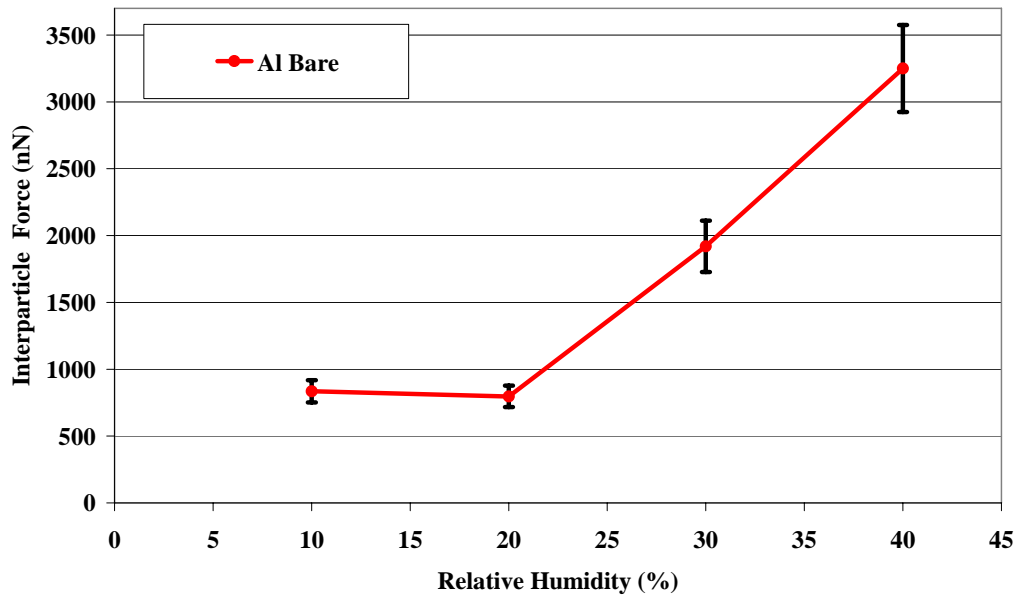


Figure 5-51. Interparticle force at humidity for bare aluminum. The graph shows the interparticle adhesion force between a bare aluminum particle and substrate. At low relative humidity, van der Waals forces dominate and no change in force is seen. As humidity increases, the amount of water adsorbed on the surface also increases. Once enough water is present to form a meniscus at the contact point between the particle and surface, capillary forces arise leading to an increase in adhesion force.

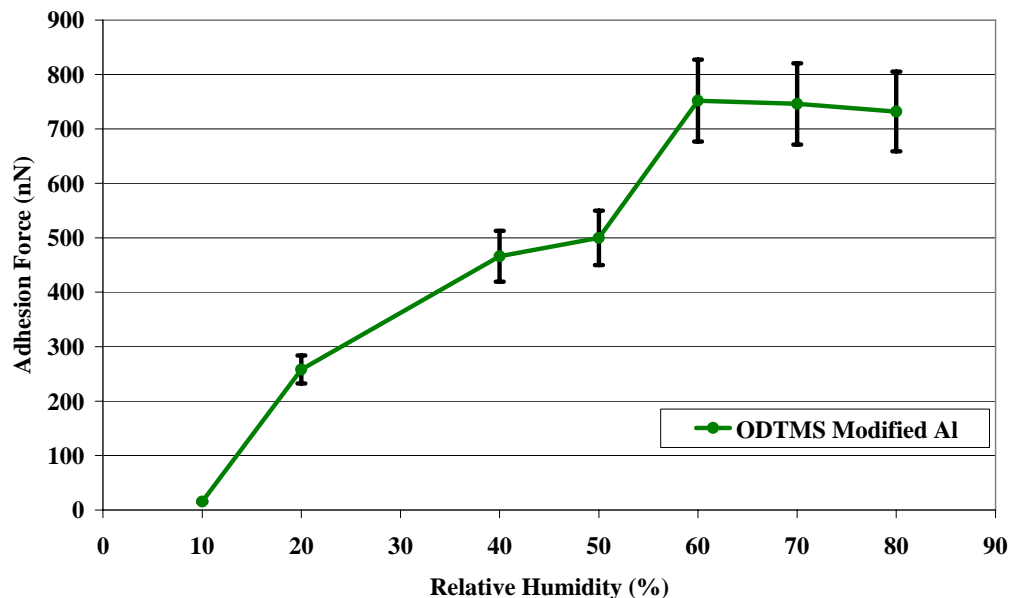


Figure 5-52. Interparticle force at humidity for ODTMS modified aluminum. This graph shows the interparticle adhesion force between an ODTMS modified aluminum particle and substrate. At low relative humidity, van der Waals forces dominate. As humidity increases, the amount of water adsorbed on the surface also increases, and capillary forces arise leading to an increase in adhesion force. Because the hydrophobic surfaces created by the ODTMS modification are not completely hydrophobic (the contact angle was 110° much less than 180°) some water can adsorb onto the surface as seen by the increased adhesion. However, the effect of this partial hydrophobicity can be seen by only a minimal increase in adhesion forces.

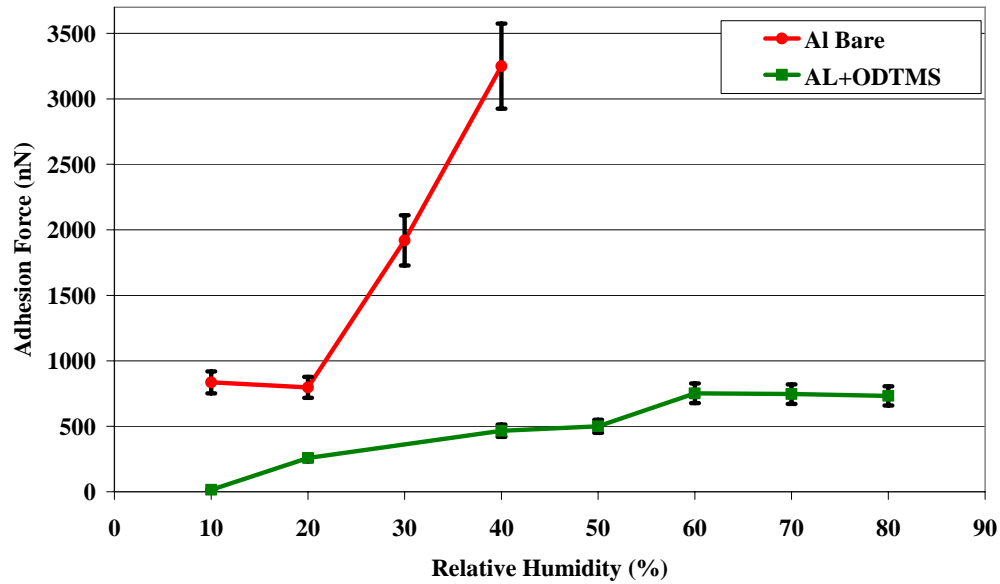


Figure 5-53. Comparison of the effect of surface modification. Inspection of this graph comparing the adhesion force for that of bare aluminum and of surface modified aluminum, the extent to which the surface modification decreases the effect of capillary forces can be seen. Even though the ODTMS does not create a perfectly hydrophobic surface, contact angle of 180° , there is still a very significant effect on interparticle forces and a much lower adhesion force is measured.

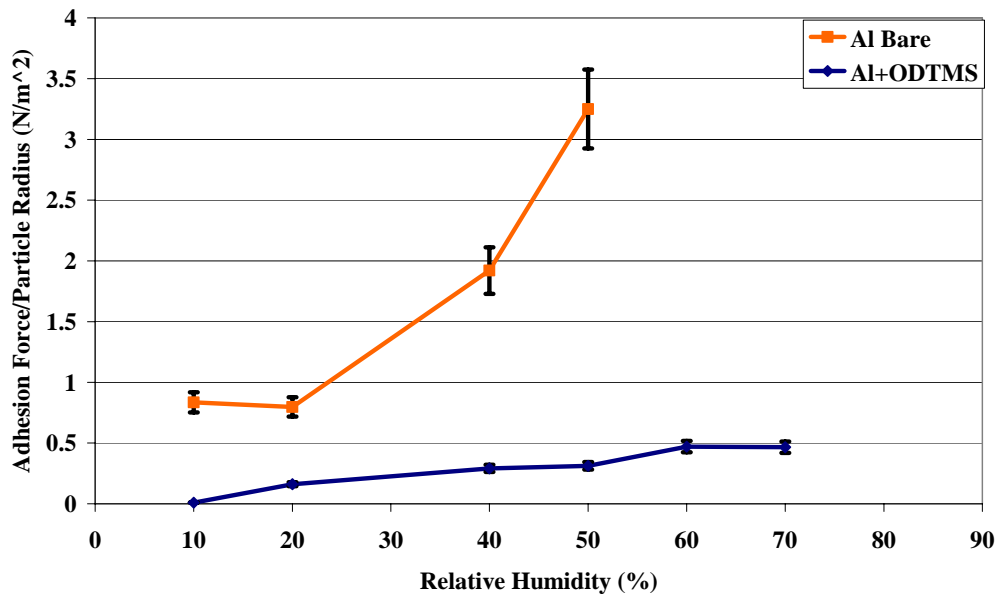


Figure 5-54. Interaction energy and surface modification. Dividing the interaction force by the radius of the particle on the probe yields the energy of interaction per unit area. This allows the comparison of this data for spheres to that of other geometries of interest such as flakes.

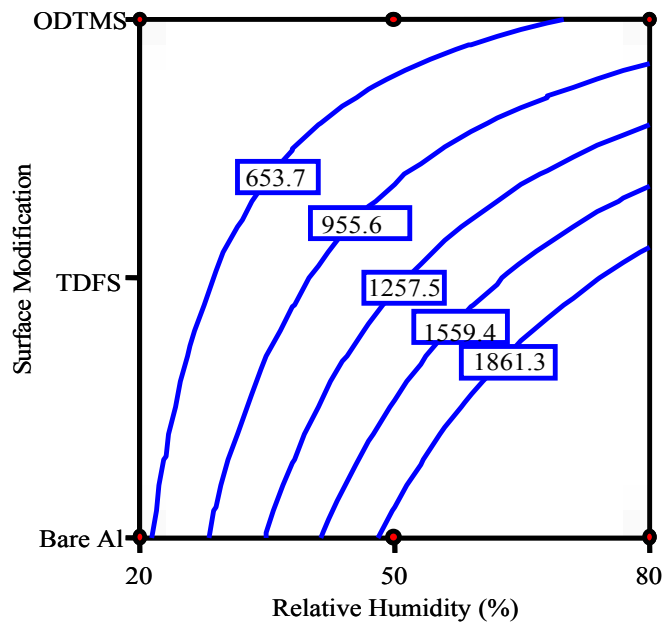


Figure 5-55. Response plot for adhesion force. The contour plot from Design Expert shows the result of changing relative humidity and surface modification on the adhesion force between a particle and surface. Surface modification is shown to lower adhesion force even at high relative humidity.

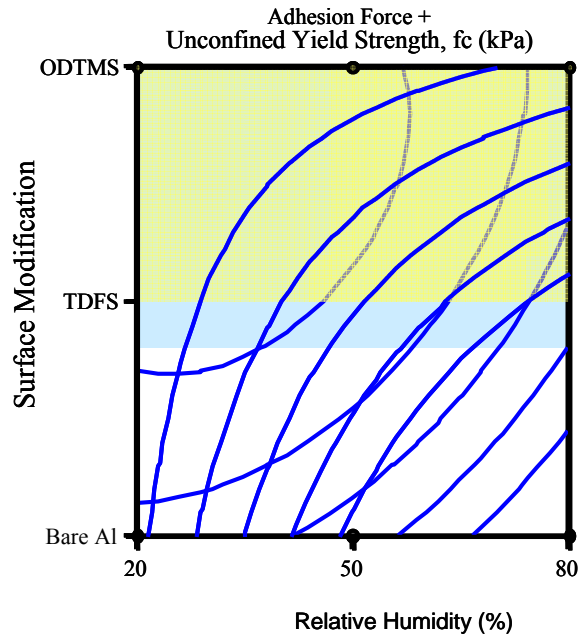


Figure 5-56. Overlay of response plots. By overlaying the response contour plots from both the shear cell and AFM experiments the optimum results for all conditions can be seen. This plot can now be compared to the experimental results also.

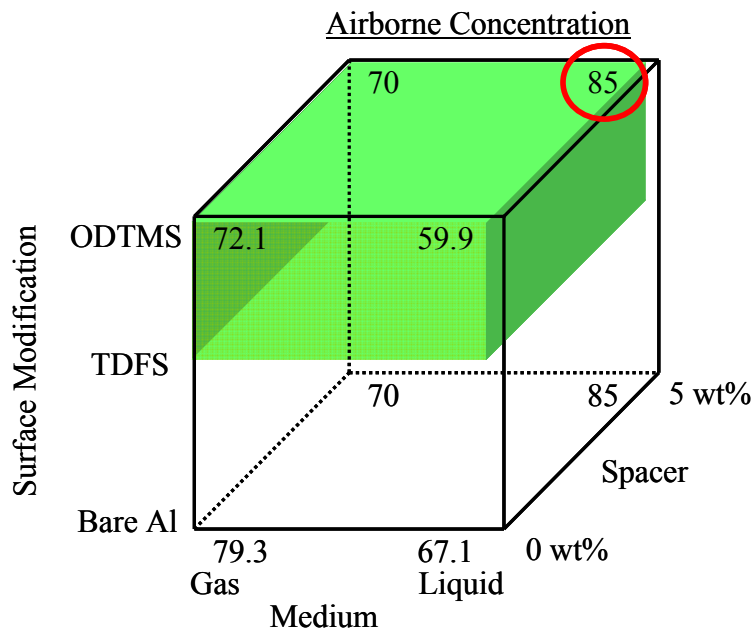


Figure 5-57. Overlay of contour on airborne concentration results. From the overlay shear cell and AFM results, optimum performance requires surface modification, limiting the conditions to those in the upper portion of the cube. Thus the optimum conditions are seen to be Surface modification, 5% spacer, and liquid CO₂ dissemination.

Table 5-1. Summary of optimum surface modified aluminum. The table shows the contact angle measurements of water for bare aluminum and aluminum surface modified with ODTMS and TDFS as well as the calculated work of adhesion. These results are for a reaction time of one hour, which was determined to be the optimum time.

Contact Angle			
	Aluminum	ODTMS	TDFS
Advancing	67.2	113.5	110.5
Receding	7.8	68.5	43.0
Work of Adhesion - W_a (J/m ²)			
	Aluminum	ODTMS	TDFS
Advancing	101.9	43.8	47.3
Receding	144.9	99.5	126.0

CHAPTER 6 CONCLUSIONS

Improving aerosol dispersion requires knowledge of the significant interparticle forces of the system and the method to control them, an aspect that has been previously by and large neglected. Through this research, a systematic investigation of the effect of significant factors on powder dispersion in air has been conducted. An understanding of the effect of these factors on dispersion, the magnitude of their effect, and the subsequent change in interparticle forces has been developed. Using this approach, the interparticle forces of any system can be determined allowing the determination of optimum processing methods to significantly alter those forces and ultimately improve dispersion.

In the first aspect of this research, factors that were determined to be significant to dispersion were investigated to determine not only their effect, but also magnitude, on dispersion. These factors included the physical factors of drying methods and contact area, as well as the chemical factors of capillary forces and surface modification. Dissemination methods were also investigated. The second part of this research involved developing an understanding of the reason for the observed effect. The change in dominant interparticle forces were measured and correlated to the processing parameters. Each will now be discussed in more detail.

Drying was shown to have a significant impact on producing a dry dispersible powder. Ineffective drying methods, such as evaporation and freeze drying, allowed the presence of a liquid – gas phase boundary and were shown to lead to strong interparticle adhesion due to the capillary forces found in the liquid bridges at particle contacts. The capillary forces drew particles together which allowed van der Waals adhesion forces to become significant. An increase in mean particle size of near 10 – 100 times the primary particle size as a result of capillary force driven agglomeration was seen. Drying the Sigma aluminum flake powder with a

12 μm mean particle size by evaporation and freeze drying led to a dry powder mean particle size of 600 μm and 300 μm respectively. The third drying method using supercritical liquid CO₂ was shown to overcome this challenge and effectively eliminate capillary forces by the complete avoidance of a liquid-gas interface through the use of the supercritical phase. The unique properties of supercritical fluids, in particular the lack of surface tension due to no definable liquid vapor phase boundary, resulted in the elimination capillary forces. This method was further developed and optimized for the production of a dry, dispersible powder. A dry aluminum flake powder with a mean particle size of 18 μm was produced, a significant improvement over any other drying method. Because of its superior results, supercritical drying became the standard drying process for all further research.

Interparticle adhesion, specifically by van der Waals forces, is known to be affected by the contact area between the surfaces. Through the use of spacer particles, the contact area between the flake surfaces was controlled and in turn the adhesion forces were decreased. By calculation, a theoretical reduction in van der Waals attraction of 1×10^7 N was found by including spacer particles in the aluminum matrix. Empirically, it was demonstrated that the addition of 5 weight percent of spacer particles resulted in a 10% increase in airborne particle concentration.

Dissemination methods using varying pressure and medium phase were also investigated in order to optimize dispersion. The airborne concentration was shown to be related to dissemination pressure and improve by increasing dissemination pressure to 800psi. A maximum airborne concentration of 80% was seen under these conditions. Calculation of the minimum turbulent eddy size showed that despite the high pressure, a minimum eddy of only 1.2 μm was possible. However, the thickness to which the force needed to be applied was only 12nm, well below the minimum eddy size.

To overcome this challenge, a novel method was developed using liquid CO₂ as the dissemination medium. Through this method, the particles were dispersed in a liquid that expanded in volume during dissemination because of its phase change to a gas, the thermodynamically favored state at standard temperature and pressure, once released from the device. The expansion added a radial force, on the order of magnitude of the interparticle forces, in addition to the shear normally produced through dispersion. The volume between bare flakes, calculated based on their surface roughness, however, was not sufficiently large for enough liquid CO₂ to reside to aid in dispersion. However, once the spacer was added, the significant increase in volume between the flakes, and therefore of liquid CO₂, led to a significant increase in dispersion. A 20% increase in airborne concentration when liquid CO₂ dissemination was employed, and the maximum airborne concentration of 85% was produced.

Capillary forces that develop due to moisture in the form of relative humidity were shown to result in agglomeration and a five fold increase in dry particle size from 10 to 50µm as relative humidity was varied from 20 to 80%. The creation of a hydrophobic surface through the use of surface modification was employed to control agglomeration caused by humidity. Two silanes, n-octadecyltrimethoxysilane (ODTMS) and tridecafluoro-1,1,2,2-tetrahydrooctyl-1-triethoxysilane (TDFS), were used. ODTMS was shown to create a hydrophobic surface with an advancing water contact angle change from bare aluminum measured to be $67 \pm 3^\circ$ to that of ODTMS modified surface of $114 \pm 1^\circ$. TDFS was shown to produce a slightly less hydrophobic surface with a measured contact angle of $111 \pm 3^\circ$ under the same conditions.

The CO₂ dissemination method was again used to investigate the ability of this method to disperse powder that was preconditioned at the varying humidity as described for the particle size measurements above. It was shown to be equally effective regardless of the powder

conditioning prior to dissemination using liquid CO₂. This was the case even for the bare aluminum, which was susceptible to the most significant agglomeration due to capillary forces. Despite conditioning for 48hr at high humidity, the increased agglomeration seen in the particle size measurements was not seen in liquid CO₂ dissemination. No significant decrease in airborne concentration was seen as the relative humidity was increased from 20-80%.

With the use of statistical design, these results were evaluated to determine both their significance and the magnitude of their effect. It was shown that the interaction between the spacer addition and dispersion medium had the largest effect on airborne concentration. From this data, a relationship was also developed to determine airborne dispersion based on the factor levels, namely Equation 5-1. The optimum levels of each factor were also determined. They were surface modification, 5 weight % spacer, and liquid CO₂ dissemination.

Next, the change in interparticle forces associated with these factors was investigated. It has already been shown that contact area reduced van der Waals forces and that the liquid CO₂ dissemination, given a sufficient volume, will add a radial force on the same order of magnitude as the van der Waals adhesion. In addition, the bulk powder properties and interparticle forces were also investigated.

Since in most aerosol applications the powder is drawn from a reservoir, bulk powder forces are important. It was shown that at low humidity levels, only van der Waals and frictional forces contributed to adhesion, however, at higher humidity capillary forces dominated. Through the use of surface modification, the adhesion force at high humidity could be controlled. With ODTMS surface modification, unconfined yield strength could be controlled and no significant increase in adhesion was seen at any humidity level.

To understand the effect at the particle level, the atomic force microscope was used. Interparticle forces were measured between bare and surface modified aluminum spheres and substrates. The bare aluminum at low humidity had an adhesion force of 850nN which is in close agreement with the calculated value. A critical humidity was reached at 20% relative humidity at which point a large enough amount of water adsorbed to the surface that a meniscus formed at the particle/surface contact and an increase in adhesion force due to the additional capillary contribution was seen. As the relative humidity increased, so did the volume of liquid in the meniscus and therefore the magnitude of the capillary forces. The ODTMS modified surfaces showed an initial adhesion force much lower than that of the bare aluminum surface. This was due to the lower surface energy of the modified surface and the steric barrier created by the silane. Taking this into account, the adhesion force could be compared to the calculated value. As humidity was increased, the adhesion force also increased slightly. The surfaces are therefore not completely hydrophobic and some water can adsorb. The maximum adhesion force at 80% humidity was an order of magnitude lower for the surface modified materials as compared to the bare aluminum surfaces. This result shows that the surface modification does work to control both the interparticle forces and capillary forces.

The correlation of the two aspects of this research shows not only the factors that effect dispersion as seen by an increased airborne concentration, but also the change in interparticle forces that are responsible for the change. From this understanding, information of what interparticle forces are involved in adhesion is enough to determine what processing parameters should be changed thereby allowing the application of this knowledge to other powder systems.

CHAPTER 7 CASE STUDY: ARMY OBSCURANTS

Introduction

Obscurant smokes and clouds are commonly used by the U.S. Army as a defense against spectral targeting and have been for centuries. Advancements in technology have led to communication and detection systems now functioning in the infrared and microwave region of the electromagnetic spectrum. For this reason new obscurant materials are under investigation to meet these requirements. An initiative has been undertaken by the US Army to improve the current infrared obscurant grenades by a factor of four. Modeling by Army and independent civilian scientists has shown that high aspect ratio metal particles would result in the maximum performance[115-120]. Despite the extent of commercially available materials, none meet the specifications to achieve these goals.

A large amount of work has been put towards fabricating a flake material with the desired characteristics. This is, however, only the first challenge. The Infrared attenuation efficiency of a particulate cloud is dependent on the particle characteristic and the amount of material in the cloud available to attenuate the light. Particle dispersion is therefore essential to the optimization of an obscurant particulate cloud. In order to maximize the number of particles in the cloud all of the material discharged must disperse into primary particles.

The focus of this research was to apply the knowledge gained through this dissertation research to develop an understanding of the particle-particle interaction between the chosen particulate systems, determine the properties that control dispersion, and develop methods to controllably manipulate these properties through processing in order to develop an obscurant material that meets the performance criteria of a four times improvement over the current material across the selected region of the infrared spectrum.

Performance parameters have been selected by the Army to characterize a material's ability to obscure in the wavelengths of interest[116, 121, 122]. The ratio of aerosol mass to transported precursor material mass, or yield factor, is the first performance parameter. The second is the electromagnetic extinction cross section per mass of aerosol. This refers to the extinction cross section, or shadow, created by the aerosol cloud. The third performance parameter is deposition velocity which is a measure of the settling rate of the cloud as it is transported downwind. Each of these factors will be influenced by the degree of powder dispersion.

Particle shape also plays a role in the overall aerosol attenuation efficiency. Particles that have been found to produce the greatest extinction over the selected wavelengths are small absorbing particles, flakes, hollow particles, and particles producing an optical resonance of some kind[121]. A wide variety of commercially available including highly absorbing materials like carbon black and graphite as well as man-made graphite flakes have also been investigated[123, 124] however a material generating greater extinction is desired. Through the use of fully dispersed aerosols of engineered high aspect ratio particles improvements in efficiency of up to an order of magnitude are theoretically possible.

Improvements have been shown by taking advantage of the nanodimension. By using high aspect ratio particles, such as flakes, the effective scattering area per unit volume of the material in the aerosol cloud will be dramatically increased. There are some challenges, however, to dispersing particles of this shape and size range. High aspect ratio particles have much larger contact area and decreasing the flake thickness into the submicron range significantly increases the surface to mass ratio. In turn the effect of surface forces is much higher leading to an increase in the cohesiveness of the powder. The fundamentals associated with these interactions

must first be understood and then processing methods developed to control dispersion in order for the maximum obscurant performance to be realized.

Experimental

It is readily acknowledged that dispersion in air is a complex multifaceted problem and requires a systematic approach in order to determine the significant factors. For this reason statistical design of experiments is used to guide the research. Drying has already been shown to be important and supercritical drying was used exclusively. The first two factors under investigation were flake thickness and the addition of a spacer material. Suspensions of different thickness aluminum flake powders with and without fumed silica were characterized and then dried and the effects of these factors on performance, and dispersion, were evaluated. Finally the dissemination method was also considered and a novel liquid carbon dioxide method was investigated

Factors and Preparation:

Flake thickness

The number of particles in the aerosol is constrained by their size and the volume of the container from which they are dispersed. By decreasing the particle thickness, while maintaining the diameter, the volume of each particle is decreased without changing the performance of the individual flake. As a result, a higher number of particles can be packed into the same volume. As can be imagined, there will be a point of diminishing return. Once the flake thickness is decreased beyond a point, two problems will arise. First, the flakes will become transparent as there is not enough material to interact with the infrared radiation[119]. In addition, the mechanical strength of the flake decreases and they are no longer flat and ridged, but instead bend or curl on themselves.

Commercially available aluminum flake materials of three different thicknesses were received. Vapor phase deposited material of 15nm and 35nm mean thicknesses were received from Sigma Technologies, Inc and a milled material with a 60nm mean thickness was received from Silberline®. All of the powders were received in paste form and solvent exchanged three times with isopropyl alcohol (IPA) to remove any other solvents or contaminants. The non-polar nature of IPA resulted in a well dispersed Al suspension. The final aluminum – IPA suspensions were between 10 and 20 weight percent solids for supercritical drying.

Spacer material

High aspect ratio particles have a very high surface area to mass ratio. That is, because the thickness of the flake is an order of magnitude smaller than the diameter the contact area between the flakes is very high while the mass to which momentum can be applied is very low. For this reason, once these high aspect ratio flakes come into contact, dispersion can become impossible. If the contact area between flakes is decreased, the adhesion between them will also be decreased and dispersion can be improved. To achieve this goal, the flakes were mixed with fumed silica particles that act as spacers and prohibit the flakes from coming into intimate contact. The spacer material used was a 10nm mean diameter superhydrophobic fumed silica, Degussa Aerosil® LE2. The addition of the silica can also have a harmful effect: since the silica does not attenuate in the infrared, the addition of silica past the point of improving dispersion will decrease the amount of aluminum material per mass and decrease the aerosol performance. Therefore, the spacer was added at 0, 5, 10 weight percent.

All suspensions were then dried using the supercritical CO₂ drying processing developed in this research. The dry powders were then dispersed in a Galai® vacuum dispersion chamber onto (1) a glass microscope slide and (2) a Dual Pass Transmission (DPT) slide for evaluation in the FTIR.

Characterization

Particle size and morphology

As discussed in Chapter 4, although high aspect ratio particles do not completely agree with the assumptions needed for accurate light scattering measurements, size analysis on a volume basis has been shown to reliably describe the particle diameter as has been confirmed by Image Analysis. The particle size distribution of each material, as received, was measured in a well dispersed suspension with isopropyl alcohol. The particle size was also measured after processing, before drying, to verify the processing did not change the particle size. Scanning electron microscope (SEM) images and transmission electron microscope (TEM) images were also taken to understand the flake morphology, thickness, and the oxide layer.

Aerosol performance

Obscurant performance was assessed on two levels. Ultimately the entire system, a grenade, will be evaluated. For this, a figure of merit, or FoM_{grenade} shown in equation 8-1, was developed and takes into account all aspects of the system including material performance, amount of material in the grenade, and the amount of material that is dispersed into the aerosol.

$$FoM_{\text{Grenade}} = \alpha \rho_{\text{Fill}} Y \quad (8-1)$$

Here the α refers to the extinction cross section of the aerosol by mass; ρ_{Fill} is the fill density, or the density of the material multiplied by the volume of material in the grenade; and Y is the dissemination yield, or mass fraction of powder aerosolized in the cloud.

The material performance is based on production methods and material properties including conductivity, ductility, and density. The fill density is determined by the packing density of the material in the container. For high aspect ratio flakes, the packing density limit has been shown to be much lower than that for spheres and only minimal pressure can be applied

to increase packing or the flakes will deform and mechanical interlocking will prevent future dispersion. It is in the Y factor that the powder dispersion is taken into account. Agglomerated material will not contribute to the aerosol but instead fall to the ground. Increasing the powder dispersion will result in more material in the aerosol cloud, a longer cloud life, and therefore improved performance. The latter, dispersion, is the major focus of this case study. The effect of packing was also briefly investigated. Different packing and drying methods were used followed by FoM measurements of samples taken for evaluation.

Grenades were not developed through this research, instead the study centered on improving the material dispersion through processing, drying, and dissemination techniques. To evaluate the material performance, instead of making a grenade, a figure of merit of the material, FoM_{material} , was developed using the Beer-Lambert Law as shown in Equation 8-2 and will be discussed in detail below.

$$FoM_{\text{material}} = \frac{-\log \frac{T}{100}}{c} \quad (8-2)$$

Here T is the transmission and c is the concentration in of the material obscuring the light.

Powder performance

Dual pass transmission (DPT) measurement In order to have a quick and effective screening process and to overcome the challenges presented by mixtures of materials, different characterization methods were developed and based on the scattering and absorption of the IR laser of the FTIR. The theoretical absorption of light is proportional to the number of particles present. By dispersing the powder onto DPT slides and measuring the transmission of IR light through the slide measured in a reflection mode the degree of dispersion and material performance can be evaluated. This method is especially useful for powders with silica added as

a flow aid; the metallic particles will attenuate light in the IR while the silica is transparent. This method follows the hypothesis that if the powder is more dispersed after processing, there will be a decrease in FTIR transmission as there will be a higher number of particles on the slide to attenuate with the laser. The mass of powder on the slide will directly effect the FTIR transmission also. For this reason, the transmission was normalized by the mass of powder on the slide. The amount of powder used was within the measurement error of lab balance so for a higher degree of accuracy Inductively Coupled Plasma Spectroscopy (ICP) was used and is described in detail below. This allowed the accurate measurement of masses well below those seen for these experiments. The material performance was determined based on the material Figure of Merit (FoM), or the improvement of the new materials over a standard material supplied by the US Army. FoM values at chosen IR wavelengths were calculated and plotted for each material processing technique. If dispersion of a constant mass of powder increased, the transmission would decrease and result in a higher FoM. On the other hand, powder agglomeration would be portrayed by a decrease in the FoM due to less laser attenuation. Decreasing the thickness of the flake by half will result in twice as many flakes per unit mass and theoretically half the transmission.

The standard procedure used for FoM measurements is as follows. The dry powders were dispersed in a Galai® vacuum dispersion chamber onto (1) a glass microscope slide and (2) a DPT slide. The powder was allowed to settle for forty five minutes after which the DPT slide was placed in the FTIR for measurement. The glass microscope slide was placed in a Nalgene® bottle with a dilute acid solution to dissolve the metal in order to accurately measure the concentration using the ICP. Mass is calculated by measuring the concentration of Al in

solution, corrected for the presence of the oxide layer, and normalized by the area of the glass slide.

Inductively Coupled Plasma Spectroscopy (ICP) The Perkin-Elmer Plasma 3200 Inductively Coupled Plasma Spectroscopy (ICP) system is equipped with two monochromators covering the spectral range of 165-785 nm with a grating ruling of 3600 lines/mm. The ICP operates on the principle of atomic emission by atoms ionized in the argon plasma. Light of specific wavelengths is emitted as electrons return to the ground state of the ionized elements, quantitatively identifying the species present. The system is capable of analyzing materials in both organic and aqueous matrices with a detection limit range of less than one part per million. This detection limit is well below the concentrations used in these experiments and therefore allowed accurate measurement of the material mass disseminated.

Results and Discussion

The particle size of each material is shown in Figure 8-1. The mean particle diameter of both the 12nm and 35nm thick material was 10 ± 2 microns. The 60nm thick material was slightly smaller with a mean particle size of 6 ± 3 microns. Scanning electron microscope images of the aluminum flakes with varying concentrations of silica can be seen in Figure 8-2 A-C. Figure 8-2A shows an image of the 35nm thick flakes without silica added. Figure 8-2B and 8-2C show images of the same material with 5 and 10 weight percent silica added respectively.

The results for packing can be seen in Figure 8-3. The flake packing can be increased but at the expense of the FoM. Optimum packing is shown to be between 15 and 20 percent by volume and achieved by vibrational packing of the supercritical dried powder. Packing by slurry evaporation uses the capillary forces present to pull the powder together and in turn increases the amount of agglomeration. Centrifuging can lead to mechanical interlocking by physical deformation of the flakes.

Supercritical Fluid processing in liquid CO₂ resulted in a very loosely packed powder of soft agglomerates with a low bulk density which was shown to effectively produce a dispersible dry powder. During SCF processing the formation of the gas-liquid interface is completely avoided as are the capillary forces limiting the strong van der Waals forces present found after conventional drying. These dry, dispersible powders were then disseminated in the Galai® vacuum dispersion chamber onto a glass microscope slide and a DPT for evaluation.

The effect of thickness can be seen in Figure 8-4. For thinner flakes, the FoM continuously increased. In these experiments, decreasing the aluminum thickness from the 60nm flakes to 35nm flakes resulted in an increase in the average FoM from 3.75 to 6. A further reduction in thickness using the 15nm flakes resulted in an increase in the average FoM to 10. The increase in FoM for these samples is lower than theory due to the presence of agglomerates. The addition of the fumed silica as a spacer material is shown to have a maximum effect as seen in Figure 8-5. When silica was added there was an increase in the FoM. It should be noted that the addition of five weight percent silica to the 35nm aluminum flake results in an increase in FoM from 6 to 7.9, close to the theoretical value suggesting that the powder is better dispersed. However, at the highest concentration of silica, ten weight percent, there was a decrease in the FoM below that of the aluminum without silica.

Unlike aluminum, silica is transparent through most of the IR and does not attenuate any IR light. As silica is added to the mixture, it has been shown to reside between the aluminum flakes and increases the interparticle spacing, seen in Figure 8-2. In turn, the strong but short ranged van der Waals forces are reduced and the powder disperses to a higher degree as seen by the increased FoM. The silica is added on a weight basis thus as silica is added, the amount of aluminum in the mixture decreases. When the silica concentration is in excess of that needed to

aid in dispersion, the reduced amount of aluminum results in less material to attenuate the IR and as it follows, a decrease in the FoM. A similar trend can be seen at all flake thicknesses; however, the effect is not as profound for the 60nm flakes, which disperse equally at all silica concentrations. A summary of the results can be seen in Figure 8-6.

These results were also analyzed using the Design Expert 6 statistical design software. Three repeats of each point were run to take into consideration the sample-to-sample variability. The surface response plot is below in Figure 8-7. The standard deviation of the data is 0.5, which means that the values on the graph are significantly different. From this output it can be seen that the FoM increases with decreasing thickness, similarly to the data from the FTIR results above, and that there is a maximum in the spacer concentration at four weight percent.

Conclusions

The drying process is crucial to the production of a dispersible, dry powder. By using Supercritical Fluid processing in liquid CO₂ the production of a dispersible dry powder has been demonstrated. This is due to the ability of this processing technique to remove liquid without the formation of the gas/liquid interface and thus capillary forces that lead to agglomeration. The FoM of the aluminum powder was shown to increase as the thickness of the flakes decreased as long as SCF processing was leveraged to produce the dry material. As flake thickness decreased, a higher number of flakes per unit mass were available to interact with the laser, lowering the transmission. Fumed silica was shown to increase the dispersion of the aluminum flakes by increasing the interparticle spacing and thus reducing the van der Waals forces between the flakes. The silica was shown to have a maximum in effectiveness at four weight percent. Although the silica increased the interparticle spacing to improve dispersion, it was added on a weight basis, so the further addition reduced the FoM. Since silica is transparent in the IR, thus after four weight percent silica was added, the number of aluminum particles available to

attenuate with the laser was decreased causing the decrease in FoM. Statistical design of experiments as used to insure that the results were obtained efficiently and were significant.

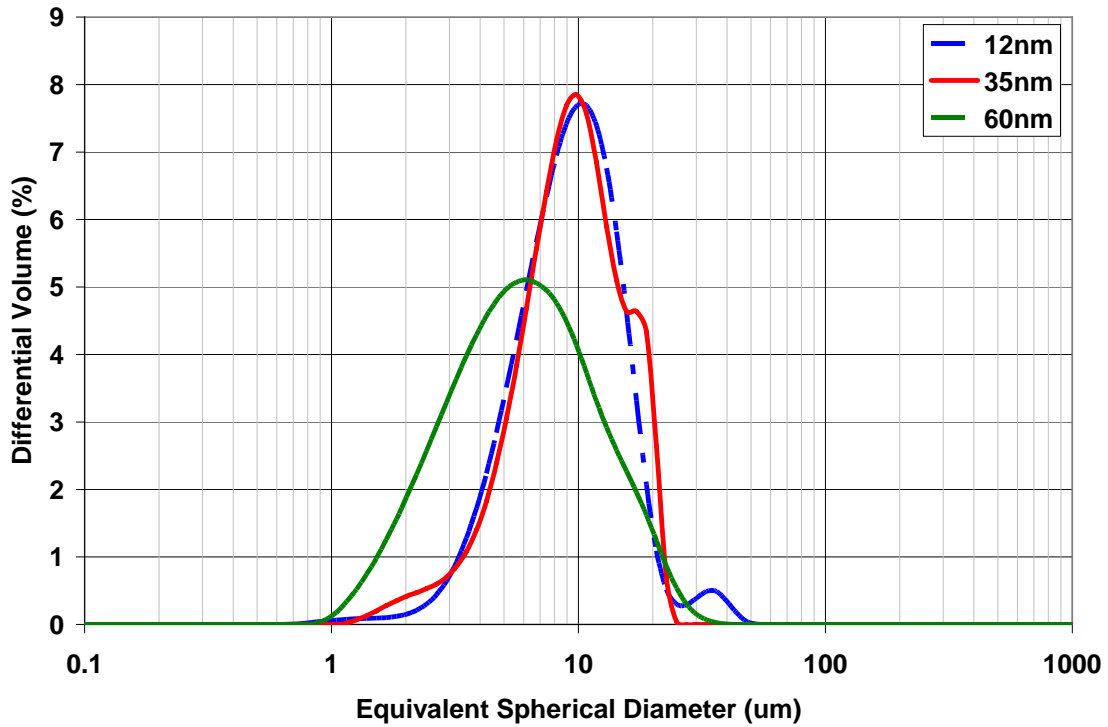


Figure 7-1. Laser Diffraction particle size distribution for aluminum flakes. A graph of the particle size distribution of the aluminum flakes as measured by laser light scattering in the Bachman/Counter 13320. The blue curve depicts the particle size for the 12nm thick flakes, the red curve shows that of the 35nm thick flakes, and the green curve shows the particle size of the 60 nm thick flakes.



Figure 7-2. Typical Images of aluminum flakes and silica. A) shows the edge of one flake, B) shows the aluminum/silica mixture at low silica concentrations, and C) shows the aluminum/silica mixture at high silica concentrations. Note the distribution of silica between the flakes increasing the interparticle spacing.

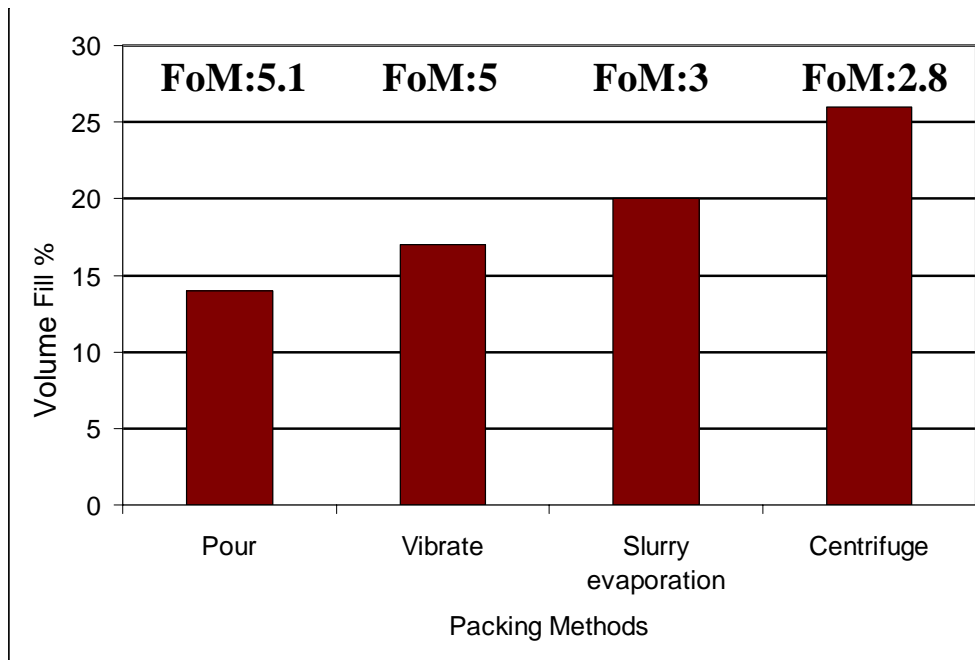


Figure 7-3. Packing density of flakes and FoM. By using different consolidation methods the maximum packing density is increased but at the sacrifice of FoM. Slurry evaporation leads to agglomeration due to capillary forces and centrifuging can lead to mechanical deformation and physical interlocking of the flakes. The optimum is shown to be between 15-20 volume percent.

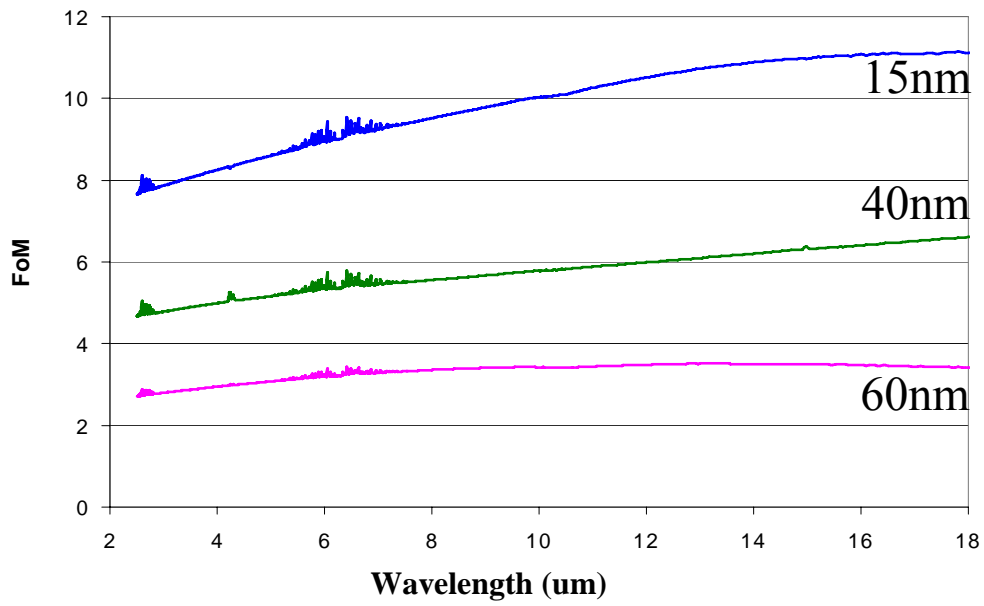


Figure 7-4. Figure of Merit for aluminum flakes of varying thickness. As thickness is decreased, the number of flakes present per unit mass increases resulting in an increase in the FoM.

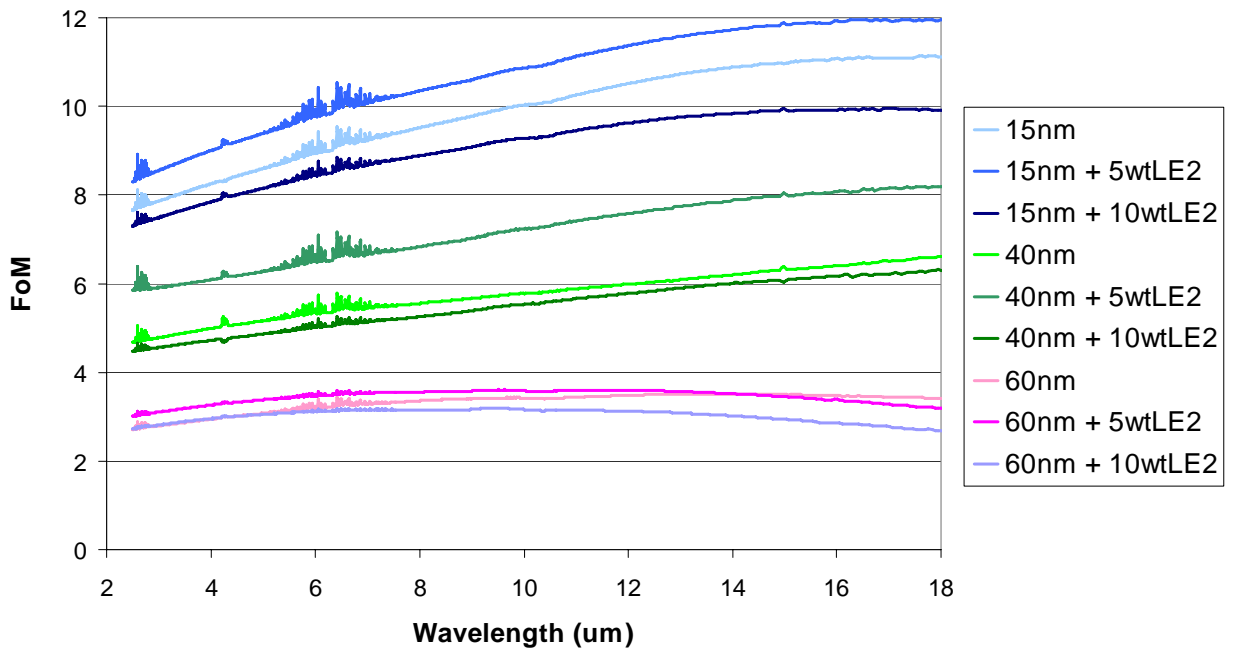


Figure 7-5. Figure of Merit for aluminum flakes of varying thickness and spacer concentration.

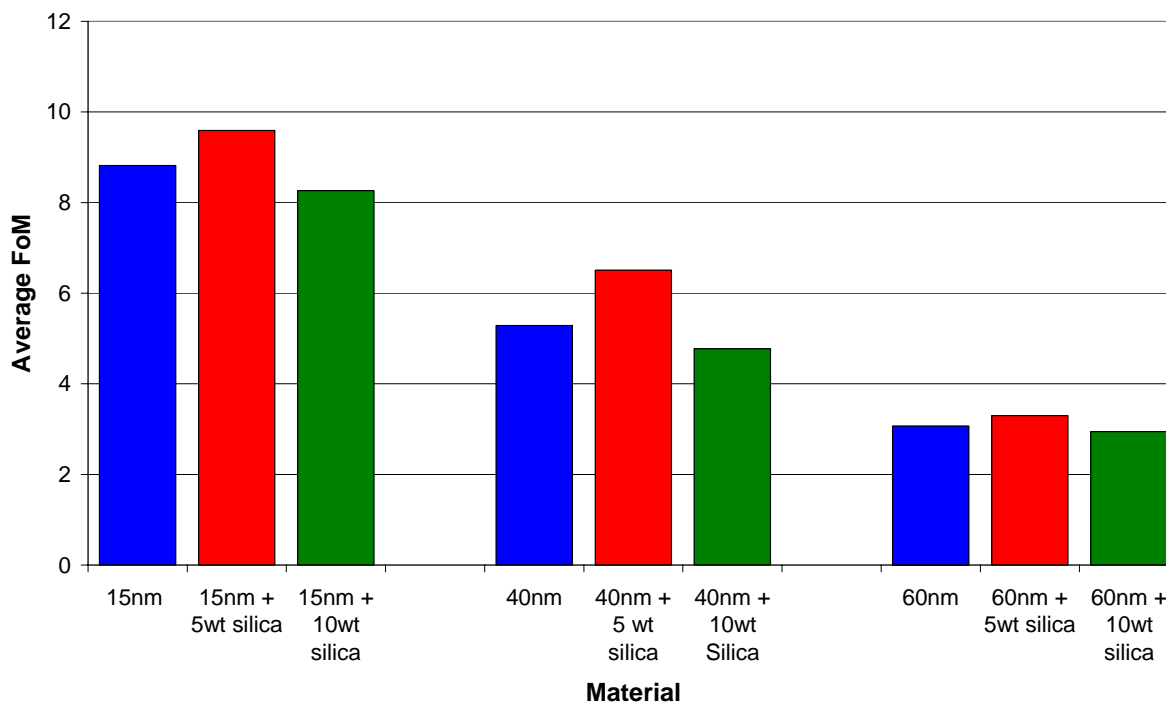


Figure 7-6. Average FoM across all wavelengths for aluminum flakes of varying thickness and silica concentrations. The addition of 5wt% silica increases the interparticle spacing, aiding in dispersion as seen in the FoM. With the further addition of silica above the optimum, excess silica decreases the amount of aluminum resulting in a decrease in FoM. Similar trends were seen for all materials.

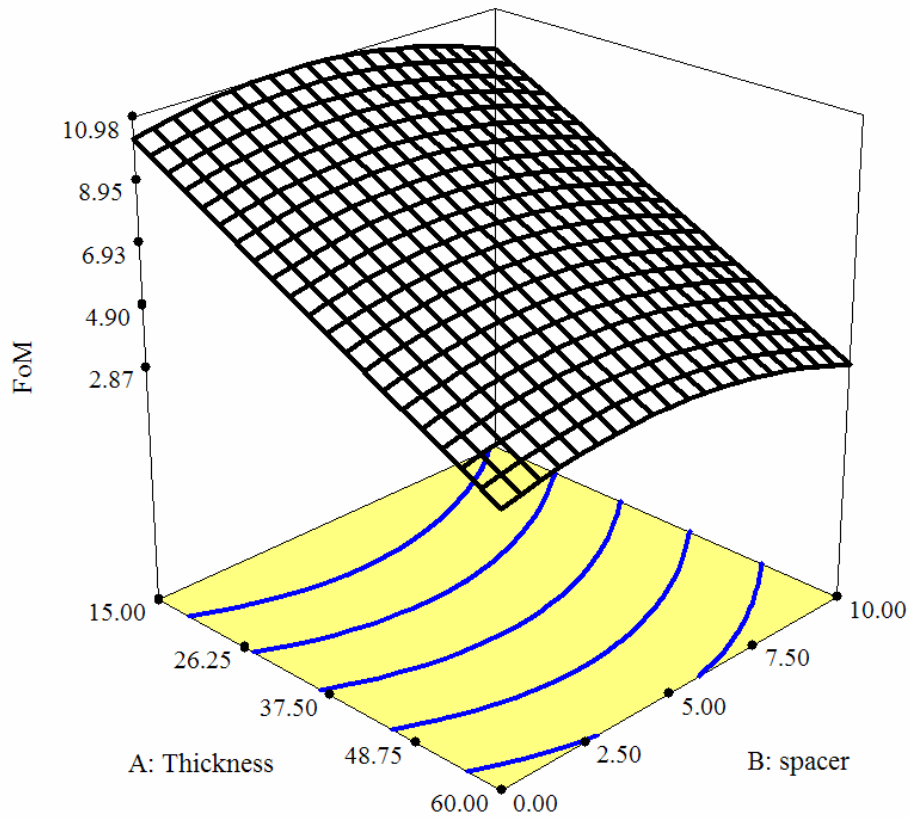


Figure 7-7. Design Expert Surface Response plot for FoM. From the plot the effect of decreasing flake thickness and increasing spacer concentration can be seen. Decreasing flake thickness increases FoM due to the higher number of flakes available to attenuate the light. The spacer decreases the contact area between flakes thereby improving dispersion. A maximum at four weight percent spacer can be seen as additional spacer decreases the amount of aluminum present. The best results are found with a 12nm thick flake and 5 weight percent spacer yielding a FoM value of 11.

CHAPTER 8 SUGGESTIONS FOR FUTURE WORK

Through the research presented in this dissertation, an understanding of the factors that affect dispersion and the changes in interparticle forces associated with those factors was developed. Because of this fundamental understanding, the conclusions developed through this work can be applied towards other powder systems. Despite these achievements, ideal dispersion still was not achieved. To this end, further research is now suggested.

The first step to understanding dispersion is its measurement. In this research a settling chamber was built to measure transmission decay of the settling aerosol. From these measurements and the Beer-Lambert Law, the airborne concentration of powder was calculated and used to compare the effectiveness of the processing and dissemination methods.

Transmission measurements over time also result in a line whose slope is proportional to settling rate. Specifically, it is equal to the change in concentration divided by the height of the chamber. From the settling rate and the equation for Stokes' settling, a particle size for the powder can be calculated. This would be a valuable undertaking that would complement airborne concentration measurements. With this disseminated particle size, a comparison can be made to the actual primary particle size and result in the development of a dispersion index. This would also give a more accurate description of the state of dispersion. For this, improvements to the dispersion chamber are required.

The current measurements made in the dispersion chamber result in a large variation in transmission at the initial times due to the high turbulence associated dissemination. One factor that can affect this variation is chamber volume, specifically height. Increasing the height of the chamber could allow the initial turbulence in the system to stabilize before reaching the height of the laser. Less turbulence at the level of the measuring laser beam would lead to more consistent

measurements and more accurate calculation of the particle size both of which are required to use this measurement method to develop a dispersion index.

In this research, methods were developed to measure interparticle forces at the macro and micro scale. These measurements were then used to develop a better understanding of the effect of the processing parameters on the change in interparticle forces and a subsequent correlation to dispersion. However, the direct correlation between interparticle forces and dispersion was not made. In continuation of the above discussion of the effective particle size, or dispersion index, this could be related directly to interparticle forces. From this a predictive model could be developed to relate interparticle forces directly to particle size, and thus the degree of dispersion. A model based on the empirical results, as that produced by statistical experimental design, would also serve in such a way if the disseminated particle size was used as a response. This would expand the model to also include the analysis of error within the experiments. The source of error, and those areas where it should be reduced, can also be used to determine optimum processing factors and levels thereof.

Another aspect of this research that had proven to be challenging is the application of a dispersion force to the agglomerates. As shown in this research, the effect of increasing pressure, and turbulence, is limited to the minimum turbulent eddy size. The addition of a radial dispersion force acting from within the agglomerate, through a volatile medium, was shown to improve dispersion. This concept could also be accompanied by the use of nozzles. Through nozzle design, rapid changes in velocity, volume, and pressure can be created. Using liquid CO₂ to create a large increase in volume combined with a standard dispersion nozzle geometry, such as a converging diverging nozzle, large gradients can be created. This could result in a reduction of the minimum turbulent eddy size and the application of a large dispersion force to smaller

agglomerates. This idea can be taken to the extreme case. With the correct configuration, a sufficient change in conditions can result in supersonic velocities and associated with that supersonic transition is a shockwave which may add enough force to greatly improve dispersion.

LIST OF REFERENCES

1. Byron, P.R., *Prediction of Drug Residence Time in Regions of the Human Respiratory Track Following Aerosol Inhalation*. Journal of Pharmaceutical Sciences, 1986. **75**(5): p. 433-438.
2. Reed, J.S., *Principles of Ceramic Processing*. 2nd ed. 1995, New York: John Wiley and Sons.
3. Haynes, R.J. and R. Naidu, *Influence of Lime, Fertilizer, and Manure Applications on Soil Organic Matter Content and Soil Physical Conditions: A Review*. Nutrient Cycling in Agroecosystems, 1998. **51**(2): p. 123-137.
4. Embury, J., *Optimum smoke Nanoparticles that Maximize Attenuation at Infrared and Radar Wavelengths*, US Army Edgewood Chemical and Biological Center.
5. de Boer, A.H., et al., *Air Classifier Technology (ACT) in Dry Powder Inhalation Part 2. The Effect of Lactose Carrier Surface Properties on the Drug-to-Carrier Interaction in Adhesive Mixtures for Inhalation*. International Journal of Pharmaceutics, 2003. **260**(2): p. 201.
6. French, D.L., D.A. Edwards, and R.W. Niven, *The Influence of Formulation on Emission, Deaggregation and Deposition of Dry Powders for Inhalation*. Journal of Aerosol Science, 1996. **27**(5): p. 769-783.
7. Louey, M.D., P. Mulvaney, and P.J. Stewart, *Characterization of Adhesional Properties of Lactose Carriers Using Atomic Force Microscopy*. Journal of Pharmaceutical and Biomedical Analysis, 2001. **25**(3-4): p. 559-567.
8. Louey, M.D. and P.J. Stewart, *Particle Interactions Involved in Aerosol Dispersion of Ternary Interactive Mixtures*. Pharmaceutical Research, 2002. **19**(10): p. 1524-1531.
9. Mullins, M.E., et al., *Effect of Geometry on Particle Adhesion*. Aerosol Science and Technology, 1992. **17**(2): p. 105-118.
10. Musante, C.J., et al., *Factors Affecting the Deposition of Inhaled Porous Drug Particles*. Journal of Pharmaceutical Sciences, 2002. **91**(7): p. 1590-1600.

11. Ranade, M.B., *Research on Coatings or Surface Treatment of Metal Powders*, A.F.C.R. Laboratory, Editor. 1975.
12. Ranade, M.B., *Surface Treatment on Metal Powders for Dispersion Improvement*, C.R.a.D. Center, Editor. 1984.
13. Zeng, X.M., et al., *The Role of Fine Particle Lactose on the Dispersion and Deaggregation of Salbutamol Sulphate in an Air Stream in Vitro*. International Journal of Pharmaceutics, 1998. **176**(1): p. 99-110.
14. Zijlstra, G.S., et al., *The Role of Particle Engineering in Relation to Formulation and De-Agglomeration Principle in the Development of a Dry Powder Formulation for Inhalation of Cetrorelix*. European Journal of Pharmaceutical Sciences, 2004. **23**(2): p. 139.
15. Masuda, H., Higashitani, K., Yoshida, H., ed. *Powder Technology Handbook*. Third ed. 2006, Taylor and Francis Group, LLC: Boca Ratone, FL.
16. Chan, H.-K. and N.Y.K. Chew, *Novel Alternative Methods for the Delivery of Drugs for the Treatment of Asthma*. Advanced Drug Delivery Reviews, 2003. **55**(7): p. 793.
17. Galk, J., W. Peukert, and J. Krahn, *Industrial Classification in a New Impeller Wheel Classifier*. Powder Technology, 1999. **105**(1-3): p. 186.
18. Hickey, A., *A New Millenium for Inhaler Technology*. Pharmaceutical Technology, 1997. **21**(6): p. 116-125.
19. Holdich, R., *Fundamentals of Particle Technology*. 2002, Shepshed, U.K.: Midland Information and Technology Publishing.
20. Masuda, H. and K. Gotoh, *Dry Dispersion of Fine Particles*. Colloids and Surfaces A: Physicochemical and Engineering Aspects, 1996. **109**: p. 29.
21. Sweeney, L.G., et al., *Spray-Freeze-Dried Liposomal Ciprofloxacin Powder for Inhaled aerosol drug delivery*. International Journal of Pharmaceutics, 2005. **305**(1-2): p. 180.
22. Voss, A. and W. Finley, *Deagglomeration of Dry Powder Pharmaceutical Aerosols*. International Journal of Pharmaceutics, 2002. **248**.

23. Calabrese, R.V. and M.B. Ranade, *Pneumatic Nozzle Dissemination of Powders into Air*, U.S.A.R. Office, Editor. 1993.
24. Chew, N.Y.K., D.F. Bagster, and H.K. Chan, *Effect of Particle Size, Air Flow and Inhaler Device on the Aerosolization of Disodium Cromoglycate Powders*. International Journal of Pharmaceutics, 2000. **206**(1-2): p. 75-83.
25. Chew, N.Y.K. and H.K. Chan, *Influence of Particle Size, Air Flow, and Inhaler Device on the Dispersion of Mannitol Powders as Aerosols*. Pharmaceutical Research, 1999. **16**(7): p. 1098-1103.
26. Chew, N.Y.K., et al., *Characterization of Pharmaceutical Powder Inhalers: Estimation of Energy Input for Powder Dispersion and Effect of Capsule Device Configuration*. Journal of Aerosol Science, 2002. **33**(7): p. 999-1008.
27. Endo, Y., S. Hasebe, and Y. Kousaka, *Dispersion of Aggregates of Fine Powder by Acceleration in an Air Stream and its Application to the Evaluation of Adhesion Between Particles*. Powder Technology, 1997. **91**(1): p. 25-30.
28. Chew, N.Y.K. and H.K. Chan, *Effect of Powder Polydispersity on Aerosol Generation*. Journal of Pharmacy and Pharmaceutical Sciences, 2002. **5**(2): p. 162-168.
29. Raula, J., et al., *Study of the Dispersion Behaviour of l-leucine Containing Microparticles Synthesized with an Aerosol Flow Reactor Method*. Powder Technology, 2007. **177**(3): p. 125.
30. Zeng, R.J. and B. Rand, *Particle Size Distribution, Powder Agglomerates and their Effects on Sinterability of Ultrafine Alumina Powders*. Journal of Materials Science & Technology, 2000. **16**(4): p. 393-396.
31. Zeng, X.M., et al., *Effects of Particle Size and Adding Sequence of Fine Lactose on the Deposition of Salbutamol Sulphate from a Dry Powder Formulation*. International Journal of Pharmaceutics, 1999. **182**(2): p. 133-144.
32. Mizes, H., et al., *Small Particle Adhesion: Measurement and Control*. Colloids and Surfaces a-Physicochemical and Engineering Aspects, 2000. **165**(1-3): p. 11-23.

33. Crowder, T.M., et al., *Fundamental Effects of Particle Morphology on Lung Delivery: Predictions of Stokes' Law and the Particular Relevance to Dry Powder Inhaler Formulation and Development*. *Pharmaceutical Research*, 2002. **19**(3): p. 239-245.
34. Ho, C.A. and M. Sommerfeld, *Modelling of Micro-Particle Agglomeration in Turbulent Flows*. *Chemical Engineering Science*, 2002. **57**(15): p. 3073-3084.
35. Lightstone, M.F. and G.D. Raithby, *A Stochastic Model of Particle Dispersion in a Turbulent Gaseous Environment*. *Combustion and Flame*, 1998. **113**(3): p. 424-441.
36. He, Y.H., *A Criterion for Particle Agglomeration by Collision*. *Powder Technology*, 1999. **103**(2): p. 189-193.
37. Han, R., G. Papadopoulos, and B.J. Greenspan, *Investigation of Powder Dispersion Inside a SPIROS(R) Dry Powder Inhaler using Particle Image Velocimetry*. *Powder Technology*, 2002. **125**(2-3): p. 266.
38. Wang, Z.L., C.F. Lange, and W.H. Finlay, *Use of an Impinging Jet for Dispersion of Dry Powder Inhalation Aerosols*. *International Journal of Pharmaceutics*, 2004. **275**(1-2): p. 123-131.
39. Gomes, M. and e. al, *The Effect of Inertial on the Dispersion of Particles in the Flow Around a Two-Dimensional Flate Plate*. *Chemical Engineering Science*, 2002. **57**: p. 1319-1329.
40. Mullins, M.E. and M.B. Ranade, *Force of Adhesion and the Energy Required to Disperse Test Dust in Air*, U.S.A. Chemical Research and Development Center, Editor. 1984.
41. Vold, M.J., *The Effect of Adsorption on the van der Waals Interaction of Spherical Colloidal Particles*. *Journal of Colloid Science*, 1961. **16**(1).
42. Safatov, A.S., et al., *Variations in Disperse Composition of Dry Powders According to Energy of their Dispersion*. *Powder Technology*, 1998. **97**(3): p. 227-232.
43. Feng, J.Q. and D.A. Hays, *Relative Importance of Electrostatic Forces on Powder Particles*. *Powder Technology*, 2003. **135**: p. 65-75.
44. Reist, P.C., *Intoduction to Aerosol Science*. 1984: p. 299.

45. Reist, P.C., *Aerosol Science and Technology*. Second ed. 1993, New York: McGraw-Hill, Inc. 379.
46. Yurteri, C.U., et al., *Electrostatic Effects on Dispersion, Transport, and Deposition of Fine Pharmaceutical Powders: Development of an Experimental Method for Quantitative Analysis*. *Particulate Science and Technology*, 2002. **20**(1): p. 59-79.
47. Ren, J., et al., *Electrostatic Dispersion of Fine Particles in the Air*. *Powder Technology*, 2001. **120**(3): p. 187.
48. Ren, J., S.C. Lu, and F.Q. Tang, *The Voltage-Current Characteristics and Dispersion Effect of RLW Electrostatic Disperser*. *Powder Technology*, 2003. **135**: p. 261-265.
49. Ata, A., Y.I. Rabinovich, and R.K. Singh, *Role of Surface Roughness in Capillary Adhesion*. *Journal of Adhesion Science and Technology*, 2002. **16**(4): p. 337-346.
50. Hooton, J.C., et al., *An Atomic Force Microscopy Study of the Effect of Nanoscale Contact Geometry and Surface Chemistry on the Adhesion of Pharmaceutical Particles*. *Pharmaceutical Research*, 2004. **21**(6): p. 953-961.
51. Hooton, J.C., et al., *Characterization of Particle-Interactions by Atomic Force Microscopy: Effect of contact Area*. *Pharmaceutical Research*, 2003. **20**(3): p. 508-514.
52. Nguyen, A.V., et al., *Attraction between Hydrophobic Surfaces Studied by Atomic Force Microscopy*. *International Journal of Mineral Processing*, 2003. **72**(1-4): p. 215-225.
53. Rabinovich, Y.I., et al., *Adhesion between Nanoscale Rough Surfaces - I. Role of Asperity Geometry*. *Journal of Colloid and Interface Science*, 2000. **232**(1): p. 10-16.
54. Rabinovich, Y.I., et al., *Adhesion between Nanoscale Rough Surfaces - II. Measurement and Comparison with Theory*. *Journal of Colloid and Interface Science*, 2000. **232**(1): p. 17-24.
55. Rabinovich, Y.I., et al., *Capillary Forces between Surfaces with Nanoscale Roughness*. *Advances in Colloid and Interface Science*, 2002. **96**(1-3): p. 213-230.
56. Ren, J., et al., *Research on the Composite Dispersion of Ultra Fine Powder in the Air*. *Materials Chemistry and Physics*, 2001. **69**(1-3): p. 204.

57. Tammet, H., *Productivity of an Electric Mobility Classifier*. Journal of Aerosol Science, 1996. **27**(Supplement 1): p. S219.
58. Gupta, R., D. Gidaspow, and D.T. Wasan, *Electrostatic Separation of Powder Mixtures Based on the Work-Functions of Its Constituents*. Powder Technology, 1993. **75**(1): p. 79-87.
59. DeSimone, J.M. and J.S. Keiper, *Surfactants and self-assembly in carbon dioxide*. Current Opinion in Solid State & Materials Science, 2001. **5**(4): p. 333-341.
60. Maury, E.E., et al., *Graft Copolymer Surfactants for Supercritical Carbon-Dioxide Applications*. Abstracts of Papers of the American Chemical Society, 1993. **206**: p. 383-POLY.
61. DeSimone, J.M., et al., *Self assembly of small molecules and macromolecules in compressible liquid and supercritical Co-2*. Abstracts of Papers of the American Chemical Society, 2002. **224**: p. U313-U314.
62. Desimone, J.M., et al., *Dispersion Polymerizations in Supercritical Carbon-Dioxide*. Science, 1994. **265**(5170): p. 356-359.
63. Shekunov, B.Y., et al., *Aerosolization behaviour of micronised and supercritically-processed powders*. Journal of Aerosol Science, 2003. **34**(5): p. 553-568.
64. Sellers, S.P., et al., *Dry powders of stable protein formulations from aqueous solutions prepared using supercritical CO₂-assisted aerosolization*. Journal of Pharmaceutical Sciences, 2001. **90**(6): p. 785-797.
65. Sievers, R.E., et al., *Supercritical fluid carbon dioxide technologies for fine particle formation for pulmonary drug delivery*. Abstracts of Papers of the American Chemical Society, 2000. **219**: p. U33-U34.
66. Kousada, Y. and e. al, *Generation of an Aerosol by the Boiling of Suspensions*. Aerosol Science and Technology, 1994. **8**(21): p. 236.
67. Zimon, A.D., *Adhesion of Dust and Powder*. 1969, New York: Plenum Press.

68. Callister, W.D., *Materials Science and Engineering, An Introduction*. 1997, New York: Wiley and Sons, Inc.
69. London, F., Eisenschitz, E., *The relation between the van der Waals forces and the homeopolar valence forces*. Zeits. f. Physik, 1930. **60**(491).
70. Hamaker, H.C., *The London van der Waals attraction between spherical particles*. Physica IV, 1937. **10**(1048).
71. van der Waals, J.D., *The Equation of State for Gases and Liquids*, in *Nobel Lecture*. 1910.
72. van der Waals, J.D., *Over de Continuïteit van de Gas- En Vloeistofoestand (On the Continuity of the Gaseous and Liquid States)*. 1873, Leiden University, Netherlands.
73. Lennard-Jones, J.E.D., B.M., *Cohesion at a Crystal Surface*. Transactions of the Faraday Society, 1928. **24**(92).
74. London, F., *The General Theory of Molecular Forces*. Transactions of the Faraday Society, 1937. **33**(8).
75. Derjaguin, B.V., *Kolloid Zeitschrift*, 1934. **69**(155).
76. Hamaker, H.C., *Physica*, 1937. **4**(1058).
77. Bradley, R.S., *The Cohesive Force Between Solid Surfaces and the Surface Energy of Solids*. Philosophical Magazine, 1932. **13**(86): p. 853-862.
78. de Boer, J.H., *Transactions of the Faraday Society*, 1936. **32**: p. 10-18.
79. Lifshitz, E.M., *The Theory of Molecular Attractive Forces Between Solids*. Soviet Physics JETP, 1956. **2**(73).
80. Ninham, B.W. and V.A. Parsegian, *van der Waals Forces - Special Characteristics in Lipid-Water Systems and a General Method of Calculation Based on Lifshitz Theory*. Biophysical Journal, 1970. **10**(646).

81. Hough, D.B. and L.R. White, *The Calculation of Hamaker Constants from Lifshitz Theory with Applications to Wetting Phenomena*. Advances in Colloid and Interface Science, 1980. **14**(1): p. 3-41.
82. Tabor, D. and H. Winterton, *Direct Measurement of Normal and Retarded van der Waals Forces*. Proceedings for the Royal Society of London Series a-Mathematical and Physical Sciences, 1969. **312**(1511).
83. Israelachvili, J., *Intermolecular & Surface Forces*. 2nd Edition ed. 1992, San Diego: Academic Press Inc.
84. Fisher, R.A., *On the Capillary Forces in an Ideal Soil; Correction of Formulae given by W. B. Haines*. Journal of Agriculture Science, 1926. **16**: p. 492.
85. Coelho, M.C., *Upper Humidity Limit of the Pendular State*. Powder Technology, 1979. **23**(2): p. 203-207.
86. Coelho, M.C. and N. Harnby, *Effect of Humidity on Form of Water-Retention in a Powder*. Powder Technology, 1978. **20**(2): p. 197-200.
87. Coelho, M.C. and N. Harnby, *Moisture Bonding in Powders*. Powder Technology, 1978. **20**(2): p. 201-205.
88. Rumpf, H., *Die Wissenschaft des Agglomerierens*. Chem.-Ing.-Tech, 1974. **46**: p. 1-11.
89. Rumpf, H., K. Sommer, and K. Steier, *Mechanismen der Haftkraftverstärkung bei der Partikelhaftung durch plastisches Verformen, Sintern und viskoelastisches Fließen*. Chem. Eng. Tech, 1976. **48**: p. 300-307.
90. Adler, J., *Interaction of Non-Ideal Surfaces in Particulate Systems*. 2001, PhD Dissertation, University of Florida: Gainesville.
91. Rabinovich, Y.I., M.S. Esayanur, and B.M. Moudgil, *Capillary Forces between Two Spheres with a Fixed Volume Liquid Bridge: Theory and Experiment*. Langmuir, 2005. **21**(24): p. 10992-10997.

92. Esayanur, M.S., *Interparticle Force Based Methodology for Prediction of Cohesive Powder Flow Properties*, in *Materials Science and Engineering*. 2004, PhD Dissertation, University of Florida: Gainesville.
93. Alonso, M. and F.J. Alguacil, *Penetration of aerosol undergoing combined electrostatic dispersion and diffusion in a cylindrical tube*. *Journal of Aerosol Science*, 2007. **38**(5): p. 481.
94. Stotzel, H., et al., *Adhesion measurements for electrostatic powder coatings*. *Journal of Electrostatics*, 1997. **40-1**: p. 253-258.
95. Rimai, D.S., D.J. Quesnel, and A.A. Busnaina, *The adhesion of dry particles in the nanometer to micrometer-size range*. *Colloids and Surfaces a-Physicochemical and Engineering Aspects*, 2000. **165**(1-3): p. 3-10.
96. Kunkel, W.B., *Comment on Static Electrification of Dust Particles on Dispersion into a Cloud*. *Journal of Applied Physics*, 1951. **22**(1): p. 103-104.
97. Kunkel, W.B., *The Static Electrification of Dust Particles on Dispersion into a Cloud*. *Journal of Applied Physics*, 1950. **21**(8): p. 820-832.
98. Nakajima, Y. and T. Sato, *Electrostatic collection of submicron particles with the aid of electrostatic agglomeration promoted by particle vibration*. *Powder Technology*, 2003. **135**: p. 266-284.
99. Watanabe, T., et al., *Submicron Particle Agglomeration by an Electrostatic Agglomerator*. *Journal of Electrostatics*, 1995. **34**(4): p. 367-383.
100. Laitinen, A., et al., *Bipolar charged aerosol agglomeration with alternating electric field in laminar gas flow*. *Journal of Electrostatics*, 1996. **38**(4): p. 303-315.
101. Law, S.E., S.A. Thompson, and W. Balachandran, *Electroclamping forces for controlling bulk particulate flow: Charge relaxation effects*. *Journal of Electrostatics*, 1996. **37**(1-2): p. 79-93.
102. Crowder, T. and A. Hickey, *Powder specific active dispersion for generation of pharmaceutical aerosols*. *International Journal of Pharmaceutics*, 2006. **327**(1-2): p. 65-72.

103. Boisdron, Y. and J.R. Brock, *On Stochastic Nature of Acquisition of Electrical Charge and Radioactivity by Aerosol Particles*. Atmospheric Environment, 1970. **4**(1): p. 35-&.
104. Natanson, G.L., *On the Theory of the Charging of Amicroscopic Aerosol Particles as a Result of Capture of Gas Ions*. Soviet Physics-Technical Physics, 1960. **5**(5): p. 538-551.
105. Pauthenier and M. Moreau-Hanot, *Spherical particle charges in an ionized field*. Journal De Physique Et Le Radium, 1932. **3**: p. 590-613.
106. Pauthenier, M. and R. Guillien, *Direct electrometric study of the limited charge of a conductor sphere in an ionised electric field*. Comptes Rendus Hebdomadaires Des Seances De L Academie Des Sciences, 1932. **195**: p. 115-116.
107. Pauthenier, M., M. Moreau-Hanot, and R. Guillien, *Charge of small dielectric spheres in an ionised electric field*. Comptes Rendus Hebdomadaires Des Seances De L Academie Des Sciences, 1932. **195**: p. 213-215.
108. Yoon, R.-H., D.H. Flinn, and Y.I. Rabinovich, *Hydrophobic Interactions between Dissimilar Surfaces*. Journal of Colloid and Interface Science, 1997. **185**(2): p. 363.
109. Keiper, J.S., et al., *New phosphate fluorosurfactants for carbon dioxide*. Journal of the American Chemical Society, 2002. **124**(9): p. 1834-1835.
110. Ye, W.J., J.S. Keiper, and J.M. DeSimone, *Polymeric nanoparticles from supercritical CO₂ microemulsion polymerization*. Chinese Journal of Polymer Science, 2006. **24**(1): p. 95-101.
111. Ducker, W.A., T.J. Senden, and R.M. Pashley, *Measurement of Forces in Liquids Using a Force Microscope*. Langmuir, 1992. **8**: p. 1831.
112. Rabinovich, Y.I. and R.H. Yoon, *Use of Atomic Force Microscope for the Measurements of Hydrophobic Forces between Silanated Silica Plate and Glass Sphere*. Langmuir, 1994. **10**(6): p. 1903-1909.
113. Cadle, R.D., *The Measurement of Airborne Particles*. 1975, New York: John Wiley and Sons, Inc.

114. Fuks, N.A., *The mechanics of aerosols*. Rev. and enl. ed. 1964, Oxford, New York: Pergamon Press; [distributed in the Western Hemisphere by Macmillan. xiv, 408 p.
115. Embury, J., *Particles Producing Strong Extinction in the Infrared*. Technical Report, 1994. US. Chemical Systems Laboratory.
116. Embury, J., *Maximizing Infrared Extinction Coefficients for Metal Discs, Rods, and Spheres*. Technical Report, 2002. US Army Edgewood Chemical and Biological Center.
117. Appleyard, P.G., *Infrared extinction performance of high aspect ratio carbon nanoparticles*. Journal of Optics a-Pure and Applied Optics, 2006. **8**(2): p. 101-113.
118. Appleyard, P.G., *Modelled infrared extinction and attenuation performance of atmospherically disseminated high aspect ratio metal nanoparticles*. Journal of Optics a-Pure and Applied Optics, 2007. **9**(3): p. 278-300.
119. Appleyard, P.G. and N. Davies, *Modelling infrared extinction of high aspect ratio, highly conducting small particles*. Journal of Optics a-Pure and Applied Optics, 2004. **6**(10): p. 977-990.
120. Appleyard, P.G. and N. Davies, *Calculation and measurement of infrared mass extinction coefficients of selected ionic and partially ionic insulators and semiconductors: a guide for infrared obscuration applications*. Optical Engineering, 2004. **43**(2): p. 376-386.
121. Embury, J., *Particles Producing Strong Extinction in the Infrared*. Technical Report, 1995. US Army Edgewood Chemical and Biological Center.
122. Embury, J., *Optimum Smoke Nanoparticles that Maximize Attenuation at Infrared and Radar Wavelengths*. Technical Report, 1998. US Army Edgewood Chemical and Biological Center.
123. Embury, J., *Extinction of Laser Radiation by Man-Made Graphite Flake Aerosols*. Technical Report, 1993. US Army Edgewood Chemical and Biological Center.
124. Embury, J., *Screening Smokes Performance of Commercially Available Powders III: Infrared and Visible Screening by Carbon Black*. Technical Report, 1994. US Army Edgewood Chemical and Biological Center.

BIOGRAPHICAL SKETCH

Stephen Tedeschi was born in Schenectady, New York. He graduated from Notre Dame – Bishop Gibbons High School in May 1997 and enrolled in The New York State School of Ceramics at Alfred University in Alfred, New York that fall. Stephen earned a Bachelors of Science in Ceramic Engineering upon graduation in May 2002. Stephen wanted to continue this education and in August of 2002 Stephen began his studies at the University of Florida. He received a Masters of Science in Materials Science and Engineering in December 2004 and a Doctorate of Philosophy in December 2007. After completion of his PhD, Stephen hopes to take the knowledge he gained here at the University of Florida and continue to do research in the area of Particle Science and Technology as part of an industrial research and development facility.